Wealth Thermalization Hypothesis and Social Networks

Klaus M. Frahm[1,2*†] and Dima L. Shepelyansky[1,2†]

[1*]Lab. Physique Théorique, Université Toulouse III - Paul Sabatier, UPS, CNRS, Toulouse, France.
[2]Univ Toulouse, CNRS, LPT, Toulouse, France.

*Corresponding author(s). E-mail(s): klaus.frahm@utoulouse.fr;
†These authors contributed equally to this work.
received: September 21, 2025

Abstract

In 1955 Fermi, Pasta, Ulam and Tsingou performed first numerical studies with the aim to obtain the thermalization in a chain of nonlinear oscillators from dynamical equations of motion. This model happend to have several specific features and the dynamical thermalization was established only later in other studies. In this work we study more generic models based on Random Matrix Theory and social networks with a nonlinear perturbation leading to dynamical thermalization above a certain chaos border. These systems have two integrals of motion being total energy and norm so that the theoretical Rayleigh-Jeans thermal distribution depends on temperature and chemical potential. We introduce the wealth thermalization hypothesis according to which the society wealth is associated with energy in the Rayleigh-Jeans distribution. At relatively small values of total wealth or energy there is a formation of the Rayleigh-Jeans condensate, well studied in physical systems such as multimode optical fibers. This condensation leads to a huge fraction of poor households at low wealth and a small oligarchic fraction which monopolizes a dominant fraction of total wealth thus generating a strong inequality in human society. We show that this thermalization gives a good description of real data of Lorenz curves of US, UK, the whole world and capitalization of companies at Stock Exchange of New York SE (NYSE), London and Hong Kong. It is also shown that above a chaos border the dynamical Rayleigh-Jeans thermalization takes place also in social networks with the Lorenz curves being similar to those of wealth distribution in world countries. Possible actions for inequality reduction are briefly discussed.

Introduction

In 1872 Ludwig Boltzmann published the fundamental work [1] that became the foundation of the theory of statistical physics and thermalization emerging from the dynamical laws of time reversible classical motion of many-body systems. Of course, certain approximations had been used there, thus considering only pair collisions of gas particles. But this was only the first step in the demonstration that the statistical laws follow from the dynamical equations. One of the important results obtained in [1] was the Boltzmann H-theorem that a system entropy is monotonically growing with time or remains constant at the steady-state.

The first numerical experiment with the aim to directly obtain statistical thermalization from dynamical equations of motion was done by Fermi, Pasta, Ulam and Tsingou in 1955 studying the dynamics of a chain of nonlinear oscillators on the most powerful MANIAC I computer (at this time) with an expectation to obtain the thermal energy equipartition between oscillator modes [2]. However, opposite to expectations the conclusion of authors was that "The results show very little, if any, tendency toward equipartition of energy between the degrees of freedom." [2].

Several explanations had been proposed to explain this result. Zabusky argued in [3] that in the continuum limit the Fermi-Pasta-Ulam (FPU) problem is close to the Korteweg-de Vries equation with stable solitons shown to be completely integrable [4], as well as the nonlinear Schrödinger equation [5]. Also, at weak nonlinearity the FPU α-model is close to the completely integrable Toda lattice [6, 7]. Another explanation of absence of thermalization in the FPU problem was given in [8–10] showing that below a certain chaos border, determined by the strength of the nonlinear interactions between oscillators, the system is located in the regime of Kolmogorov-Arnold-Moser (KAM) integrability and only above this border an overlap of nonlinear resonances takes place with emergence of chaos and thermalization. Indeed, above a chaos border numerical simulations demonstrated an emergence of dynamical thermalization with energy equipartition as reported in [9, 10]. Possibilities of low energy chaos in the FPU model were discussed in [11],

It should be pointed out that while impressive mathematical results and theorems were obtained by mathematicians (see e.g. [12, 13] and Refs. therein) they remained usually not applicable to thermalization in physical nonlinear systems which usually have a divided phase space (see [14, 15]) where integrable islands of stable motion are often embedded in a chaotic component. Thus the KAM theorem is valid for unrealistically weak nonlinear perturbations [12, 13] and it is more appropriate to use the Chirikov criterion of overlapping resonances to estimate more realistic parameters for a chaos border [14, 15] (even if this criterion is not working for completely integrable systems like the Toda lattice for example).

An overview of the full richness of the FPU model and various regimes of its nonlinear dynamics has been presented 50 years after [2] in the book [16]. The variety of studies presented there clearly demonstrates that this model has an important role in the investigations of nonlinear dynamics. However, at the same time the variety of different features of FPU dynamics indicates that the FPU model does not belong to a class of generic oscillator systems with nonlinear interactions.

With the aim to capture the generic features of dynamical thermalization the nonlinear random matrix model (NLIRM) was proposed in the work [17], submitted 150 years after the Boltzmann article [1]. In this model, the linear unperturbed Hamiltonian is described by a random matrix that can be also viewed as a system of linear oscillators with complex linear couplings. The chaos in this system is induced only by a nonlinear perturbation that can be local or can have a certain interaction range. Thus in this model the unperturbed properties of eigenmodes and eigenenergies are described by the generic Random Matrix Theory invented by Wigner for a description of the spectra of complex nuclei, atoms, and molecules in many-body quantum mechanics [18]. Indeed, RMT finds a variety of applications in multiple areas of physics [19, 20] including systems of quantum chaos where the dynamics is chaotic in the classical limit [21, 22].

In [17] it was shown that above a certain chaos border the dynamical thermalization takes place leading to the Rayleigh-Jeans thermal distribution (see Eq. (I.1 below) well known in classical thermodynamics [23, 24]. However, the dynamics of the NLIRM system has two integrals of motion being the total energy and norm (or probability that is very natural for quantum evolution). Due to this the Rayleigh-Jeans distribution is characterized by temperature and chemical potential. Such a situation appears in various classical systems including dynamics of nonlinear waves (see e.g. [25]). In fact this type of thermal distribution was described and experimentally observed for light propagation in multimode optical fibers (see e.g. review [26] and Refs. below). The important feature of the Rayleigh-Jeans thermalization is the condensation of a main fraction of system norm or probability at the lowest energy modes of the system. However, in [26] the emergence of such thermalization and condensation was attributed to the turbulence like energy flows similar to those of the Kolmogorov-Zakharov turbulence spectra of nonlinear waves [25] (even if it is stated [26] that the dynamics is Hamiltonian). In contrast, it is argued in [17, 27] that such Rayleigh-Jeans thermalization and condensation appear due to dynamical chaos emerging above a chaos border while below this border the thermalization is absent and the system is located in the integrable KAM regime. Certain similarities of this condensation with the Fröhlich condensate proposed for molecular systems at room temperature [28, 29] are discussed in [27]. The striking applications of Rayleigh-Jeans thermalization are discussed in this work.

This work is composed of two parts. In the first Part I, we push forward the Wealth Thermalization Hypothesis according to which the wealth is associated with system energy and the wealth distribution in the human society is described by the Rayleigh-Jeans thermalization and condensation which are at the origin of strong inequality in the world. The comparison of the obtained thermalization results with the real data of wealth inequality in countries and stock exchange markets confirms the validity of the Rayleigh-Jeans thermal description. In the second Part II, we provide certain additional arguments and justifications for this hypothesis. In particular, we argue that social networks, actively investigated in the network science and society (see e.g. books [30, 31]), provide a reliable model of social relations in the society. While the previous studies of social networks describe the social relations and links only in the frame work of linear matrix algebra we introduce a nonlinear interaction in such social

networks. Similarly to the NLIRM results [17] our studies show that above a certain chaos border for the strength of the nonlinearity dynamical thermalization takes place in social networks being well described by the steady-state Rayleigh-Jeans distribution. This gives an additional support to the Wealth Thermalization Hypothesis. In this way the problem of emergence of statistical laws from dynamical equations of motion finds new application perspectives.

The main results of this research are presented in Part I for links between wealth inequality and Rayleigh-Jeans thermalization and in Part II for dynamical thermalization in social networks supporting the Wealth Thermalization Hypothesis discussed in Part I. Figures in there are marked as Fig.IXX and Fig.IIXX respectively. Additional material and Figures are presented in Appendix A related to Part I and Appendix B related to Part II, in the Appendix A and B Figures are marked as Fig. AXX and Fig.BXX omitting the word Appendix A or B.

Part I: Wealth Thermalization Hypothesis

I.1 Prologue I

The wealth distribution in the human society is characterized by a striking inequality (see e.g. [32–34]). Thus for the whole world 50% of the population owns only 2% of total wealth, while 10% of population owns 75% of total wealth and 1% of population owns 38% of total wealth [33].

The distribution of wealth is usually described by the Lorenz curve [34, 35] which gives the dependence of accumulated normalized wealth $0 \leq w \leq 1$ on the cumulated normalized fraction of population or households $0 \leq h \leq 1$. Thus the equipartition of wealth corresponds to the diagonal $w = h$ and the doubled area between diagonal and the Lorenz curve $w(h)$ determines the Gini coefficient $0 \leq G \leq 1$ [34, 36]. Values of G can be found in [37] for world countries in 2021 being in the range $0.59 < G < 0.90$; for the whole world $G = 0.889$.

The sharing of wealth varies from country to country but the global features remain rather similar with a big fraction of very poor population with scanty wealth and a very small fraction of rich people having a significant fraction of a country's total wealth. This gives an insight that some fundamental underground reasons can be at the origin of this inequality.

Diverse methods of statistical mechanics and physical kinetics [23, 24, 38] have been proposed and used by different research groups [39–47]. Various models of interacting agents are investigated including Random Asset Exchange models [39–47]. In several of these models there is appearance of some kind of oligarchic phase with a significant wealth accumulation by a group of agents [42, 45–47]. The specific arguments are presented in a favor of the Boltzmann-Gibbs type description of distribution of money, wealth and income [41, 43]. Also a nonlinear Fokker–Planck description of asset exchange is proposed [45, 46] with emergence of oligarchic phase. A few important elements are stressed in [45, 46]: the conservation of two integrals of system evolution being the total wealth and total norm (or number of agents), the argument in favor of consideration of wealth instead of money based on the small-transaction approximation. The conservation of two integrals is rather natural assumption since a Gross

domestic product and population of a country or the whole world are only weakly changed on a typical time scale of one year.

The above models give interesting insights for understanding of certain features of wealth distribution in the world countries but they remain model specific and their universality remains questionable. The universality of the Boltzmann-Gibbs thermal distribution is the ground element of the approach developed in [41, 43] but it does not capture emergence of a huge condensate of poverty in various countries.

Our studies here are based on the Wealth Thermalization Hypothesis (WTH) according to which the wealth of a country is described by the Rayleigh-Jeans (RJ) thermal distribution:

$$\rho_m = \frac{T}{E_m - \mu} \text{ (RJ)}. \tag{I.1}$$

Here we assume that the system wealth has certain states $0 \leq m < N$ with energies E_m and the population probabilities in these states are ρ_m. Thus a systen wealth is associated with a system energy. Also in (I.1) the parameters T and $\mu(T)$ are the system temperature and its chemical potential dependent on T. As in [45] there are two conserved integrals of motion being the total norm of population, fixed to be unity for convenience, $\sum_m \rho_m = 1$, and the system average wealth being its total energy $\sum_m E_m \rho_m = E$. For a given system energy E and unity norm these two integrals of motion determine the system temperature T and its chemical potential $\mu(T)$. The entropy S of the system is determined by the usual relation [23, 24]: $S = -\sum_m \rho_m \ln \rho_m$ with the implicit theoretical dependencies on temperature $E(T)$, $S(T)$, $\mu(T)$.

The RJ thermalization (I.1) is universal and describes a variety of classical systems [23, 24] including nonlinear waves [25], light propagation in multimode optical fibers with a nonlinear media [48–53], dynamical thermalization for nonlinear perturbation of the Random Matrix Theory (RMT) [17] and the nonlinear Schrödinger equation (NSE) in quantum chaos billiards [27]. It is pointed out in [18–20] that RMT finds a variety of applications in multiple areas of physics including nuclei, complex atoms and systems of quantum chaos whose dynamics is chaotic in the classical limit. Thus almost any physical nonlinear interaction above a chaos border [17] leads to dynamical RJ thermalization (I.1). An example of such a system can be an ensemble of N nonlinear RMT oscillators with random frequencies $\omega_m \propto E_m$ of an ensemble of N agents with nonlinear interactions leading to the RJ thermalization (I.1). The thermalization can have a dynamical origin when chaotic nonlinear dynamics leads to (I.1) or it can appear due to an external thermal bath. We suppose that for WTH a dynamical origin is more adequate since in a first approximation on a scale of one year a country or the whole world can be considered to be quasi-isolated from slow external processes.

Due to the presence of two integrals of motion, energy and norm, RJ thermalization has the phase of RJ condensate emerging at relatively low total energy E or low temperature T [27, 49, 50]. Thus at low energy and a big number of oscillators, as in [17], or a big number of interacting agents, the fraction of RJ condensate is approaching unity being concentrated at a vicinity of the ground state energy E_0 being zero or very close to zero [27]. Thus the RJ condensate (I.1) very naturally has a huge fraction of very poor agents that naturally describes the huge world wealth inequality where 50% of population owns only 2% of the total wealth [33]. Below we describe in detail

various consequences of WTH (I.1) and compare the results of this theory with real Lorenz curves of certain countries and the whole world.

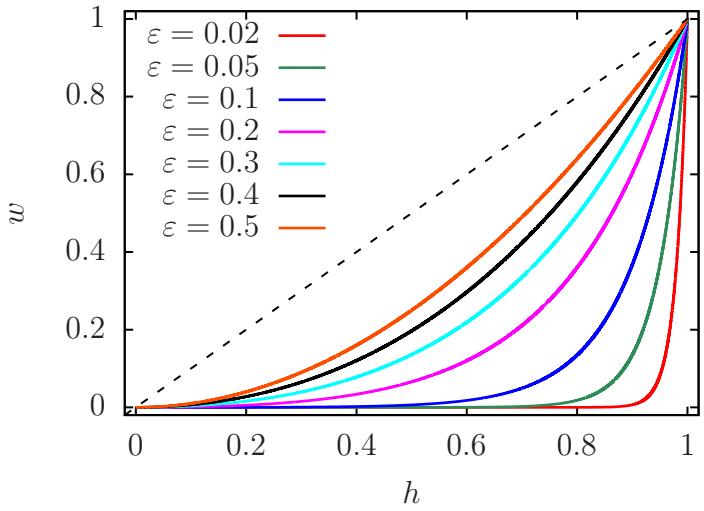

Fig. I.1 Lorenz curves for the RJS model with the linear spectrum $E_m = m/N$ (for $N = 10000$) for different values of the rescaled energy $\varepsilon = E/B$. The x-axis corresponds the cumulated fraction of households (h) and the y-axis to the cumulated fraction of wealth (w). The dashed line is the line of perfect equipartition $w = h$. The Gini coefficients G for all curves are $G = 0.9600, 0.9000, 0.8006, 0.6250, 0.4990, 0.4066, 0.3333$ (bottom to top).

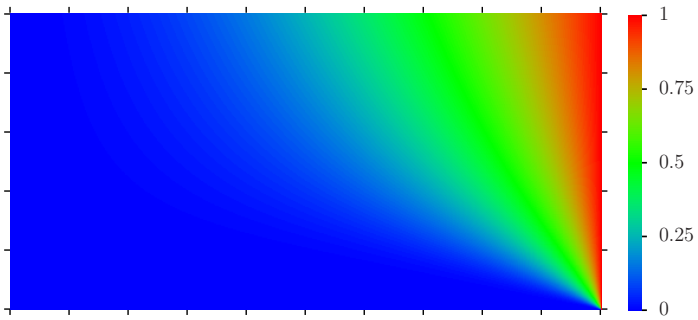

Fig. I.2 Color plot of wealth w from Lorenz curves of the RJS model ($N = 10000$). The x-axis corresponds to the fraction of households $h \in [0, 1]$ and the y-axis to the rescaled energy $\varepsilon = E/B \in [0, 0.5]$. The ticks mark integer multiples of 0.1 for h and ε.

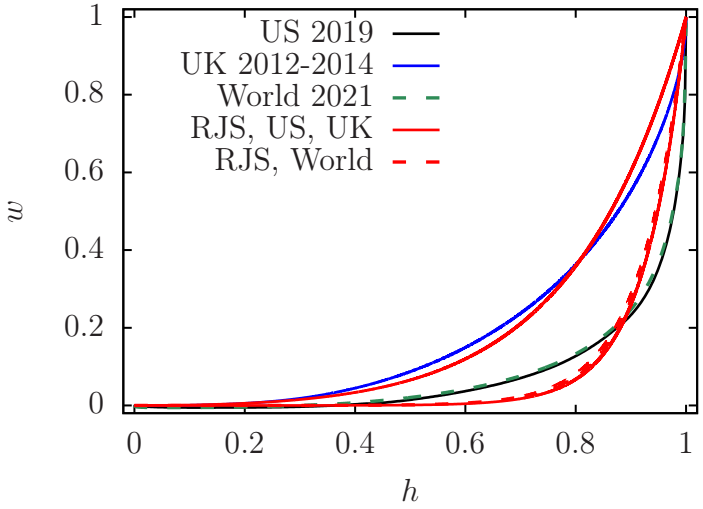

Fig. I.3 Comparison of the Lorenz curves for US 2019 (black), UK 2012-2014 (blue), World 2021 (dashed green) with those of RJS model (red curves; $N = 10000$); US and World curves are rather close. For the three referenced curves Gini coefficients are $G = 0.852$, 0.626, $G = 0.842$ respectively and the rescaled energies $\varepsilon = E/B$ of RJS model are respectively fixed as $\varepsilon = 0.07420$, $\varepsilon = 0.1996$, $\varepsilon = 0.07911$ so that the corresponding Gini coefficients match the referenced data.

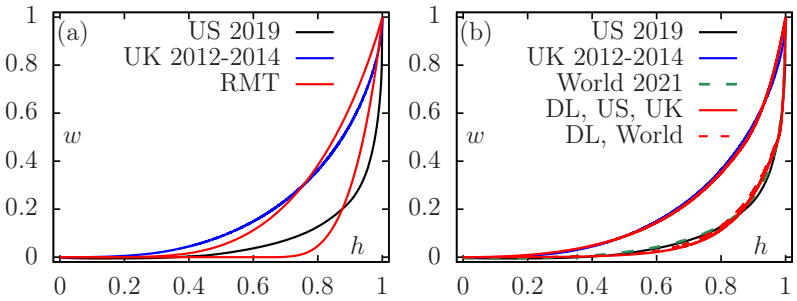

Fig. I.4 Both panels compare the Lorenz curves for different data sets (black for US 2019, blue for UK 2012-2014 and green dashed for World 2021) with those of the RMT model (a) and the DL model (b). As in Fig. I.3 the Gini coefficients G of the reference curves are used to fix the rescaled energy $\varepsilon = E/B$ of the corresponding model such that the model curves (red) have the same G. For the RMT model (a) only two data sets are shown $\varepsilon = 0.07996$ (US) and $\varepsilon = 0.2027$ (UK). For the DL model (b) the parameter values are $a = 16$ (US and World) and $a = 3$ (UK). These values are fixed to have a best possible fit of the model data with those of the reference curves. The chosen values $\varepsilon = 0.01434$ (US), $\varepsilon = 0.1355$ (UK), $\varepsilon = 0.01535$ (World) match the G values of the reference data. In (b) the curves for US and World are rather close and a zoomed view is given in Appendix Figure A.4. In (a) the RMT Lorenz curves are shown for one realization of a random matrix, other realizations give practically the same curves.

I.2 RJ thermalization and condensation

We start from a model with N equidistant energy levels $0 \leq E_m = m/N \leq B$ located in the energy band of total width B. This corresponds to certain levels of wealth for N agents with a fraction of agents on level m being ρ_m. The conserved average system energy is $E = \sum_m E_m \rho_m$ and the dimensionless parameter $\varepsilon = E/B$ determines its fraction with respect to the maximal system energy B. We call this model the RJ standard (RJS) model. On the basis of WTH with RJ distribution (I.1) the local (normalized) wealth on level i is $(E_i/E)\rho_i$ and the cumulated wealth on levels $[0, m]$ is $w = \sum_{i=0}^{m} (E_i/E)\rho_i$ with the cumulated fraction of population or households $h = \sum_{i=0}^{m} \rho_i$. Computing both sums for all values of $m = 0, 1, \ldots$ provides the Lorenz curve $w(h)$. Since the Lorenz curve describes the normalized distribution of cumulated fractions of wealth $w \in [0, 1]$ and households $h \in [0, 1]$ we use the ratio E_i/E (since $E = \sum_i E_i \rho_i$) in the definition of wealth ensuring that $w = 1$ at $h = 1$ for the total population. At given ε the relation (I.1) and two integrals of energy and norm determine the physical parameters T, μ, S. In our numerical studies we use $N = 10000$ which practically corresponds to the continuous limit with results independent of N. The dependencies of T and μ on ε in the RJS model are shown in Appendix Figure A.1. As discussed in [17, 27] for $\varepsilon > 1/2$ the temperature T becomes negative and at ε close to unity there is a formation of an RJ condensate on highest energy levels with $E_m \to B$ (see Appendix Figure A.2). Many unusual properties of RJ thermalization have been discussed in [17, 27] but for convenience we provide some details in Appendix and Figures A.2, A.3 show the dependence of ρ_m on E_m/B for certain values of ε with a clear formation of an RJ condensate at small ε or $1 - \varepsilon$. Even if the regime with negative temperatures has been realized in fiber experiments [48, 53] we consider that such a regime is not applicable to human society and hence we consider only the range with $0 \leq \varepsilon \leq 1/2$.

The Lorenz curves for the RJS model at several ε values are shown in Fig. I.1. Due to RJ condensate there is a very high fraction of poor households f_p (with $w \leq 0.02$) and a small fraction of rich ones f_r (with $w \geq 0.75$) who owns a huge fraction of total wealth. Thus the RJS model naturally describes the big phase of poor households and the oligarchic phase of small fraction of households capturing the big fraction of total wealth. At maximal $\varepsilon = 0.5$ with $(\mu \to -\infty)$ all ρ_m are equal and hence the Lorenz curve is $w = h^2$ with the limiting minimal Gini coefficient $G = 1/3$ for the RJS model. The dependence of cumulated wealth w on h and ε is shown in Fig. I.2. It clearly shows the phase of poor households (blue), corresponding to the RJ condensate, and the oligarchic phase of very rich households (red). Thus we see that the RJ thermal distribution (I.1) describes the main qualitative features of wealth inequality of human society [33].

From Figs. I.1, I.2 we see that for the RJS model the WTH based on (I.1) captures main elements of wealth inequality but it is important to see if it can reproduce the real Lorenz curves for the whole world and specific countries. For this comparison of WTH theory we choose three cases with the Lorenz curves for: the whole world from [33] (integration of front page data gives cumulative w, h values); USA 2019 case from [54] and UK 2012-2014 case from [55]. These real Lorenz curves are compared with those obtained from the RJS model (I.1) in Fig. I.3. For the comparison values of

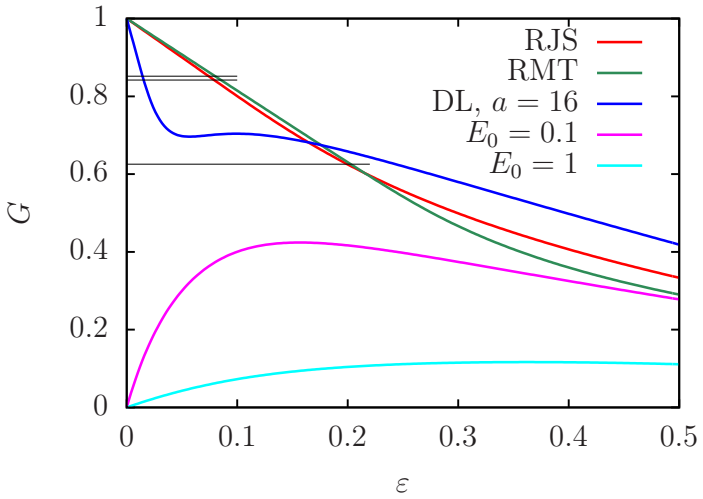

Fig. I.5 Gini coefficient versus rescaled energy $\varepsilon = (E - E_0)/(E_{N-1} - E_0)$ for the RJS model (red), RMT model (green), DL model (blue; only for the case $a = 16$), and the EQI model (pink for the offset $E_0 = 0.1$ and cyan for $E_0 = 1$; same values of E_0 are used in Appendix Figure A.6). The thin black lines show the values of $G = 0.852$, $G = 0.842$ and 0.626 for the data of US 2019, World 2021 and UK 2014. The intersection of these lines with the red and green curves correspond to ε values used in Figs. I.3, I.4.

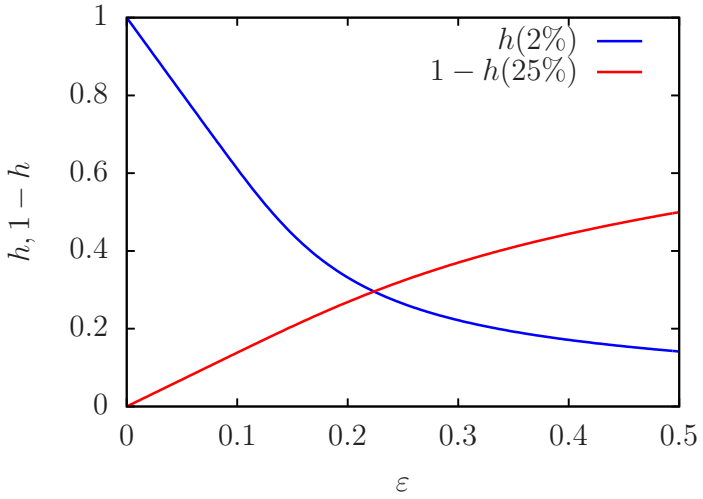

Fig. I.6 Dependence of fraction of poor households $f_p = h(2\%)$ (owning 2% of wealth) and fraction of rich oligarchic households $f_r = 1 - h(25\%)$ (owning 75% of wealth) on the rescaled energy $\varepsilon = E/B$ for the RJS model.

ε are fixed in such a way that Gini coefficient is the same for theory and real data curves. The comparison for UK case shows that there is a good agreement of real and theoretical Lorenz curves even if there is a certain difference for the range $0.9 \leq h \leq 1$. The difference is more visible for USA case and the whole world (Lorenz curves are very similar for these two cases). In Appendix Figure A.4, we also show that the the RJS Lorenz curves have a satisfactory agreement with the Lorenz curves for France and Germany (data are obtained for the year 2010 from [56]).

In view of certain differences between real Lorenz curves and those obtained from RJS model (see Fig. I.3) we also study the case of RJ distribution (I.1) with level energies E_m taken from a random matrix of size $N = 1000$ as it was discussed in [17]. For this RJ RMT model the density of states is $\nu = dm/dE_m = \frac{2N}{\pi}\sqrt{1-E^2}$ with typical eigenvalues in the interval $E_m \in [-1, 1]$ and we shift all E_m to $E_m - E_0$ to have nonnegative values $E_m \geq 0$ in (I.1). The comparison of Lorenz curves for US and UK cases with the results of the RJ RMT model is shown in Fig. I.4a. The similarity between real and RMT model data is a bit less good then those in Fig. I.3 for the RJS model. This shows that the density of states ν can affect the Lorenz curves. Indeed, we have $\nu = $ const. for the RJS model being different from the semi-circle law of RMT model.

To reproduce the real Lorentz curves from [33, 54, 55] in a better way we also analyze a double-linear (DL) model with energies $E_m = m/N$ for $m < N/2$ and $E_m = E_{N/2} + a(m - N/2)/N$ for $m \geq N/2$ at $N = 10000$ with $a = 16$ ($B = 8.5$) for US and World data, and $a = 3$ ($B = 2$) for UK data. In this type of model the density of states takes not one but two values being $\nu = 1$ and $\nu = 1/a$. The existence of two ν values can correspond to a society where high wealth energy E_m values are only accessible to very rich people whose density is lower compared to common people. The comparison of real Lorenz curves with those of the DL model is shown in Fig. I.4b (and its zoomed version Appendix Figure A.5) demonstrating a better proximity between real Lorenz curves and those from the DL model as compared to the results of the RJS model in Fig. I.3. However, the DL model has two fit parameters a, ε while the RJS model has only one ε.

We also remind that for the RJS model the minimal Gini value is $G = 1/3$ that is reached at maximal physical value of $\varepsilon = 1/2$. Thus to have $G < 1/3$, we need to significantly modify the density of states ν. Indeed, we can obtain a perfect complete wealth and energy equipartition with $w = h$ and $G = 0$ for the case when all $E_m = E_0$ values are the same. In this case, the integrals of energy and norm give only one conservation law and all states have the same energy and same population. A small spectrum modification to $E_m = E_0 + m/N$ with a constant energy offset E_0 leads to Lorenz curves being closer to the diagonal with small Gini values $G < 1/3$ and a finite slope $w(h) \approx [E_0/(\varepsilon + E_0)]\, h$ at small h (see Appendix with additional discussion of this model and related Figure A.6). We call this model the equipartition (EQI) model.

We also show color Figures analogous to Fig. I.2 for various models discussed above (see Appendix Figure A.7).

The dependence of the Gini coefficient G on ε is given in Fig. I.5 for the different models. In global the results show that an increase of ϵ leads to a reduction of G. Also in Fig. I.6, we show the dependence of fractions of poor f_p and rich oligarchic f_r

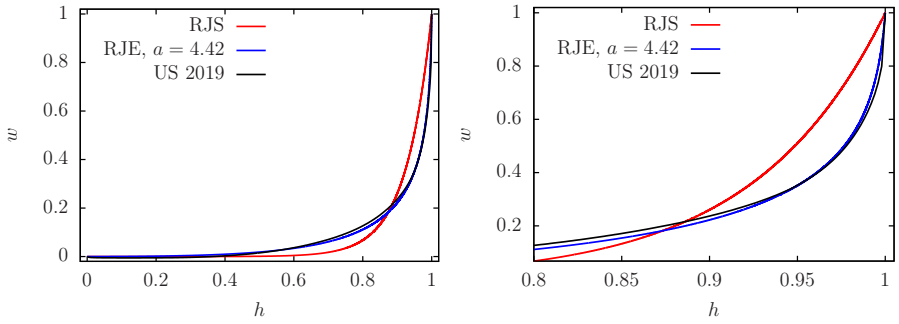

Fig. I.7 Comparison of the Lorenz curve for the data of US 2019 (black) with the corresponding curves for the RJS model (red curve; $N = 10000$) and the RJE model with $a = 4.42$ (blue curve; $N = 10000$). The rescaled energy values $\varepsilon = 0.01233$ (RJE) and $\varepsilon = 0.07420$ (RJS) are obtained by matching the Gini coefficient $G = 0.8515$. The value of a is obtained by a fit from the reconstructed spectrum. The left (right) panel shows the full range $h \in [0, 1]$ (zoomed range $h \in [0.8, 1]$).

households on ε for the RJS model. Thus at $\varepsilon = 0.07$ we have $f_p = 0.73$ and $f_r = 0.097$ that is close to the real values $f_p = 0.53$(US), 0.5(World) and $f_r = 0.09$(US), 0.1 (World) while for UK we have $f_p = 0.32$, $f_r = 0.28$ corresponding to a higher $\varepsilon \approx 0.21$. Furthermore Fig. I.6 shows that the fraction of poor households can be significantly reduced and the fraction of rich households can be increased by increasing parameter ε, thus diluting the oligarchic phase.

Finally, we mention that for the RJS model it is possible to work out analytic expressions (at $N \to \infty$; see Appendix Section 3) for the Lorenz curve and other quantities that accurately match the numerical data (see Appendix Figure A.8). These expressions depend on μ and at small $\varepsilon \leq 0.2$ (with $\mu \approx 0$), we have $w(h) \approx e^{(h-1)/\varepsilon}$ and $G \approx 1 - 2\varepsilon$, matching 3 values of G in Fig. I.1.

I.3 RJ thermalization and universality

Above we presented the comparison of real Lorenz curves of countries and the whole world with the theoretical results of the RJS model based on the physical phenomenon of RJ thermalization and condensation. Since this thermalization is universal for classical systems when the norm and energy are conserved we expect that other systems will be also describe by the RJS model and its extensions.

To check this expectation we analyze the capitalization data for S&P500 companies at the New York Stock Exchange (NYSE), companies of London stock exchange and Hong Kong stock exchange. The data are obtained from the open public sources [57], [58] and [59] respectively. From these sources we construct the real Lorenz curves and compare them with those given by the RJS model for these three cases (see Appendix Section 4 and Figures A.8, A.9, A.10, A.11). The comparison shows that the RJS model qualitatively describes the real Lorenz curves behavior approximately with the same level of agreement as it was for countries and the whole world cases considered before. It is interesting to note that for the case of Dow Jones companies with $N = 30$ companies the Lorenz curve is very close to the case of perfect equipartion with $w = h^2$

(see Appendix Figure A.12) and $\epsilon = 0.5, T \to \infty$ in the RJS model. However, for this case we cannot consider that these companies form an isolated system.

To obtain an RJ extended (RJE) model giving a better agreement with the real Lorenz curves for countries and stocks exchange we make the following extension of the RJS model.

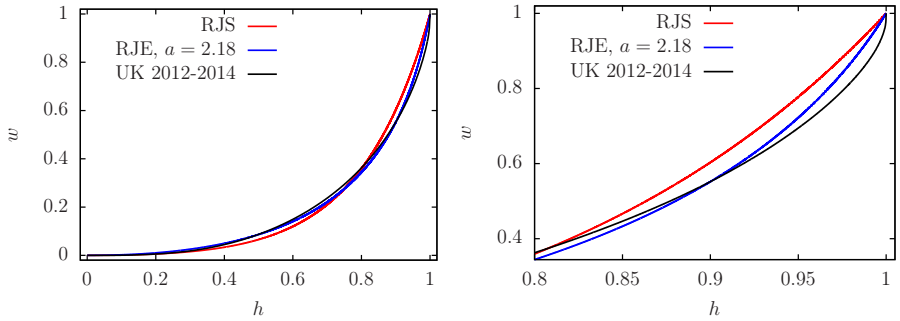

Fig. I.8 Comparison of the Lorenz curve for the data of UK 2012-2014 (black) with the corresponding curves for the RJS model (red curve; $N = 10000$) and the RJE model with $a = 2.18$ (blue curve; $N = 10000$). The rescaled energy values $\varepsilon = 0.1332$ (RJE) and $\varepsilon = 0.1996$ (RJS) are obtained by matching the Gini coefficient $G = 0.6255$. The value of a is obtained by a fit from the reconstructed spectrum. The left (right) panel shows the full range $h \in [0, 1]$ (zoomed range $h \in [0.8, 1]$).

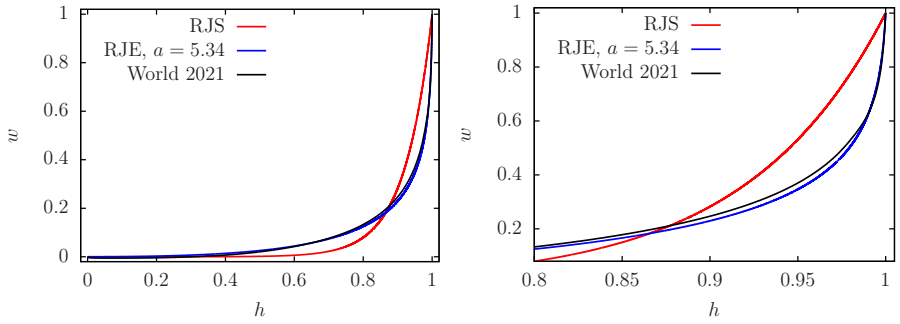

Fig. I.9 Comparison of the Lorenz curve for the data of World 2021 from [33] (black) with the corresponding curves for the RJS model (red curve; $N = 10000$) and the RJE model (I.2) with $a = 5.34$ (blue curve; $N = 10000$). The rescaled energy values $\varepsilon = 0.008553$ (RJE) and $\varepsilon = 0.07911$ (RJS) are obtained by matching the Gini coefficient $G = 0.8420$. The value of a is obtained by a fit from the reconstructed spectrum. The left (right) panel shows the full range $h \in [0, 1]$ (zoomed range $h \in [0.8, 1]$).

The comparison of the different data with the RJS model shows that typically the curves of the RJS model have a slower (final) growth rate. Since the latter is proportional to the energy E_m one could try an extended model where the energy values grow stronger with m. One step in this direction is the DL model which allowed

for a considerable improvement as can be seen in the right panel of Fig. I.4 and also its zoomed version Fig. A.5 in Appendix. Another possibility is to choose an exponential growth of E_m but in such a way that still $E_m \sim m$ for small m. This can be achieved by the formula

$$E_m = \frac{\exp(a\,(m/N)) - 1}{a} \tag{I.2}$$

which we call RJE model (RJ extended or RJ exponential model). Here a is an additional parameter of the model in addition to the value of ε which is now $\varepsilon = E/B$ with bandwidth $B = E_{N-1} \approx (e^a - 1)/a$. In the limit $a \to 0$, we recover simply the RJS model while with increasing values of a the exponential growth of E_m becomes more dominant.

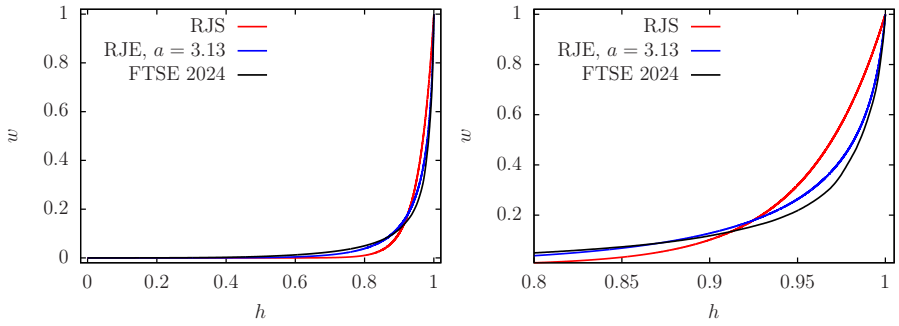

Fig. I.10 Comparison of the Lorenz curve for the data of the London stock exchange FTSE at 31 December 2024 (black; data from Ref. [58]) with the corresponding curves for the RJS model (red curve; $N = 10000$) and the RJE model with $a = 3.13$ (blue curve; $N = 10000$). The rescaled energy values $\varepsilon = 0.01346$ (RJE) and $\varepsilon = 0.04376$ (RJS) are obtained by matching the Gini coefficient $G = 0.9126$. The value of a is obtained by a fit from the reconstructed spectrum. The left (right) panel shows the full range $h \in [0, 1]$ (zoomed range $h \in [0.8, 1]$).

The energy spectrum (I.2) corresponds to a density of states:

$$\nu(E_m) = \frac{dm}{dE_m} = \frac{d}{dE_m}\left(\frac{N \ln(1 + aE_m)}{a}\right) = \frac{N}{1 + aE_m} \tag{I.3}$$

which interpolates between a constant density of states $\nu(E_m) \approx N$ for $E_m \ll a^{-1}$ (as in the RJS model) and a power law decay $\nu(E_m) \approx N/aE_m \sim 1/E_m$ for $E_m \gg a^{-1}$.

To determine optimal values for the parameter a, we compute a reconstructed spectrum from a given Lorenz curve of some given data set (see Appendix Section 5 for a description and more detailed discussion of this spectral reconstruction with Figure A.13) and fit the reconstructed spectrum to the function $E_m \approx C(e^{a\,(m/N)} - 1)/a$ with two parameters C and a. The 2nd parameter C has no importance since one could apply an arbitrary fixed factor on (I.2) without changing the resulting Lorenz curve of the RJE model. This is because the construction procedure of Lorenz curve

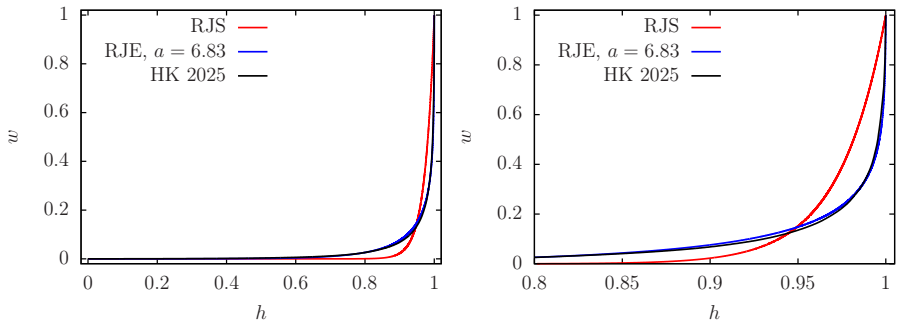

Fig. I.11 Comparison of the Lorenz curve for the data of the Hong Kong stock exchange at 19 June 2025 (black; data from Ref. [59]) with the corresponding curves for the RJS model (red curve; $N = 10000$) and the RJE model with $a = 6.83$ (blue curve; $N = 10000$). The rescaled energy values $\varepsilon = 0.0008381$ (RJE) and $\varepsilon = 0.02648$ (RJS) are obtained by matching the Gini coefficient $G = 0.9471$. The value of a is obtained by a fit from the reconstructed spectrum. The left (right) panel shows the full range $h \in [0, 1]$ (zoomed range $h \in [0.8, 1]$).

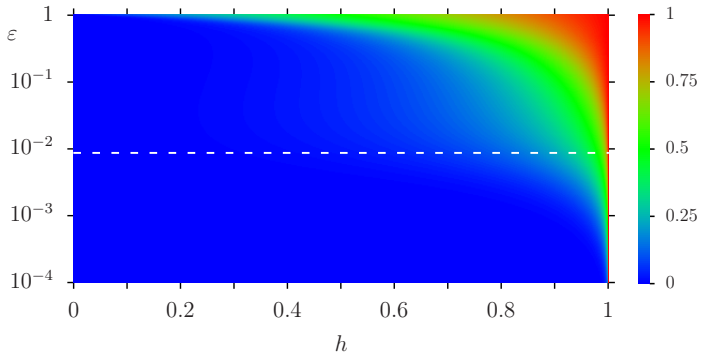

Fig. I.12 Color plot of cumulated wealth w from the Lorenz curves of the RJE model (I.2) ($N = 10000$) with the parameter $a = 5.34$. The x-axis corresponds to the fraction of households $h \in [0, 1]$ and the y-axis to the rescaled energy $\varepsilon = E/B \in [10^{-4}, 1[$ in logarithmic representation. The white dashed line corresponds to the value $\varepsilon = 0.008553$ obtained by matching the Gini coefficient of the RJE model (at $a = 5.34, N = 10000$) with the data of World 2021 from [33] (see Fig. I.9). Note that the color values along the dashed line correspond to the blue RJE curve in Fig. I.9.

involves only the ratio E_m/E (with E being the average energy) so that the global energy scale (or bandwidth B) drops out.

To fix some procedure, we perform the fit of the reconstructed spectrum for two fit intervals for the rescaled level number $x = m/N$ being either $x \in [0, 0.7]$ or $x \in [0, 0.9]$ and select the resulting value of a for which the RJE model provides a closer Lorenz curve to the given data set. In certain cases, the shorter fit interval provides a better fit value of a (cases where the global fit is of reduced quality for small x) and in other cases the longer fit interval is more accurate (cases where the global fit is also of rather good quality for small x).

The results for US 2019, UK 2012-2014, World 2010, FTSE 2024 (London stock exchange) and the Hong Kong 2025 stock exchange are shown in Figs. I.7—I.11, in each case with two panels, top for the full range of $h \in [0, 1]$ and bottom for the zoomed range $h \in [0.8, 1]$. Here, we choose for simplicity the value of $N = 10000$ for the curves of both RJE and RJS models (the RJS curves are also shown for comparison). Other values such as $N = 1000$ or the given size of the data set, give the same Lorenz curves at graphical precision.

In all cases, the agreement of the RJE model with the data is significantly better than the RJS model. In particular for HK 2025, the agreement is close to perfect and even in the zoomed panel it is difficult to distinguish the theoretical RJE curve (blue) from the data (black). For the case UK 2012-2014 the original simpler RJS model was already quite good, but also here the RJE model provides a significant improvement. The RJE curves for US 2019 and World 2021 are also very good, nearly as good as the curve for HK 2025. For FTSE 2024 the agreement of the data with the RJE model is a bit less perfect (since S&P500 captures only about 80% of NYSE) but still clearly better than the RJS model.

We also verified that for three other cases DE 2010, FR 2010 and NYSE 2025 the RJE model gives a good description with values $a = 4.2$, $a = 3.82$ and $a = 2.66$ respectively. Here the results have also a strongly improved agreement of the RJE model with the real data. For NYSE 2025 the agreement is slightly less good compared to other cases (since S&P sector captures only about 80 percent of total NYSE) but even here the RJE model is significantly better than the simple RJS model.

On the basis of presented results we conclude that the RJ thermalization gives a universal description of inequality described by the Lorenz curves for countries and company capitalization at stock exchange.

I.4 Overview of wealth thermalization results

In this Part I we use the WTH approach (I.1) to describe the wealth distribution in a closed system that may be a country or the whole world or a stock exchange. Our main argument is that in such a system interaction of agents is described by nonlinear equations with the conservation of two integrals of motion being total number of agents (norm or total probability analogous to number of system particles) and total wealth (analogous to total system energy). Under these conditions the wealth sharing is described by the universal RJ thermal distribution (I.1) as it is the case for various physical systems [17, 23–25, 27, 49–53]. The striking feature of RJ thermalization (I.1) is that at low system energy (low ε) there is the physical phenomenon of RJ

condensation when a high fraction of total probability is located at lowest energy states that corresponds to the high fraction of poor households with very low wealth and also other small fraction of oligarchic households that monopolizes a big fraction of total wealth. Thus according to the WTH phenomenon a huge wealth inequality in the world [32, 33] finds a natural thermodynamic explication. We show that the WTH theory gives a good description of the Lorenz curves of US, UK and the whole world. It also gives a very good description of capitalization of companies at stock exchange of New York, London, Hong Kong demonstrating the universality of RJ thermalization description.

On the basis of WTH theory we see that a reduction of wealth inequality can be realized by an increase of rescaled system energy ($\varepsilon = E/B$). This point is illustrated in Fig. I.12 which shows a color plot of the Lorenz curves of the RJE model at $a = 5.34$ for different values ε. For this case there is very good matching with the World 2021 data at $\varepsilon = 0.008553$ as can be seen in Fig. I.9 and at larger values of ε the green/red domain with moderate/high wealth increases. The simplest way to reach this is to reduce the global dispersion of wealth (given by B) that can be realized by a high taxation of high wealth revenues.

In the next Part II, we give more justifications for the WTH approach showing that a nonlinear perturbation of social networks leads to the RJ thermalization and condensation.

Part II: Dynamical thermalization in social networks

II.1 Prologue II

During last years social networks gained a significant importance for communications, opinion formation and relations analysis in a human society (see e.g. [30, 31]). Many fundamental properties of such networks have been studied with a variety of their applications established for multiple fields of science. However, all these studies are based on a linear matrix algebra of links between network nodes provided by their adjacency matrix. At the same time it may be interesting and important to analyze the effects of nonlinear interactions between network nodes (agents or users). Indeed, it looks rather natural to assume that in real relations between network agents nonlinear effects should play an important role. With this aim we consider a nonlinear perturbation of two examples of nondirected social networks. These two networks are taken from the database compiled by Newman [60]. The first one represents a collaboration network of scientists studying networks created by Newman [61–63] and the second one is a network of politicians generated from Facebook in [64] with network data of [64] taken from [60].

Both networks are nondirectional so that their adjacency matrix is symmetric and can be viewed as a certain Hamiltonian of a quantum system or a system of coupled linear oscillators. As in [17] a nonlinear interaction is included as a nonlinear frequency shift on a network site (node, agent). The dynamical evolution of the obtained system of nonlinear oscillators has two integrals of motion being the total energy and total norm (probability or number of agents). This corresponds to two integrals of motion

in the evolution of wealth of agents considered in [45, 46] assuming that the wealth is associated to the system energy.

We show that above a certain chaos border of nonlinear interactions a dynamical thermalization takes place in the social networks nonlinear dynamical models leading to RJ thermal distribution (I.1). At low values of the total system energy, or total wealth, RJ condensation emerges in the considered social networks leading to an enormous phase of poor households and a small oligarchic fraction capturing a main part of total wealth. Since social networks can be considered as realistic models of relations in a human society the obtained results for dynamical RJ thermalization provide an additional support and justification for the WTH related to the origins of wealth inequality considered in Part I.

In a certain sense the presented studies of dynamical thermalization in social networks can be considered as an extension of the studies of the FPU problem [2] but with a Hamiltonian part of linear oscillators based on a typical structure of social network links. This linear part of the Hamiltonian is similar to that of the random matrix model NLIRM [17]. We attribute this similarity between two systems to the fact that the nodes in social networks are well connected with each other and only a few link hoppings are required to pass from any node to any other node (see e.g. [30, 31]). Indeed, only 4-5 such link transitions, called the Erdös number, are required to connect any node of the entire Facebook with 8×10^8 users to any other node [65]. Due to this the so called "six degrees of separation" [30, 31], the nonlinear interactions lead to an efficient chaos transition with dynamical thermalization and RJ condensation.

II.2 Model description and numerical methods

In this work, we consider mainly a nondirected network of $N = 379$ known scientists with $N_\ell = 1828$ links from [61, 62], called the *netscience network*, where certain weights are attributed to the links (see Eq. (2) of [61]). In addition, we also present a few results for a larger anonymous nondirected network of $N = 5908$ of politicians and $N_\ell = 83412$ links, called the *politician network*, obtained from Facebook [64]. In this network all links have the same weight being unity. For both cases, links $i \to j$ and $j \to i$ for different nodes $j \neq i$ are counted twice in the definition of N_ℓ and self links $i \to i$ are either absent (netscience network) or taken out (politician network).

For these networks, we define the adjacency matrix A_{ij} by $A_{ij} = w_{ij}$ if there is a link from node j to i and where w_{ij} is the weight of this link (which is 1 for the politician network) and $A_{ij} = 0$ if there is no link $j \to i$. For nondirected networks this matrix is symmetric and has real eigenvalues. We briefly mention that using this matrix A one can define a stochastic matrix S by normalizing the columns of A where eventual empty columns of A for *dangling nodes* are replaced by $1/N$ entries in S but this does not happen for the two networks above. Then the Google matrix G with elements G_{ij} is defined as $G_{ij} = \alpha S_{ij} + (1 - \alpha)/N$ with the damping factor α and its typical value $\alpha = 0.85$. The reason for this is to obtain a unique leading eigenvector of G with eigenvalue $\lambda = 1$, called the *PageRank*, which can be computed efficiently by the power method. However, in the two networks here also for $\alpha = 1$ there is a unique PageRank with a gap between $\lambda = 1$ and other eigenvalues with $|\lambda| < 1$. We refer to

Ref. [69] for a review on the network matrices A, S and G and the PageRank (for the more general case of directed networks) .

We associate to each of these networks a "quantum Hamiltonian" by

$$H = A + \kappa H^{\rm GOE} \tag{II.1}$$

where κ is a small parameter and $H^{\rm GOE}$ is a random GOE-matrix [18–20] with a semicircle density of states of radius unity (at large $N \gg 1$) which corresponds to random gaussian matrix elements with zero mean and variance $\langle (H^{\rm GOE}_{n,n'})^2 \rangle = (1+\delta_{n,n'})/(4(N+1))$. The contribution of $\kappa H^{\rm GOE}$ corresponds to a small static perturbation of the network links which we also expect in real life. In this work, we mainly used one specific random realization of $H^{\rm GOE}$ for a given network of size N but we verified with different realizations that the results do not depend on this choice.

Using the matrix H, we consider the nonlinear oscillator system

$$i\frac{\partial \psi_n(t)}{\partial t} = \sum_{n'=1}^{N} H_{n,n'}\psi_{n'}(t) + \beta |\psi_n(t)|^2 \psi_n(t) \tag{II.2}$$

with complex oscillator amplitudes $\psi_n(t)$ for nodes n where β is the parameter of the nonlinear perturbation. The dynamical system (II.2) has two integrals of motion being the *norm* $\mathcal{N}$ and the *classical energy* $\mathcal{H}$:

$$\mathcal{N} = \sum_n |\psi_n|^2 \quad , \quad \mathcal{H} = \sum_{n,n'} \psi_n^* H_{n,n'} \psi_n + \frac{\beta}{2} \sum_n |\psi_n|^4 \; . \tag{II.3}$$

In fact, the system (II.2) is actually a classical Hamiltonian system with Hamilton function $\mathcal{H}$ if we write $\psi_n = (q_n + i p_n)/\sqrt{2}$ with canonical coordinates q_n and p_n. In this work we fix the norm by $\mathcal{N} = 1$. The case $\mathcal{N} \neq 1$ can be transformed to the case $\mathcal{N} = 1$ by a suitable rescaling of ψ and β.

For $\beta = 0$ this system is simply the time dependent Schrödinger equation for a quantum system with the state $|\psi\rangle = \sum_n \psi_n |n\rangle$ (with $\hbar = 1$). It is useful to diagonalize H by $H\phi^{(m)} = E_m \phi^{(m)}$ with eigenvectors $\phi^{(m)}$ (and components $\phi_n^{(m)}$) and to define amplitudes C_m in eigenmode space by

$$C_m = \sum_n \phi_n^{(m)*} \psi_n \; . \tag{II.4}$$

Here we write more general formulas with the complex conjugate of $\phi_n^{(m)}$ which are also valid for the more general case of complex hermitian matrices H even though in our case H is real symmetric where it is possible to choose real eigenvectors $\phi_n^{(m)} \in \mathbb{R}$. Also we assume that the eigenvectors are orthogonal

$$\sum_n \phi_n^{(\tilde{m})*} \phi_n^{(m)} = \delta_{\tilde{m},m} \tag{II.5}$$

so that the matrix $U_{nm} = \phi_n^{(m)}$, containing the eigenvectors in its columns, is orthogonal (or unitary for complex hermitian H) with the diagonalization identity $H = U\hat{E}U^\dagger$ where $\hat{E}_{\tilde{m},m} = E_m \delta_{\tilde{m},m}$ and the inverse transformation of (II.4) being

$$\psi_n = \sum_m \phi_n^{(m)} C_m \ . \tag{II.6}$$

Using (II.4)-(II.6) one can show that the nonlinear system (II.2) can be rewritten in the eigenmode amplitudes C_m as

$$i\frac{\partial C_m}{\partial t} = E_m C_m + \beta \sum_{m_1,m_2,m_3} Q_{m m_1 m_2 m_3} C^*_{m_2} C_{m_3} C_{m_1} \tag{II.7}$$

with nonlinear transition coefficients

$$Q_{m m_1 m_2 m_3} = \sum_n \phi_n^{(m)*} \phi_n^{(m_1)} \phi_n^{(m_2)*} \phi_n^{(m_3)} \ . \tag{II.8}$$

At $\beta = 0$ the solution of this system is $C_m(t) = e^{-iE_m t} C_m(0)$ and for small values of β there is typically a complicated KAM scenario with a transition to a chaotic region in a large part of the phase space for sufficiently large β.

The two integrals of motion (II.3) can be written in the eigenmode amplitudes C_m as:

$$\mathcal{N} = \sum_m |C_m|^2 \quad , \quad \mathcal{H} = \sum_m E_m |C_m|^2 + \mathcal{H}_{\rm nl} \quad , \tag{II.9}$$

$$\mathcal{H}_{\rm nl} = \frac{\beta}{2} \sum_n |\psi_n|^4 = \frac{\beta}{2} \sum_{m_0,\ldots,m_3} Q_{m_0 m_1 m_2 m_3} C^*_{m_0} C^*_{m_2} C_{m_3} C_{m_1} \ . \tag{II.10}$$

As in [17], we solve the nonlinear system by a symplectic fourth order integrator [66] also known as one of the splitting methods [67, 68]. More details about our implementation of this method can be found in the supplementary material of [17]. This method has the advantage that it respects the symplectic symmetry of the problem. In particular the first integral $\mathcal{N}$ is exactly conserved (up to usual numerical rounding errors) while the second integral $\mathcal{H}$ varies only slightly in time with a small error $\sim dt^4$ and can be used to verify if the choice of dt is appropriate.

As initial condition, we usually start with an eigenstate located at an initial energy mode m_0 with $C_m(t=0) = \delta_{m,m_0}$. For the netscience network, we also consider a few cases where the initial state is localized on some specific node n_0 with $\psi_n(t=0) = \delta_{n,n_0}$ (i.e. $C_m(t=0) = \phi_{n_0}^{(m)*}$). As in [17] an integration time step dt is chosen in such a way that the second integral of motion $\mathcal{H}$ is conserved with a high relative precision being below 10^{-4} for most initial modes (or $\sim 10^{-2}$ for very few boundary modes; note that due to the method the first integral $\mathcal{N}$ is always conserved "exactly" with numerical precision $\sim 10^{-15}$).

II.3 Theoretical elements of RJ thermalization

At sufficient strong values of β and long times t, we expect the nonlinear system to be chaotic and the amplitudes to be somehow ergodic. Assuming a simple behavior $\psi_n(t) \sim 1/\sqrt{N}$ the typical value of the nonlinear energy contribution in $\mathcal{H}$ is $\mathcal{H}_{\rm nl} \sim \beta/N$ which can be neglected at $N \gg 1$ and then we have:

$$E = \mathcal{H} \approx \sum_m E_m |C_m(t)|^2 \tag{II.11}$$

where E is the specific energy value of the integral $\mathcal{H}$. However, in real systems, such as the network generated matrices H considered here, the assumption $\psi_n(t) \sim 1/\sqrt{N}$ may not be realistic, especially at initial times. More generally, the nonlinear energy contribution is $\mathcal{H}_{\rm nl} = \beta/\xi_{\rm IPR}$ where

$$\xi_{\rm IPR} = \left(\sum_n |\psi_n|^4 \right)^{-1} \tag{II.12}$$

is the *inverse participation ratio* (IPR) on the state ψ_n. The IPR corresponds roughly to the number of populated nodes and is broadly used in the problems of disordered solids (see e.g. [70]). The identity (II.11) is still valid if $\beta/\xi_{\rm IPR}$ can be neglected for sufficiently large values of $\xi_{\rm IPR} \gg \beta$. For the case of the eigenmode initial condition with $\psi_n(t) \approx \phi_n^{(m_0)}$ at small times it is the IPR of the eigenstate $\phi^{(m)}$ which fixes the value of $\mathcal{H}_{\rm nl}$ at initial times. We discuss the IPR for the eigenstates of both models in the next sections pointing out that certain eigenmodes may have relatively small IPR values (depending on E_m and κ).

In any case, even if the initial value of $\mathcal{H}_{\rm nl}$ is not very small, we expect that it decays with time t and that (II.11) holds at large times (assuming a chaotic behavior, i.e. no KAM localized state for very small β). This situation corresponds to a microcanonical ensemble with energy conservation (II.11) and an additional second constraint

$$1 = \mathcal{N} = \sum_m |C_m(t)|^2 \ . \tag{II.13}$$

This special microcanonical ensemble can be treated analytically in a simple way only for small energies (temperatures) with E in the lower part of the spectrum E_m and it is more convenient to replace it with a grand canonical ensemble with a probability density

$$P(\{C_m\}) = \frac{1}{Z} \exp\left(-\sum_m \frac{E_m - \mu}{T} |C_m|^2 \right) \quad , \tag{II.14}$$

$$Z = \int \prod_m d^2 C_m \exp\left(-\sum_n \frac{E_m - \mu}{T} |C_m|^2 \right)$$

$$= \pi^N \prod_m \frac{T}{E_m - \mu} = \pi^N \prod_m \rho_m \quad \text{with} \quad \rho_m = \langle |C_m|^2 \rangle = \frac{T}{E_m - \mu} \tag{II.15}$$

being the (thermalized) average *occupation probability of the mode* m. Here the temperature T and the chemical potential μ are determined such that both constraints are verified in average:

$$1 = \sum_m \rho_m \quad , \quad E = \sum_m E_m \rho_m \ . \tag{II.16}$$

(See also [17] and Appendix A.1 below for more details on this.) The probability density (II.14) corresponds to the RJ thermalization for classical fields. The condition $\rho_m > 0$ (for all m) ensures that there is only a unique physically valid solution of (II.16) with either $T > 0$, $\mu < E_1$ or $T < 0$, $\mu > E_N$.

For the numerical system evolution we compute the time average $\rho_m(t) = \langle |C_m(\tilde{t})|^2 \rangle$ over time intervals $t/2 < \tilde{t} \leq t$ for successive discrete time values $t = 2^l \leq t_{\max}$ with $l = 2, 3, \ldots, l_{\max}$ and $t_{\max}$ being typically $2^{22} - 2^{24}$ for the netscience network and $2^{19} - 2^{20}$ for the politician network. These values for $\rho_m(t)$ can be compared to the thermalized theoretical values $\rho_{m,RJ} = T/(E_m - \mu)$ where T and μ are determined from the constraints (II.16) using the value $E = \langle E \rangle = \sum_m E_m \rho_m(t)$ to fix the energy from the numerically obtained values of $\rho_m(t)$.

Note that for the eigenmode initial condition with $C_m(t = 0) = \delta_{m,m_0}$, we typically have $E \approx E_{m_0}$ if $\mathcal{H}_{\rm nl}(t = 0)$ can be neglected. However, in case of relatively large β values and small IPR, with a significant initial value of $\mathcal{H}_{\rm nl}(t = 0)$, we have the more precise relation $E = E_{m_0} + \mathcal{H}_{\rm nl}(t = 0)$ which may give a significant energy shift in the linear part at larger times scales $\langle E \rangle = \mathcal{H} - \mathcal{H}_{\rm nl}(t) = E - \mathcal{H}_{\rm nl}(t) \approx E = E_{m_0} + \mathcal{H}_{\rm nl}(t = 0)$ assuming that $\mathcal{H}_{\rm nl}(t)$ becomes small for large t (for "ergodic states" in a thermalized regime). However, the initial value $\mathcal{H}_{\rm nl}(t = 0)$ may be rather large such that E_{m_0} and $\langle E \rangle$ are rather different. Therefore, it is more appropriate to use $\langle E \rangle = \sum_m E_m \rho_m(t)$ (with numerical values of $\rho_m(t)$ at large t) rather than E_{m_0} to estimate the value of E to determine T and μ from (II.16) and to compute the theoretical RJ values which are to be compared with the numerical results. We see in the next sections that the numerical data $\rho_m(t)$ indeed approach the thermalized theoretical values for sufficiently large t and the netscience network while for the politician network the situation is more difficult due to a limited available integration time.

Another quantity of thermalization is the entropy of the system as a function of either $\langle E \rangle$ or t. There are two points of view to define the entropy. The first one is to use the discrete occupation probabilities ρ_m and define the quantum von Neumann entropy by

$$S_q = -\sum_m \rho_m \ln(\rho_m) \ . \tag{II.17}$$

The latter can also be viewed as the entropy of the associated quantum system of the N levels of the Hamiltonian H with neglected nonlinear term.

The second point of view is based on the underlying classical nonlinear oscillator system with the classical Boltzmann entropy:

$$S_B = -\int \prod_m d^2C_m \; P(\{C_m\}) \ln\left(P(\{C_m\})\, h_B^N\right) \tag{II.18}$$

where $P(\{C_m\})$ is the classical probability density (in some statistical ensemble) of the oscillator amplitudes C_m and h_B is a small constant which compensates the physical dimension in the logarithm. The interpretation of this constant is that we use the discrete probabilities $p(\{C_m\}) = P(\{C_m\})\, h_B^N$ of finding a micro-state in a given elementary cell of volume h_B^N at phase space point $\{C_m\}$ to define the entropy by a sum over a grid of such elementary cells: $-\sum p(\{C_m\}) \ln(p(\{C_m\})$ which gives exactly the above expression (II.18). Below, we give an explicit numerical choice for the parameter h_B which corresponds to a certain constant offset in the definition of S_B.

The formula (II.18) is numerically not convenient since the classical probability density in phase space is not easily available from the trajectory $C_m(t)$ and the integral itself (over many variables) is also difficult to evaluate. In thermal equilibrium, we can replace $P(\{C_m\})$ by (II.14) which gives

$$S_B = \ln(Z/h_B^N) + \sum_m \frac{E_m - \mu}{T} \langle |C_m|^2 \rangle = \ln(Z/h_B^N) + N \tag{II.19}$$

$$= \sum_m \ln\left(\rho_m/h_B\right) + N\,(1 + \ln \pi) \;\; . \tag{II.20}$$

The expression (II.20) is also more generally valid (outside thermal equilibrium) if we assume independently gaussian distributed amplitudes:

$$P(\{C_m\}) \sim \exp\left(-\sum_m a_m |C_m|^2\right) \tag{II.21}$$

with arbitrary coefficients a_m related to $\rho_m = \langle |C_m|^2 \rangle = 1/a_m$. In thermal equilibrium we have $a_m = (E_m - \mu)/T$ but we may assume that (II.21) is also valid at sufficiently large finite iteration times if $\rho_m = 1/a_m$ is computed as some suitable time average over the trajectory. However, we insist that this assumption is not necessarily very exact especially at small t and that outside thermal equilibrium (II.20) is only a convenient approximation of (II.18) in terms of parameters ρ_m obtained from the numerical procedure.

To have reasonable numerical values of S_B which are (mostly) positive, we choose the numerical value $h_B = 1/N^2$ for the data and figures presented in this work (the numerical choice of h_B defines only a certain constant offset in the definition of S_B). Since typical values of ρ_m are $\sim 1/N$ (at rather larger T) this gives indeed $\rho_m \gg h$. In particular for uniform $\rho_m = 1/N$ we have $S_B/N = \ln(N) + 1 + \ln \pi$ which is comparable to $S_q = \ln(N)$. However, at very small times and/or small values of β it is still possible that many values of ρ_m are below $1/N^2$ which gives potentially negative values of S_B. This is an artificial effect of the classical oscillator model and we remind

Table 1 Table of node names with largest eigenvector components. The first three columns show names of 10 top nodes in K_m-rank order ($K_m = 1, \ldots, 10$) obtained by ordering the eigenvectors components of modes $m = 1, 2, 3$ of lowest energies E_m with decreasing values of $|\phi_n^{(m)}|$ (in n for given value of m). The 4th (6th) column corresponds to the K-rank order for the PageRank at $\alpha = 1$ ($\alpha = 0.85$) and the 5th column contains the PageRank probabilities (at $\alpha = 1$) for the node list in the 4th column.

K_1	K_2	K_3	$K(\alpha = 1)$	$P(\alpha = 1)$	$K(\alpha = 0.85)$
Barabasi	Pastorsatorras	Newman	Barabasi	0.03064	Barabasi
Jeong	Sole	Pastorsatorras	Newman	0.02349	Newman
Albert	Vespignani	Vespignani	Jeong	0.01839	Sole
Oltvai	Newman	Watts	Pastorsatorras	0.01736	Jeong
Ravasz	Valverde	Girvan	Moreno	0.01532	Pastorsatorras
Bianconi	Watts	Moore	Vespignani	0.01532	Boccaletti
Demenezes	Ferrericancho	Stauffer	Sole	0.01532	Vespignani
Dezso	Girvan	Sneppen	Boccaletti	0.01226	Moreno
Vicsek	Montoya	Park	Kurths	0.01124	Kurths
Yook	Moore	Lusseau	Vazquez	0.01124	Stauffer

that the entropy of classical systems (oscillators, ideal gas etc.) typically behaves as $S \sim \ln(T)$ for small T with a logarithmic singularity at $T \to 0$. For practical reasons and since S_B is extensive, we consider typically the entropy per mode S_B/N which has comparable numerical values to S_q assuming $\rho_m \sim 1/N$.

We note that in our model the 2nd law of thermodynamics applies to the 2nd entropy S_B and technically it does not apply to S_q. In particular, it is possible that $S_q(t)$ may temporarily decrease with t for certain specific situations (see below) while $S_B(t)$ always increases with t (except for a few cases with a very minimal decrease at very short times and/or small values of β below the chaos border). Furthermore, the usual thermodynamic relation $dS/dE = 1/T$ only holds for $S = S_B$ (and not for S_q), that can be verified by a rather simple calculation from (II.20) using $\rho_m = T(E)/(E_m - \mu(E))$. In particular the terms $\sim d\mu(E)/dT$ cancel exactly due to the two constraints (II.16).

II.4 Netscience network model

In this section, we present the results for the netscience network. Note that additional results and figures related to this section (and also the subsequent sections) are presented (and sometimes discussed in more detail) in Appendix B.

The issue of thermalization depends in a sensitive way on the "ergodic" structure of the eigenvector components $\phi_n^{(m)}$ of the matrix H given in (II.1). We compute the eigenvalues and eigenvectors of this matrix for the netscience network with $N = 379$ for different values of the parameter κ. For certain eigenvectors of modes m with minimal energies E_m, $m = 1, 2, 3, \ldots$, we also determine the ranking index K_m such $|\phi_n^{(m)}|$ is ordered in n in this index, i.e. $|\phi_n^{(m)}| \geq |\phi_{n'}^{(m)}|$ if $K_m(n) < K_m(n')$. The PageRank eigenvector is computed at damping factor $\alpha = 1$ and $\alpha = 0.85$. This is the leading eigenvector of $G(\alpha)$; see text above (II.1) and [69]. Both cases have a similar ranking index K.

In Tab. 1, we present the names of the top 10 nodes for the eigenmodes with $m = 1, 2, 3$ and also both PageRank vectors (at $\alpha = 1$ and $\alpha = 0.85$) ordered by their respective ranking index K_m or $K(\alpha)$. The data in this table was computed for $\kappa = 0$ but the top rankings of the eigenmodes at $\kappa = 0.5$ are actually identical to those of $\kappa = 0$. The top 4 PageRank names at $\alpha = 0.85$ being *Barabasi*, *Newman*, *Sole* and *Jeong* also appear as nodes with strong "community centrality" in [62] (see additional data at Ref. [84] therein). They also play an important role in the PageRank at $\alpha = 1$ with rank values $K = 1, 2, 7, 3$ respectively. *Barabasi* and *Jeong* occupy the positions $K_1 = 1$ and 2 in the first eigenmode ranking for $m = 1$ while *Newman* and *Sole* appear with $K_2 = 4$ and 2 in the 2nd eigenvector. *Newman* also holds the first ranking position $K_3 = 1$ in the 3rd eigenvector. We also mention that each of the three eigenvectors with modes a $N + 1 - m$ ($m = 1, 2, 3$, $N = 379$) at largest energies (not shown in the table) has actually a rather strong overlap with top nodes with the lowest modes m (e.g. $\phi^{(1)}$ and $\phi^{(379)}$ have some common node names in their top ranking index and similarly for the 2nd and 3rd eigenvectors) while there is no overlap between $m = 1$ and $m = 2$.

Fig. II.1 shows in different panels the density of states of H at $\kappa = 0$ and $\kappa = 0.5$ and also the dependence of E_m on m. The global spectral energy band is in the range $E_1 \approx -6.4$ and $E_N \approx 9.7$ (see caption of this figure for 4 bottom and top eigenvalues) with strong gaps of boundary eigenvalues while the density of states has peaked structure around $E = 0$, with a slightly stronger peak for $\kappa = 0$. The global dependence of E_m on m seems rather similar between $\kappa = 0$ and $\kappa = 0.5$ but the zoomed bottom panels show that at $\kappa = 0$ there are several plateau values of degenerate levels at $E = 0$ and $E = -1/p$ for $p = 2, \ldots, 7$ which are lifted by small GOE perturbations. At $\kappa = 0.1$ the degeneracies are only weakly lifted and one can still see the effect of them in the (zoomed) E_m vers m curve while at $\kappa = 0.5$ this curve is essentially a straight line in the shown interval $-0.8 < E_m < 0.2$.

In order to understand these degeneracies we have analyzed the eigenvector structure in more detail by computing for each eigenvector m (at $\kappa = 0$) the *support length* $l(m)$ which we define as the number of nodes n with $\phi_n^{(m)} \neq 0$ (or more precisely with $|\phi_n^{(m)}| > 10^{-12}$ due to the limited numerical precision) and also the IPR (for $\kappa = 0$ and $\kappa = 0.5$).

It turns out that the eigenvectors of the degenerate energies (at $\kappa = 0$) visible in Fig. II.1 have small values of the support length in the interval $8 \leq l(m) \leq 48$ ($l(m) = 48$ for $E_m = 0$). There are also other eigenmodes (non degenerate or only with a double degeneracy) with very small support length in the range $2 \leq l(m) \leq 8$. In total there are 104 out of 379 eigenmodes with $l(m) \leq 48$. These modes are all characterized by energies $E_m = p/q$ with nice rational values (maximal $q = 420$ and other $q \leq 12$). These points are also illustrated in In Fig. B.1 in Appendix B.1 which provides also a more detailed discussion on this.

The IPR values of the eigenvectors at $\kappa = 0$ (in the interval $1.77 \leq \xi_{IPR} \leq 45.98$) are actually not strongly correlated to the support length (see Fig. B.2). Globally the IPR is rather small, also for modes with maximal $l(m) = N$, and for some modes with small $l(m)$ the IPR value may be close to $\xi_{\rm IPR} \approx 20$ (about 50% of the possible maximal value).

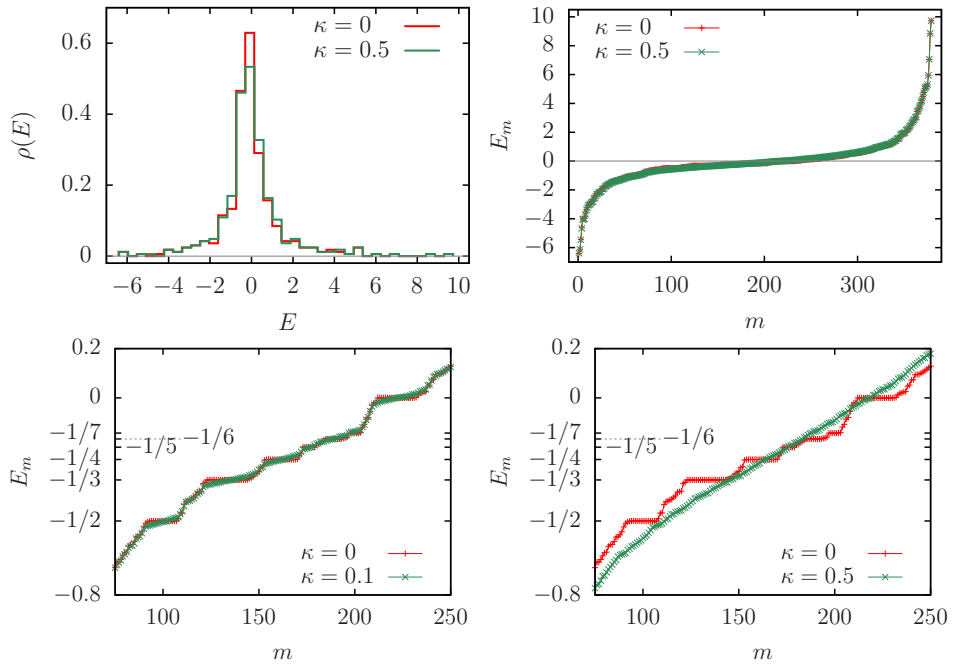

Fig. II.1 Spectral properties of the eigenvalue spectrum of the matrix H for the netscience network with $N = 379$ eigenvalues E_m ($E_1 < E_2 < \ldots < E_N$). The top left panel shows the density of states for $\kappa = 0$ and $\kappa = 0.5$ normalized by $\int_{E_1}^{E_N} dE\, \rho(E) = 1$ with histogramm bin width $dE = 10(E_N - E_1)/N \approx 0.436$. The top right panel shows the eigenvalue E_m versus index m for $\kappa = 0$ and $\kappa = 0.5$. Note that $m/N \approx \int_{E_1}^{E_m} dE\, \rho(E)$. Bottom panels show E_m versus m in a zoomed range for either $\kappa = 0$ and $\kappa = 0.1$ (left) or $\kappa = 0$ and $\kappa = 0.5$ (right). The plateau values for $\kappa = 0$ (red data points) at $E_m = 0$ and $E_m = 1/p$ for $p = 2, \ldots, 7$ correspond to degenerate energy levels. Many eigenvectors of these energies (and other energies with nice rational values) have a small support length $l(m) \ll N$ where $l(m)$ is the number of non-zero values of eigenvector components (with numerical precision 10^{-12}). These degeneracies are lifted by small GOE perturbations at $\kappa = 0.1$ or $\kappa = 0.5$. Bottom and top eigenvalues (at $\kappa = 0.5$) are $-6.38, -6.12, -5.46, -4.67$ and $5.94, 7.06, 8.86, 9.73$. (Bottom/top eigenvalues at $\kappa = 0$ are very close).

Globally, the netscience network and its related adjacency matrix has some specific algebraic structure explaining these modes. Even though the netscience network has only one single component of maximal size $N = 379$ there is some hidden subblock structure in some other base obtained by linear combinations of certain states.

We mention, without going into much details, that for $\kappa = 0$ and even strong interaction values such as $\beta = 10$, typical states with initial modes m_0 in the band center do not thermalize well to all modes E_m according to the RJ-values of ρ_m. For many values of m (corresponding to the degenerate modes) the values of ρ_m stay very small even for long times such as $t = 2^{24}$. For this reason, we focus in the following on the case $\kappa = 0.5$ with a rather significative GOE-perturbation which clearly lifts the degeneracies, where all eigenvectors have the maximal value $l(m) = N$ and where the IPR values are roughly a factor 10 larger than for the case $\kappa = 0$ (see also Fig. B.2). Only a few number of boundary modes, which are clearly in the perturbative regime due to the large gaps, have roughly the same IPR values between $\kappa = 0.5$ and $\kappa = 0$. We assume that it is natural to have in human society a presence of such small random links between society members that can appear due to global information sources (e.g. radio, TV). Thus we present results mainly for the case at relatively small $\kappa = 0.5$ where the RMT perturbation takes out the degeneracies present at $\kappa = 0$.

The values of typical Lyapunov exponents (obtained for initial mode initial conditions), show that at $\beta = 10$ and $\kappa = 0.5$ all modes are in the chaotic regime (see Fig. B.3). Even for a very small value of $\beta = 0.2$ the values of Lyapunov exponent is not very small for modes with $-2 < E_{m_0} < 2$ while boundary modes are in the KAM regime. The basic properties of the theoretical thermalized values of ρ_m for the energy spectrum of the netscience network and the energy dependence of temperature T and chemical μ are illustrated in Figs. B.3 and B.4.

We now turn to the discussion of how well the numerical results for the nonlinear system (II.2) are in agreement with the RJ-theory. As already explained above, we solve (II.2) numerically for the netscience network using initial conditions localized on one energy mode m_0 with $C_m(t = 0) = \delta_{m,m_0}$. Due to the nonlinear term we expect, for sufficiently large values of the parameter β, that the probability states to diffuse approaching to the RJ-distribution. To verify this point, we compute long time averages $\rho_m(t) = \langle |C_m(\tilde{t})|^2 \rangle$ over time intervals $t/2 < \tilde{t} \leq t$ for successive discrete time values $t = 2^l$, $l = 1, 2, \ldots$ with values up to $t = 2^{25}$. Using these numerical averages, we compute S_q and S_B/N using the formulas (II.17) and (II.20) in terms of ρ_m and using $h_B = 1/N^2$ in (II.20). Then we can compare with the theoretical values of S_q and S_B/N using the RJ-thermalized occupation probabilities $\rho_{m,RJ} = T/(E_m - \mu)$. To obtain the values of T and μ, we need to solve the implicit equations (II.16) with a given energy value E as parameter. One possible choice for the comparison is $E = E_{m_0}$ where m_0 is the used initial mode of the numerical data. However, it turns out that the agreement between numerical and theoretical values is better if we choose $E = \langle E \rangle = \sum_m E_m \rho_m$ (using the numerical values of ρ_m at a given time t) to solve (II.16) to obtain T, μ and $\rho_{m,RJ}$. Typically, we have $\langle E \rangle \approx E_{m_0}$ but for boundary modes with small initial IPR, and larger initial nonlinear energy contribution, there may be a significant energy shift between E_{m_0} and the final $\langle E \rangle$ value (see also the discussion at the beginning of the last section around Eqs. (II.11)-(II.13)).

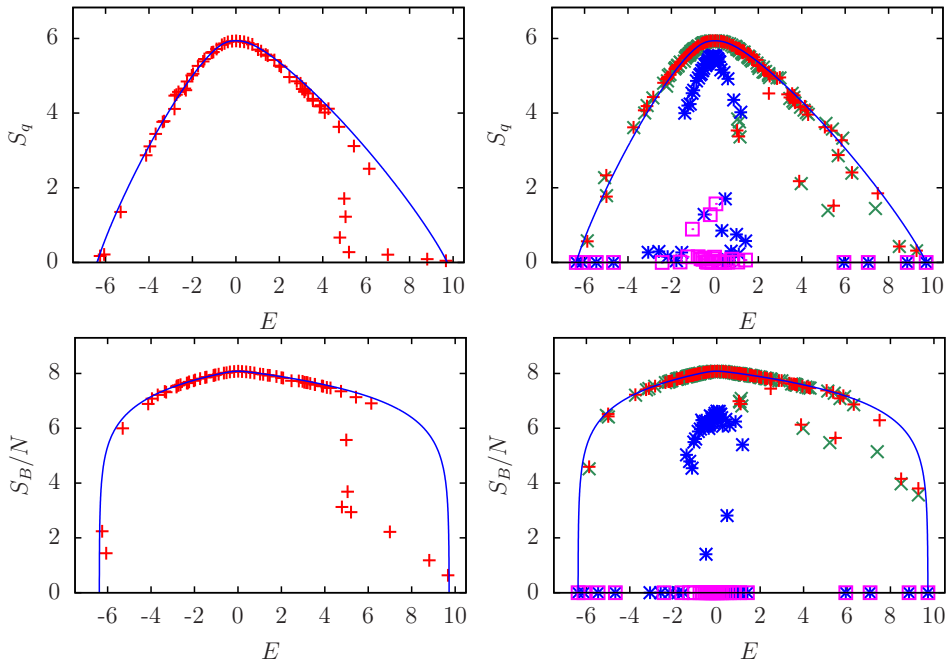

Fig. II.2 Entropy S_q (S_B/N) versus energy E in top (bottom) panels for certain cases of the netscience network with $\kappa = 0.5$, $N = 379$. Left panels correspond to 64 selected modes at $\beta = 4$ and $t = 2^{22}$ (red + symbols) and right panels correspond to 128 selected modes at $\beta = 10$, $t = 2^{22}$ (red + symbols), $\beta = 10$, $t = 2^{20}$ (green $\times$ symbols), 64 modes at $\beta = 0.2$, $t = 2^{22}$ (blue $*$ symbols) and 32 modes at $\beta = 0.05$, $t = 2^{22}$ (pink $\Box$ symbols) In the right bottom panel the data points with $S_B < 0$ (certain points for $\beta = 0.2$ and all points for $\beta = 0.05$) have been shifted up to $S_B = 0$. The blue line shows the energy dependence of the theoretical thermalized entropy for both entropy quantities. S_q (S_B) has been computed by Equation (II.17) (Equation II.20 with $h_B = 1/N^2$) using ρ_m values obtained as the time average $\rho_m = \langle |C_m(\tilde{t})|^2 \rangle$ for $t/2 < \tilde{t} \leq t$ (for $t = 2^{22}$ or $t = 2^{20}$ according to the selected data in this Figure).

Thus Fig. II.2 compares the energy dependence of the numerical data of S_q and S_B/N for a selected number of initial modes with the theoretical values (for $E = \langle E \rangle$) for the netscience network at $\kappa = 0.5$ and different values of β. For $\beta = 4$ and $\beta = 10$ at $t = 2^{22}$ the numerical entropy values agree very well with the theoretical curves for $E \leq 4$ (with 2-3 exceptions at $\beta = 10$). Some of the boundary modes at $E > 4$ have very low entropy values which can be explained by the large energy gaps for theses modes which are very stable with respect to the nonlinear perturbation. They have also slightly smaller Lyapunov exponents compared to the modes with E_m in the band center. Furthermore, the effect of the energy shift due to the initial nonlinear energy contribution pushes these modes more to the right boundary for $\beta > 0$ while boundary modes at the lower part of the spectrum are more pushed to the band center with a reduced chaos border by this effect. For $\beta = 10$ the second set of data with $t = 2^{20}$ is very close to the first set if data at $t = 2^{22}$ (with a few exceptions at $E > 0$) showing that most entropy values are already quite stable for $t \geq 2^{20}$. These results

are confirmed for other values $1 \leq \beta \leq 20$ (data not shown in this or other figures here) with the same kind of exceptions for $E > 4$ and for $1 \leq \beta \leq 3$ a few boundary modes at the lower energy border for $E \leq -5$ are not well thermalized as well.

The entropy data for very small coupling constants $\beta = 0.2$ and $\beta = 0.05$ (blue and pink data points in the right panels) are clearly below the theoretical curves. Note that for S_B/N negative values have been artificially shifted up to zero values for a better visibility. This vertical shift concerns some boundary modes (all modes) for $\beta = 0.2$ ($\beta = 0.05$) with rather strong negative values of S_B (using the parameter $h_B = 1/N^2$). However, for $\beta = 0.2$ the entropy values of the center energy modes in the interval $-1.5 < E < 1.5$ are not very far from the theoretical curves and they still continue to increase in time (at largest available time values). Also their Lyapunov exponents are somewhat stronger than those of the boundary modes at same value of β. These results indicate that center modes at $\beta = 0.2$ are already in a "weak" chaotic regime, but with reduced Lyapunov exponent and much larger thermalization time scales, while boundary modes are still in a pertubative KAM regime. For $\beta = 0.05$ the entropy values are very low for all modes, most S_q values are close to zero and only three values are between 1 and 2 which is 1 to 3 times smaller than the theoretical S_q value. We know that in the energy band center there are many oscillators with very close frequencies E_m and in such cases the KAM theory is not valid and even a very small nonlinearity for e.g. 3 oscillators with equal frequencies have about 50% of the phase space being chaotic (see e.g. [71, 72]).

For the case $\kappa = 0$ and $\beta = 10$ we show in Appendix Fig. B.6 the energy dependence of S_q. Globally there a is similar agreement as for the case with $\kappa = 0.5$ but for this longer iteration time scales $t = 2^{24}$ are required.

In Fig. II.3, we show the dependence of numerical values $\rho_m(t)$ on E_m for the netscience network, $\beta = 10$, $\kappa = 0.5$, several initial modes m_0 and two time values $t = 2^{22}$ and $t = 2^{24}$ (note that $\rho_m(t) = \langle |C_m(\tilde{t})|^2 \rangle$ for $t/2 < \tilde{t} \leq t$). The blue curve corresponds to the thermalized expression $\rho_{RJ}(E_m) = T/(E_m - \mu)$ with T and μ obtained by solving the implicit equations (II.16) with $E = \langle E \rangle = \sum_m E_m \rho_m(t = 2^{24})$. The states with initial modes $m_0 = 4, 46, 292$ are very well thermalized with values of ρ_m that are in good agreement with the theoretical curve. There are somewhat stronger fluctuations for $m_0 = 292$ and the shorter time value $t = 2^{22}$. Even the first (left) boundary mode $m_0 = 1$ is quite well thermalized while the second mode $m_0 = 2$ is not well thermalized with most ρ_m values below the theoretical curve and a few data points strongly above it. The reason for this strange behavior is that the first mode $m_0 = 1$ has a very strong energy shift effect ($E_1 = -6.38$ while $\langle E \rangle = -4.99$) due to its particularly small value of the initial IPR (≈ 2.8, see also first left data point in right panel of Fig B.2 in Appendix B).

The right boundary mode $m_0 = 378$ has a significant nonlinear energy shift being close to maximal possible energy values. Thus the energy integral of motion (energy constraint) does not allow to diffuse to a more ergodic state and the system remains in the integrable KAM regime.

More generally, for modes with $T < 0$ and $E_{m_0} > 0$ the energy shift effect has a tendency to increase the energy to a region with a stronger condensation and due to the energy constraint it is more difficult to thermalize while at $E_{m_0} < 0$ the energy

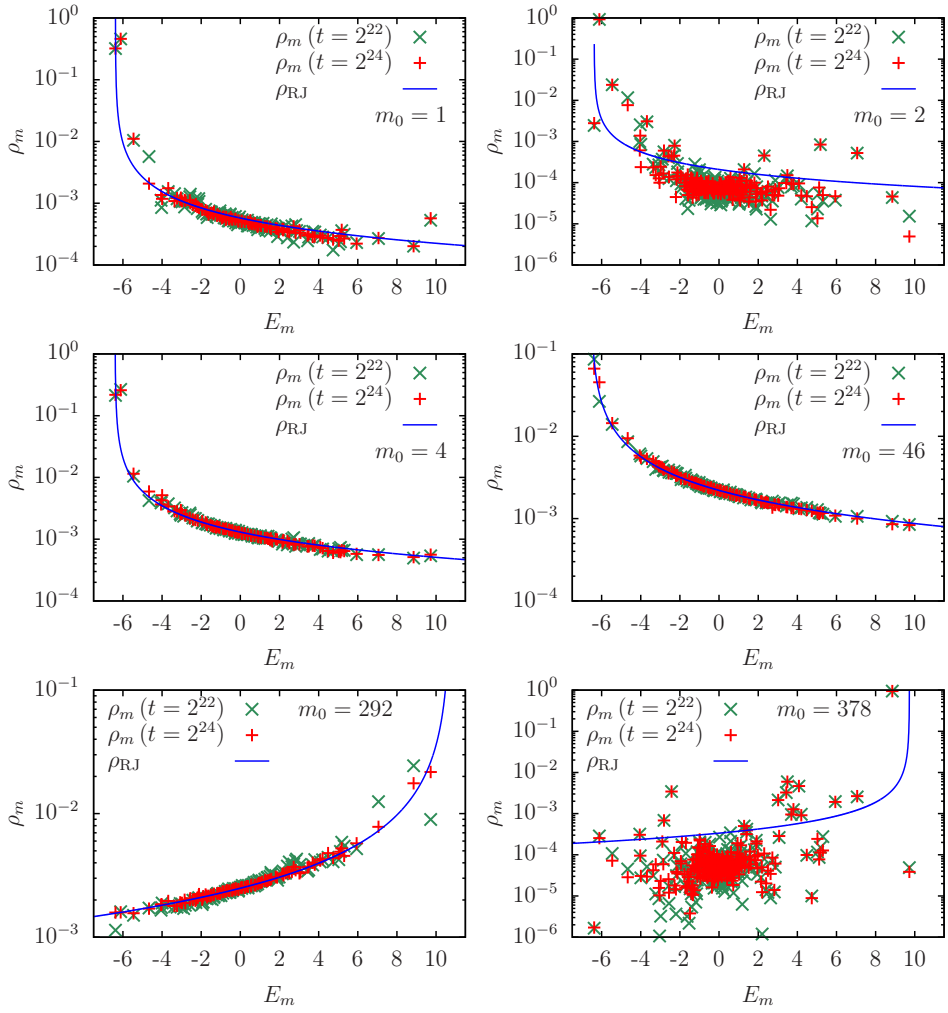

Fig. II.3 Dependence of $\rho_m(E_m)$ on E_m for the netscience network with $\kappa = 0.5$, $\beta = 10$, $N = 379$, the initial condition $C_m(t=0) = \delta_{m,m_0}$ where the initial modes are $m_0 = 1, 2, 4, 46, 292, 378$. ρ_m has been obtained as the time average $\rho_m = \langle |C_m(\tilde{t})|^2 \rangle$ for $t/2 < \tilde{t} \leq t$ for $t = 2^{22}$ (green $\times$ symbol) and $t = 2^{24}$ (red $+$ symbol). The blue curve shows the RJ theoretical curve $\rho_{\rm RJ}(E_m) = T/(E_m - \mu)$ with T and μ determined from the implicit equations (II.16) and using the mean linear energy of the state $\langle E \rangle = \sum_m E_m \rho_m(t = 2^{24})$ for the value of E. The values of T, μ and $\langle E \rangle$ for the 6 initial modes $m_0 = 1, 2, 4, 46, 292, 378$ are $T = 0.003689, 0.001347, 0.008348, 0.01443, -0.02676, -0.003266$, $\mu = -6.388, -6.384, -6.402, -6.555, 10.74, 9.729$ and $\langle E \rangle = -4.99, -5.874, -3.238, -1.088, 0.6025, 8.492$. Note that the case of the initial mode $m_0 = 1$ has finally at large times higher values of T, $-\mu$ and $\langle E \rangle$ than the case for $m_0 = 2$ which is due to a stronger energy shift from the nonlinear energy contributions for $m_0 = 1$.

shift effect facilitates thermalization (to a certain modest degree). This can be seen at the modes $m_0 = 1$ and $m_0 = 4$ and also in Fig. II.2 where many modes with $E > 4$ do not thermalize and their entropy values are clearly below the theoretical curves (for the cases $\beta = 4$ and $\beta = 10$ with good thermalization at $E < 4$). Further two examples of well thermalized states at the smaller value $\beta = 4$ are shown in Fig. B.7 for initial modes $m_0 = 8$ and $m_0 = 54$.

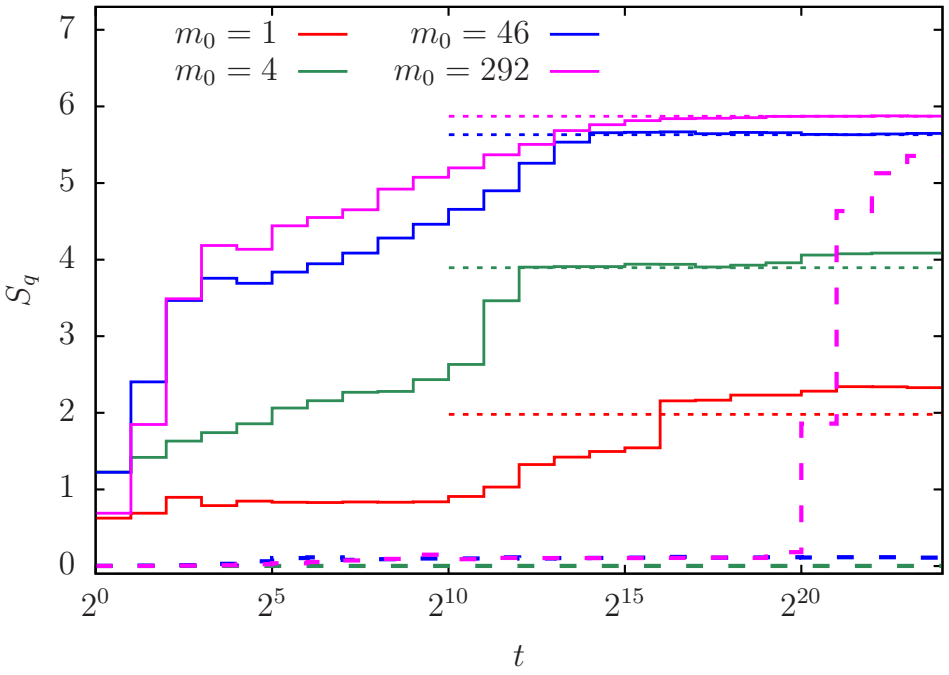

Fig. II.4 Time dependence of S_q for the netscience network with $\kappa = 0.5$, $N = 379$. The full lines with colors red, green, blue, pink correspond to $\beta = 10$ for modes $m_0 = 1, 4, 46, 292$ respectively, the dashed lines correspond to $\beta = 0.2$ (for $m_0 = 4, 46, 292$ with colors green, blue, pink) and the dotted lines indicate the theoretical thermalized RJ values. S_q has been computed by (II.17) using $\rho_m(t)$ values obtained as the time average $\rho_m = \langle |C_m(\tilde{t})|^2 \rangle$ for $t/2 < \tilde{t} \leq t$.

Figs. II.4 and II.5, show the entropy time dependence of of $S_q(t)$ and $S_B(t)/N$ for the 4 well thermalized modes $m_0 = 1, 4, 46, 292$ at $\beta = 10$ (full lines) and also for $m_0 = 4, 46, 292$ at $\beta = 0.2$ (dashed lines of same color for corresponding modes). The plateau values correspond to the used intervals for the time average in the computation of $\rho_m(t)$ between $t/2$ and t for $t = 2^l$, $l = 1, 2, \ldots 24$.

For $\beta = 10$ both entropy quantities increase with time and saturate at values close the theoretical thermalized values (dotted lines). The initial values between $t = 1$ and $t = 2$ are already ~ 1 (for S_q) or ~ 4 (for S_B). Note this figure does not show any data for the very initial time interval $t \in [0, 1[$ with at least 10 (or more) basic integration steps with $dt = 0.1$ (or less) at which there is already some initial diffusion from $S_q = 0$ (or $S_B = -\infty$) of the mode localized initial condition to some finite values.

For S_q (at $\beta = 10$) and the modes $m_0 = 1, 4$ the latest values of $S_q(t)$ are even a bit above the thermalized values. A similar effect for a well thermalized boundary mode was also observed in [17] (for intermediate time scales) and such a behavior is indeed possible since S_q is different from the thermodynamical entropy S_B/N. Furthermore, S_q is not maximal at the thermalized $\rho_{m,RJ} = T/(E_m - \mu)$ values but S_B/N is of course maximal for $\rho_{m,RJ}$ which can be verified by a standard textbook calculation by maximizing (II.17) and (II.20). Mathematically, S_q from (II.17) is maximal at the Gibbs values $\rho_{m,G} = e^{-(E_m-\mu_G)/T_G}$ where the Gibbs temperature T_G and chemical potential μ_G are determined from the implicit equations (II.16) using $\rho_m = \rho_{m,G}$.

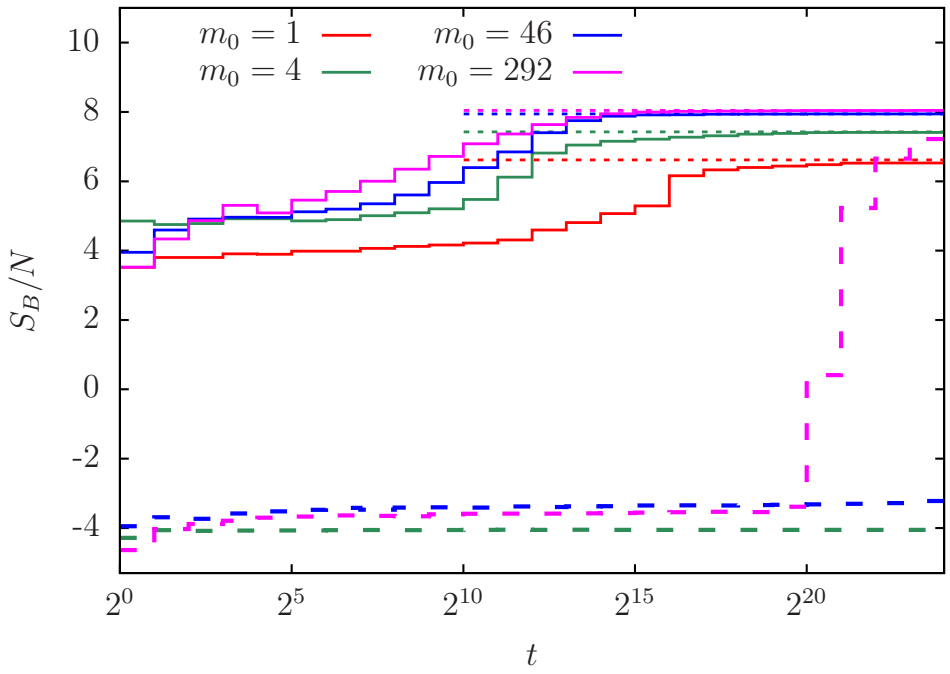

Fig. II.5 Time dependence of S_B for the netscience network with $\kappa = 0.5$, $N = 379$. The full lines with colors red, green, blue, pink correspond to $\beta = 10$ for modes $m_0 = 1, 4, 46, 292$ respectively, the dashed lines correspond to $\beta = 0.2$ (for $m_0 = 4, 46, 292$ with colors green, blue, pink) and the dotted lines indicate the theoretical thermalized RJ values. S_B has been computed by (II.20) using $h_B = 1/N^2$ and $\rho_m(t)$ values obtained as the time average $\rho_m = \langle |C_m(\tilde{t})|^2 \rangle$ for $t/2 < \tilde{t} \leq t$.

For $\beta = 0.2$ the modes $m_0 = 4, 46$ stay localized, even with significant negative values of S_B/N (for the parameter choice $h_B = 1/N^2$) and $S_q \approx 0$. It is likely that there are in the KAM regime. The mode $m = 292$ at $\beta = 0.2$ is very interesting with a very late onset of thermalization at $t \approx 2^{20}$, with a "final" value at $t = 2^{24}$ only slightly below the theoretical value.

We also consider (for $\kappa = 0.5$, $\beta = 1, 4, 10$ and the netscience network) two example states where the initial condition is localized on one specific node n_0 (instead of some eigenmode m_0) with $\psi_n(t = 0) = \delta_{n,n_0}$ (i.e. $C_m(t = 0) = \phi_{n_0}^{(m)*}$) being either *Barabasi*

or *Newman* which are the two top PageRank nodes (see also Table 1). For this case, we show some results in Fig. B.8 of Appendix B. For example the time evolution of both entropy quantities is similar to Figs. II.4 and II.5 with a good convergence to the theoretical thermalized entropy, now in a regime of negative temperature $T < 0$ since the conserved energy is $E \approx \mathcal{H} \approx \beta/2$. Also the data of $\rho_m(t)$ at large times match very nicely the theoretical thermalized curves. For more details on this case see Fig. B.8 and its related discussion in Appendix B.

Finally, the results for dynamical thermalization in the netscience network with nonlinear interactions show that the time evolution is converging to the theoretical RJ distribution for a majority of initial conditions if the system is above a certain chaos border with $\beta > \beta_c$ We estimate that $\beta_c \sim 1$ even if a small chaotic component can survive even below β_c as it as the case in [72]. In the regime of dynamical thermalization the Boltzmann entropy is growing monotonically with time reaching its maximal value in the thermal state in agreement with the Boltzmann H-theorem [1].

II.5 Politician network model

In this section and related Appendix B subsection, we present a few results on the politician network for $N = 5908$ politicians via Facebook using data from [64]. For this case, we do not know the names associated to each node and each of the $N_\ell = 83412$ links has the same unit weight 1 so that $A_{ij} = 1$ for the non-vanishing matrix elements of the adjacency matrix.

Fig. II.6 shows for the cases of this network and different values of κ the density of states $\rho(E)$ of the eigenvalues E_m of the matrix $H = A + \kappa H_{\rm GOE}$ and also the dependence of E_m on m. The global interval for the energies is between $E_1 \approx -25.5$ and $E_N \approx 64.6$, which is significantly larger than for the netscience network. The overall form for $\rho(E)$ and the E_m dependence on m is rather similar to the netscience network but with a somewhat reduced (relative) sub-interval for the bulk of eigenvalues in the center (in comparison to the global energy interval). Now, at $\kappa = 0$, there are two degenerate eigenvalues $E_0 = 0$ (with about 700 modes) and $E_0 = -1$ (with about 40 modes) which produce visible peaks in $\rho(E)$ (a strong one for $E_m = 0$ and a modest one for $E_m = -1$). At $\kappa = 0.1$ and $\kappa = 0.5$ these degeneracies are lifted but their effect on $\rho(E)$ is still visible at $\kappa = 0.5$ with slightly reduced peaks.

The IPR values of the eigenmodes are very small for boundary modes and have a broad distribution for center modes with a reduced probability to have small IPR values at $\kappa = 0.5$ in comparison to $\kappa = 0$. See Fig. B.9 in Appendix B and the related Appendix discussion for more details.

Fig. II.7 shows (same style as Fig. II.3) the dependence of ρ_m on E_m for four example states of the politician network at maximal iterations times $t = 2^{19}$ ($m_0 = 8, 128$) or $t = 2^{20}$ ($m_0 = 1137, 2399$). The latter two modes have been chosen because of their large IPR $\approx 1250 - 1300$ values close to the maximal values in the hope to optimize the chance to observe a rapid thermalization. However, due to the large matrix size $N = 5908$ for the politician network the numerical effort is very high and only the limited time scales used in Fig. II.7 are available. Indeed, the states visible in Fig. II.7 are clearly not yet thermalized at $t = 2^{19}$ or $t = 2^{20}$. However, the time evolution between the two sets of data points at $t/100$ and t still indicates a tendency

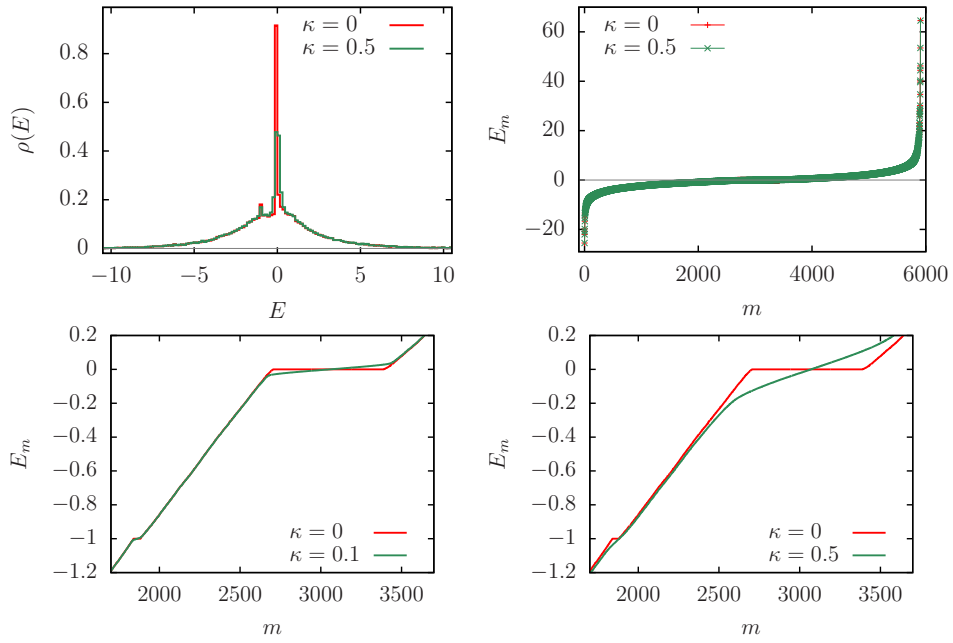

Fig. II.6 Spectral properties of the eigenvalue spectrum of the matrix H for the politician network with $N = 5908$ eigenvalues E_m. The top left panel shows the density of states for $\kappa = 0$ and $\kappa = 0.5$ normalized by $\int_{E_1}^{E_N} dE\, \rho(E) = 1$ with histogram bin width $dE = 10(E_N - E_1)/N \approx 0.153$. The top right panel shows the eigenvalue E_m versus index m for $\kappa = 0$ and $\kappa = 0.5$. Note that $m/N \approx \int_{E_1}^{E_m} dE\, \rho(E)$. Bottom panels show E_m versus m in a zoomed representation for either $\kappa = 0$ and $\kappa = 0.1$ (left) or $\kappa = 0$ and $\kappa = 0.5$ (right). The plateau values for $\kappa = 0$ (red data points) at $E_m = 0$ and $E_m = -1$ correspond to degenerate energy levels lifted by small GOE perturbations at $\kappa = 0.1$ or $\kappa = 0.5$ but the larger (smaller) degeneracy at $E_m = 0$ ($E_m = -1$) has still a strong (modest) effect on the density of states with a strong (small) peak at $E = 0$ and a (slightly) deformed E_m vers m curve. Bottom and top eigenvalues (at $\kappa = 0.5$) are $-25.48, -22.02, -20.76, -19.80$ and $44.46, 46.23, 53.50, 64.58$. (Bottom/top eigenvalues at $\kappa = 0$ are very close).

for convergence to the thermalized curve at much longer time scales numerically not easily accessible. In particular, for the modes $m_0 = 8, 128$ the cloud of data points approaches the theoretical curve, with a delayed "convergence" for the values ρ_m with E_m close to 0 which can be explained by the effects of the strong initial degeneracy at $E_m = 0$ (for $\kappa = 0$) and typical reduces IPR values (also for $\kappa = 0.5$).

Furthermore, the entropy values of the states shown in Fig. II.7 (and some other states we computed) are already rather close to the theoretical value as can be seen in Fig. B.10 in Appendix B. This figure shows for each mode three data points for successive values of t clearly indicating a convergence to the theoretical entropy values. In summary, we can say that the available numerical data provides indications for the onset of thermalization for the politician network but at longer time scales than yet accessible by the numerical method.

Thus the results of this Section show that in large size networks the thermalization time scale can be rather high.

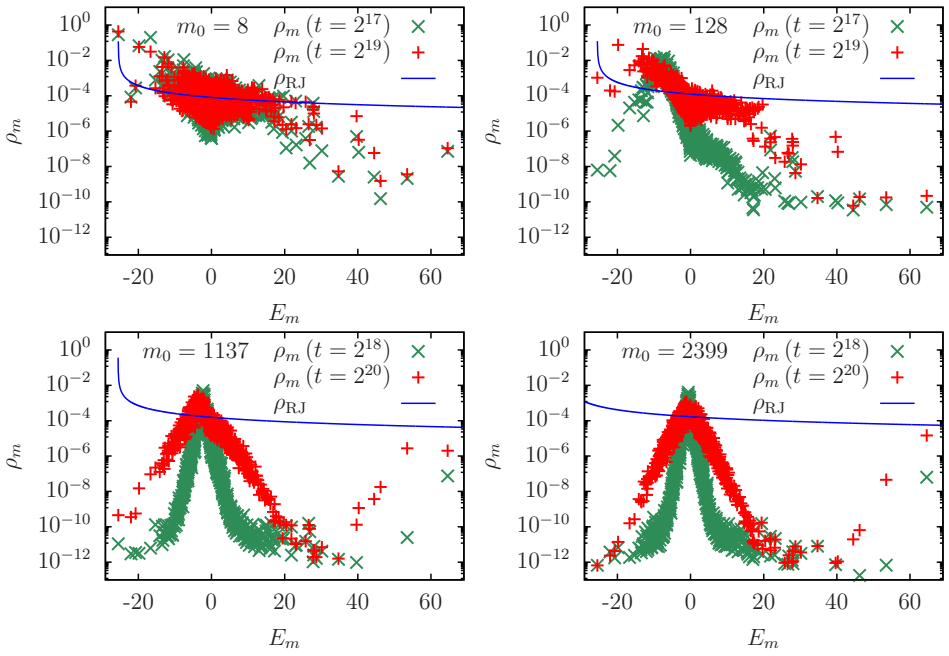

Fig. II.7 Dependence of $\rho_m(E_m)$ on E_m for the politician network with $\kappa = 0.5$, $\beta = 10$, $N = 5908$, the initial condition $C_m(t = 0) = \delta_{m,m_0}$ where the initial modes are $m_0 = 8, 128, 1137, 2399$. ρ_m has been obtained as the time average $\rho_m = \langle |C_m(\tilde{t})|^2 \rangle$ for $t/2 < \tilde{t} \leq t$ for two values of t. The blue curve shows the RJ theoretical curve $\rho_{\rm RJ}(E_m) = T/(E_m - \mu)$ with T and μ determined in the usual way as described in the text (see also the caption of Figure II.3). The values of T, μ and $\langle E \rangle$ for the 4 initial modes $m_0 = 8, 128, 1137, 2399$ (and the larger t value) are $T = 0.002053, 0.003161, 0.003972, 0.005611$, $\mu = -25.49, -25.5, -25.55, -33.53$ and $\langle E \rangle = -13.36, -6.824, -2.083, -0.3803$. For comparison the values of E_{m_0} for these modes are $E_{m_0} = -13.53, -6.84, -2.085, -0.382$. The cases with $m_0 = 8, 128$ ($m_0 = 1137, 2399$) have been computed using the time step $dt = 1/32$ ($dt = 0.1$) for the symplectic integrator up to $t = 2^{19}$ ($t = 2^{20}$).

II.6 Entropy in the RMT model

In Ref. [17], we already studied the thermalization problem for a nonlinear perturbation of a GOE matrix with semicircle radius 1 (corresponding to $A = 0$, $\kappa = 1$ and $N = 64$ in the notations here). However, in [17] only the quantity S_q was computed (and called S there). Therefore, we provide here also a few results for S_B/N using the data of [17]. Specifically, Figs. B.11 and B.12 in Appendix B show the time dependence of $S_q(t)$ and $S_B(t)/N$ for the cases already shown in Fig. S1 of [17] which is actually very similar to Fig. B.11 (the latter is provided for convenience and also shows more theoretical values than Fig. S1 of [17]).

Both entropy values converge for the cases with $\beta = 1$ clearly to the thermalized entropy values. For the initial mode $m_0 = 3$ at $\beta = 1$, we observe that $S_q(t)$ takes at intermediate times ($t \sim 2^{14}$) even larger values (roughly by a factor 1.5) than the thermalized theoretical value before the curve drops to its final value at larger times. This behavior is indeed possible since S_q is not the thermodynamical entropy

of the problem. However, $S_B(t)$ increases monotonically with t all modes (including this mode) and converges in (certain cases) to the thermalized value. For the mode $m_0 = 30$ Figs. B.11 and B.12 show each three curves (of either S_q or S_B/N) at $\beta = 1, 0.1, 0.02$. For $\beta = 1$ ($\beta = 0.1$) there is a rapid (slow/delayed) convergence to the (same) thermalized value while for $\beta = 0.02$ the mode does not thermalize since it is very likely in the integrable KAM regime. Thus the time dependence of $S_B(t)$ is well in agreement with the Boltzmann H-theorem [1].

At the same time we note that a nonmonotonic time dependence of $S_B(t)$ was found in numerical simulations of dynamical thermalization in quantum chaos billiard described by the nonlinear Schrödinger equation [27]. However, in this system the number of linear modes is formally unlimited and there is a question how to define a finite Boltzmann entropy in such a case since the definition (II.20) is diverging in such a case.

II.7 Wealth inequality and Lorenz curves

It is interesting to compute Lorenz curves for the specific spectra of both networks discussed above. We briefly remind the construction procedure which was introduced in Part I. For a given energy spectrum E_m (e.g. for the netscience network at $\kappa = 0.5$), we first compute a shifted spectrum $\bar{E}_m = E_m - E_1$ such that $\bar{E}_1 = 0$ and other $\bar{E}_m > 0$. Then for a specific value of the energy $\bar{E} = E - E_1$ with $\bar{E}_1 < \bar{E} < \bar{E}_N$ corresponding the rescaled energy $\varepsilon = (E - E_1)/(E_N - E_1) = \bar{E}/\bar{E}_N$ we compute the RJ thermalized values of T, μ and ρ_m in the usual way (T and ρ_m are not modified by the shift and for μ the same shift as for E_m is applied). In particular, the relation $\bar{E} = \sum_m \bar{E}_m \rho_m$ is verified. Using these values of ρ_m we compute (for $0 \leq m \leq N$) the cumulated household fraction $h(m) = \sum_{i=1}^{m} \rho_i$ and the associated cumulated wealth fraction $w(m) = \sum_{i=1}^{m} (\bar{E}_i/\bar{E})\rho_i$ such that $h(0) = w(0) = 0$, $h(N) = w(N) = 1$ and $h, w \in [0, 1]$. The set of points $(h(m), w(m))$ for $0 \leq m \leq N$ then provides the Lorenz curve.

To characterize the degree of "inequality" one uses the *Gini coefficient* defined as the area between the line $w = h$ (of perfect "equality") and the curve divided over its maximal possible value if $w = 0$ (i.e. $1/2$ for the area of the triangle below the line $w = h$).

Fig. II.8 shows for the netscience network a certain number of Lorenz curves for different values of the rescaled system energy ε. The largest used value $\varepsilon = 0.38$ is close to the critical value $\varepsilon_c = 0.39622$ at which the transition from $T > 0$ to $T < 0$ appears. As expected at smaller values of ε the curves describe a strong inequality with a value of G close to 1. Here for $\varepsilon \approx \varepsilon_c$ we have $G \approx 0$ and a curve quite close to the line $w = h$ of perfect equality. This is different from the RJS model (of a uniform spectrum) used in Part I where at $\varepsilon = \varepsilon_c = 1/2$ we have found $w = h^2$. Apart from that, for most curves there is a large interval $h \in [0, h_0]$ where $w(h) = 0$ which is due to the very large energy gaps of the first modes at $m = 1, 2, 3, \ldots$ in comparison to the level spacings of modes in the bulk. For $h > h_0$ the curves increase to the final value $w(h = 1) = 1$ and there are rather close to the straight line between $(h_0, 0)$ and $(1, 1)$. This behavior can be modified a bit (at least for the larger values of ε) by choosing an ever stronger value of κ. Fig. B.13 in Appendix B illustrates this for $\kappa = 6$ where the

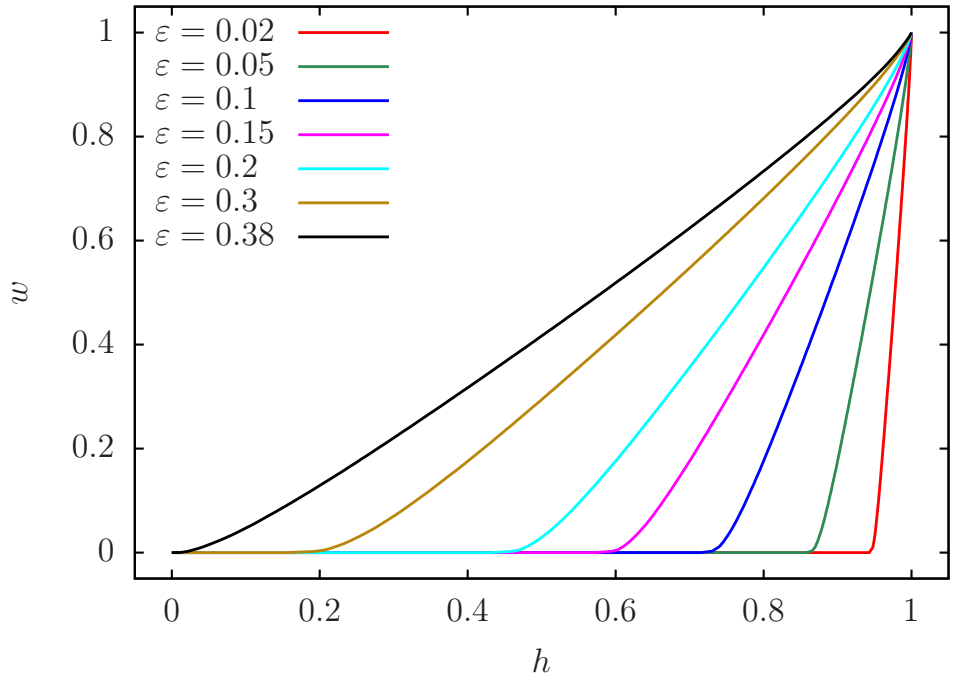

Fig. II.8 Lorenz curves for the netscience network with $\kappa = 0.5$, $\beta = 10$, $N = 379$ for different values of the rescaled energy $\varepsilon = (E - E_1)/(E_N - E_1) = \bar{E}/\bar{E}_N$. The x-axis corresponds the cumulated fraction of households (h) and the y-axis to the cumulated fraction of wealth (w). The largest value $\varepsilon = 0.38$ is slightly below the critical value $\varepsilon_c = 0.39622$ at which the transition from $T > 0$ to $T < 0$ appears. The Gini coefficients G for all curves are $G = 0.9534, 0.8834, 0.7668, 0.5336, 0.6502, 0.301, 0.1321$ (bottom to top).

straight lines are a bit more curved. However, in this case also the density of states is strongly modified and it is rather close to the semicercle law with radius $\kappa = 6$ with a significant reduction of the initial energy gaps.

The results of Fig. II.8 show that e.g. ar $\varepsilon = 0.15$ the phase of absolutely poor households is approximately 60% of all households while the top 10% of most rich households own approximately 32% of total wealth.

Fig. II.9 shows a color density plot for the Lorenz curves for a continuous distribution of $\varepsilon \in [0, \varepsilon_c[$ essentially confirming the observations of Fig. II.8 the length h_0 of the initial interval (with $w(h) = 0$) behaves roughly as $h_0 \approx \varepsilon/\varepsilon_c$.

Figs. II.10 and II.11 are as Figs. II.8 and II.9 respectively but for the politician network. Now the critical value for the transition from positive to negative T is $\varepsilon_c = 0.28297$. The structure of the curves and the color plot are rather similar as for the netscience network but the effect of straight lines for $h > h_0$ is even a bit stronger which is certainly related to the larger initial energy gaps of the politician network.

The results of this section show that the RJ thermalization and condensation in social networks presented in the previous sections leads to the formation of an enormous phase of very poor households and a small fraction of rich households that

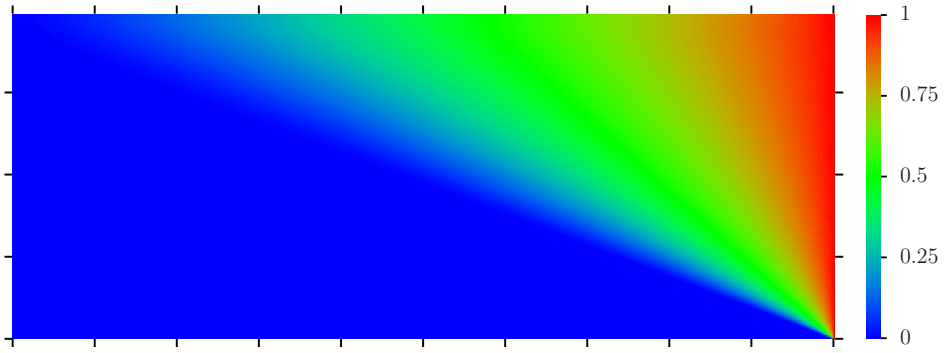

Fig. II.9 Color plot of wealth w from Lorenz curves for the netscience network with $\kappa = 0.5$, $\beta = 10$, $N = 379$. The x-axis corresponds to the fraction of households $h \in [0, 1]$ and the y-axis to the rescaled energy $\varepsilon = (E - E_1)/(E_N - E_1) \in [0, \varepsilon_C[$ where $\varepsilon_c = 0.39622$ is the critical value at which the transition from $T > 0$ to $T < 0$ appears. The ticks mark integer multiples of 0.1 for h and ε.

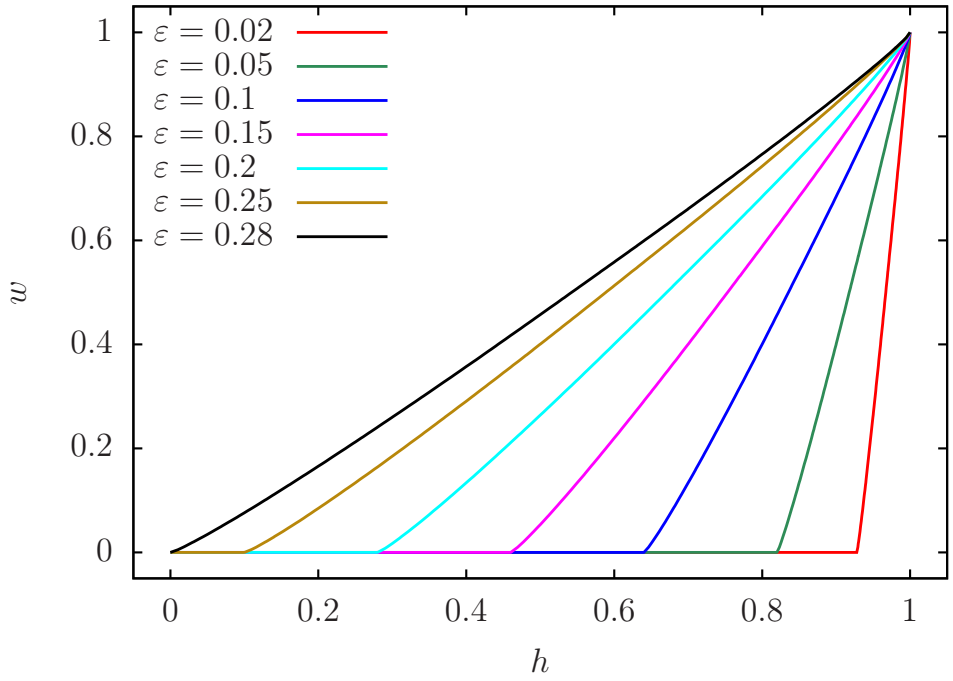

Fig. II.10 Lorenz curves for the politician network with $\kappa = 0.5$, $\beta = 10$, $N = 5908$ for different values of the rescaled energy $\varepsilon = (E - E_1)/(E_N - E_1)$. The x-axis corresponds the cumulated fraction of households (h) and the y-axis to the cumulated fraction of wealth (w). The largest value $\varepsilon = 0.28$ is slightly below the critical value $\varepsilon_c = 0.28297$ at which the transition from $T > 0$ to $T < 0$ appears. The Gini coefficients G for all curves are $G = 0.9328, 0.8321, 0.6642, 0.4963, 0.3284, 0.1605, 0.06647$ (bottom to top).

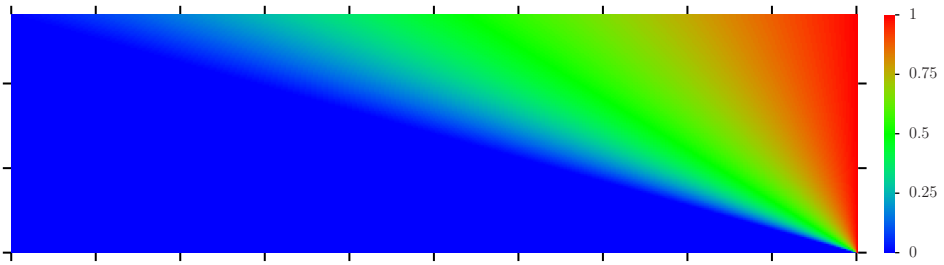

Fig. II.11 Color plot of wealth w from Lorenz curves for the politician network with $\kappa = 0.5$, $\beta = 10$, $N = 5908$. The x-axis corresponds to the fraction of households $h \in [0, 1]$ and the y-axis to the rescaled energy $\varepsilon = (E - E_1)/(E_N - E_1) \in [0, \varepsilon_C[$ where $\varepsilon_c = 0.28297$ is the critical value at which the transition from $T > 0$ to $T < 0$ appears. The ticks mark integer multiples of 0.1 for h and ε.

owns a significant fraction of total system wealth. The presence of a significant energy gap in the energy spectrum of two social networks studied here enhance the fraction of the poor phase comparing to the other spectrum models considered in Part I. The question of how typical such energy gaps are for social networks requires further studies. Another feature of the considered social networks is a strongly peaked density of states approximately at the middle of the energy band. As a result the energies E_m are very flat in this energy region. This is rather different from the RMT model or RJS model of Part I where the density of states is approximately constant in this energy range. We suppose that the origin of this difference is related to the fact that in the considered networks we have links between the members of the same society layer or class: scientists linked to scientists, politicians to politicians. Probably this is a general feature of internet connections where there is little if any distinction between classes of network members. In a real human society there is some kind of natural society statification: factory workers are mainly linked with workers, peasants with peasants, businessmen with businessmen, aristocrats with aristocrats. This feature is well present in a real human society with its society classes and wealth gradient between classes (of course with fluctuations and relatively weak links between classes). Thus it is possible that the society networks should be revised and updated to include the above feature of human society.

II.8 Overview of social networks results

The presented studies of dynamical thermalization in social networks show that chaos in these systems lead to the RJ thermalized distribution if nonlinear interactions are above a certain chaos border. The time scale for onset of this RJ distribution is determined by the strength of the nonlinearity. This time scale can be relatively long. On a first glance this seems rather surprising in view of a rather small number of links to hope and connect any pair of nodes, with the Erdös number $N_E \approx 4 - 5$ [30, 31, 65]. However, such link transitions are provided only by the linear part of system Hamiltonian while only the nonlinear interactions lead to transitions between eigenmodes (see (II.7)) with eventual thermalization. Our results show that the RJ thermalization process in the social networks has close similarities with those in the NLIRM

model [17]. Thus we expect that the Lyapunov exponents λ_m and the thermalization time scale t_{RJ} have a similar to [17] dependence on nonlinearity β and number of oscillators (nodes) where it was found that the typical Lyapunov exponent values are $\lambda \sim \beta^{1.5}/N^{1.9}$. We expect that $t_{RJ} \propto 1/\lambda$ but further studies are required to confirm these dependencies.

The emergence of RJ condensate leads to a formation of an enormous phase with high fraction of total norm located at low energy, or wealth, states. This leads to a massive fraction of poor households in the social networks as it is well seen in the figures of the Lorenz curves in Section II.7. At the same time a significant part of total wealth is captured by a small oligarchic group of rich households. Thus the obtained results for dynamical thermalization in social networks provide a confirmation of WTH origin and highlight the problem of wealth inequality in human society from a new view point.

Discussion and conclusion

In 1955 Fermi, Pasta, Ulam and Tsingu performed the first numerical simulations of a chain of nonlinear oscillators with the aim to find a dynamical thermalization and energy equipartition between the degrees of freedom. However, this model happened to have various specific features so that no tendency to equipartition was found in 1955 [2]. To extend these studies a generic model of coupled oscillators was proposed in [17] on the basis of nonlinear perturbation of Random Matrix Theory showing that chaos leads to dynamical thermalization with the resulting RJ distribution over the linear energy eigenmodes. This model has two integrals of motion being the total energy and total norm (probability). Thus the RJ distribution in this isolated Hamiltonian system is characterized by the system temperature $T(E)$ and chemical potential $\mu(E)$.

In fact the emergence of the RJ thermalization had been studied earlier numerically and experimentally for light propagation in multimode optical fibers [26, 48–53], even if the origin of this thermalization was attributed to the Kolmogorov-Zakharov turbulence [25] without links to chaos and KAM integrability. The emergence of RJ condensation was established numerically [49] and experimentally [48, 50]. The emergence of an RJ condensate and thermalization in quantum chaos fibers with the nonlinear Schrödinger equation was demonstrated in numerical and analytical studies reported in [27]. At the same time it should be pointed out that the Fröhlich condensate for molecules at room temperature, discussed in [28, 29], has also certain similarities with the RJ condensate, even if in [28, 29] the system is considered under external pumping and dissipation (see discussion in [27]).

In Part I we analyzed the consequences of RJ thermalization and condensation associating system energy and norm, both conserved by time evolution. These quantities are related to the global wealth and the number of interacting households which are also conserved as justified in [45, 46]. The performed analysis shows that this WTH description depicts very well the shape of real Lorenz curves of wealth of households for several countries and the whole world. Also the WTH approach well reproduces the Lorenz curves for the stock exchange markets of New York, London and Hong Kong. To provide more arguments in support of the WTH description we study in Part II

the dynamical thermalization in social networks induced by a nonlinear perturbation. Our results show the emergence of RJ thermalization and condensation in social networks with nonlinear interactions between network agents with the interactions being above a certain chaos border. As in Part I the RJ condensation leads to the Lorenz curves with an enormous fraction of poor households and a small fraction which owns a main part of total wealth. On the basis of the results of this work we argue that the WTH description provides new perspectives for the understanding of the nontrivial aspects of the wealth inequality in the world.

Declarations

- Funding: The authors acknowledge support from the grant ANR France NANOX N° ANR-17-EURE-0009 in the framework of the Programme Investissements d'Avenir (project MTDINA).
- Conflict of interest: The authors declare no conflicts of interest.
- Data availability: This work uses specific datasets about wealth data for countries, stock market, network data etc. available at Refs. [31–34, 37, 55–64].

Acknowledgements. We thank A. D. Chepelianskii and L. Ermann for useful discussions. The authors acknowledge support from the grant ANR France NANOX N° ANR-17-EURE-0009 in the framework of the Programme Investissements d'Avenir (project MTDINA).

Appendix A Additional material for Part I

A.1 General features of the thermalization in the RJS model

Here we remind a bit more details about thermalization of the RJS model (see also Refs. [17, 27] for more details). Let us assume that we have N linear classical oscillators with individual energies E_m, $m = 0, \ldots, N-1$ which are coupled by some small nonlinear perturbation (see Ref. [17] for an example) such that there are two conserved quantities being the global (squared) amplitude and total energy:

$$1 = \sum_{m=0}^{N-1} \rho_m \quad , \quad E = \sum_{m=0}^{N-1} E_m \rho_m \tag{A.1}$$

where ρ_m is the time averaged squared amplitude and occupation probability of each oscillator. If the non-linear terms are sufficiently strong or if there is some weak coupling to an external system (which respects both constraints (A.1)) one can assume that the system thermalizes. Applying the framework of the grand canonical ensemble one introduces two parameters: temperature T and chemical potential μ to satisfy both constraints (A.1) in average and it can be shown (see e.g. Ref. [17]) that

$$\rho_m = \frac{T}{E_m - \mu} \quad , \quad T = \frac{E - \mu}{N} \tag{A.2}$$

where the expression for the temperature T is obtained from $\sum_m (E_m - \mu)\rho_m = (E - \mu)$ which follows directly from (A.1). The chemical potential is determined (using standard numerical techniques) by solving the implicit equation:

$$1 = \frac{E-\mu}{N} \sum_{m=0}^{N-1} \frac{1}{E_m - \mu} \tag{A.3}$$

which allows for one physical solution of μ outside the energy interval $[E_{\min}, E_{\max}]$ with either $\mu < E_{\min}$ $(T > 0)$ or $\mu > E_{\max}$ $(T < 0)$ (depending on the value of E we have either $T < 0$ or $T > 0$) such that $\rho_m > 0$. The data presented in this work were obtained by this procedure for different model spectra and certain values of $N = 10000$ (or $N = 1000$ for the RMT model). Concerning the RJS model we have also considered the cases $N = 100$, $N = 1000$ and verified that the obtained Lorenz curves are very close (in graphical precision).

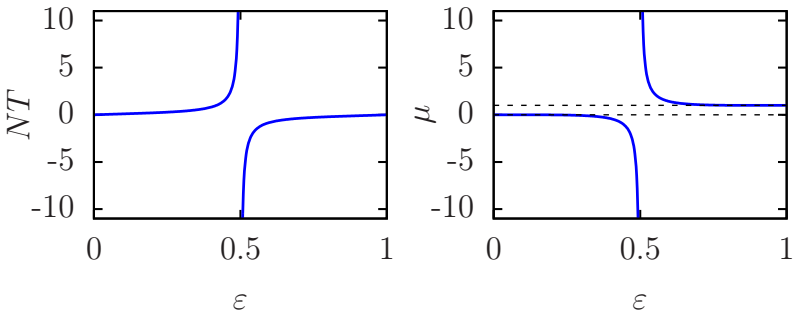

Fig. A.1 The left (right) panel shows the (rescaled) temperature NT (the chemical potential μ) versus the rescaled energy $\varepsilon = E/B$ for the RJS model $E_m = m/N$, $N = 10000$. The dashed black lines in the right panel correspond to the values of $E_0 = 0$ and $B \approx 1$ showing that either $\mu < E_0$ (for $T > 0$) or $\mu > B$ (for $T < 0$).

As illustration Fig. A.1 shows for the RJS model with $E_m = m/N$, $m = 0, 1, \ldots, N-1$, $N = 10000$ both T and μ as a function of $\varepsilon = E/B$ (here $B = E_{\max} - E_{\min} \approx 1$). Note that the left panel shows the rescaled temperature NT since typical numerical values of T are $\sim 1/N$ due to the finite value of B in our particular model. (We note that the construction of the Lorenz curve is independent of a global scaling factor one could apply to the energy levels.) The figure illustrates that $-\mu \to 0$ $(\mu \to -\infty)$ for $\varepsilon \to 0$ $(\varepsilon \to 1/2)$.

Using (A.3) one can show that $-\mu \approx E/(N-1) \ll E$ for very small energies $0 < E \ll 1/N$ and in this particular case we have $\rho_0 \approx 1$ (strong condensation) and other $\rho_m \sim E/(NE_m) \ll 1/N$ (for $m > 0$). With increasing values of E (or ε) the values of "$-\mu$" increase and more probability is shifted to the other ρ_m values for $m > 0$. At $\varepsilon \approx 1/2$ we have very large values of "$-\mu$" (and of T) such that all $\rho_m \approx 1/N$ are uniformly constant. Further increase of ε enters the regime of negative temperatures (with $\mu > E_{\max}$) with possible condensation at the last oscillator with

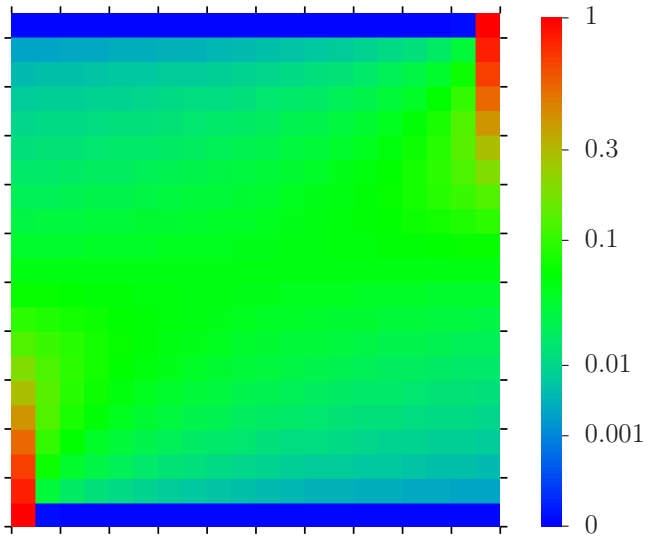

Fig. A.2 Color plot of the coarse-grained thermalized occupation probabilities $\rho_m = T/(E_m - \mu) = (E-\mu)/[N(E_m-\mu)]$ for the RJS model. The x-axis corresponds to the fraction $E_m/B \in [0,1]$ (left to right) and the y-axis to the rescaled energy ε (top to bottom for increasing values). The tics indicate integer multiples of 0.1 for both quantities. The color values shown in the color bar correspond to the value of ρ_m averaged over intervals of size 1/20 (for E_m/B on the x-axis) and computed for 21 values $\varepsilon = i/20$, $i = 0, 1, \ldots, 20$ (for the y-axis; the minimal value $\varepsilon = 0$ has been slightly enhanced and the maximal value $\varepsilon = 1$ has been slightly reduced to have a stable computation of the thermalized μ-value). To increase visibility of small values a non-linear color bar scale has been chosen (e.g. green color corresponds to 1/16).

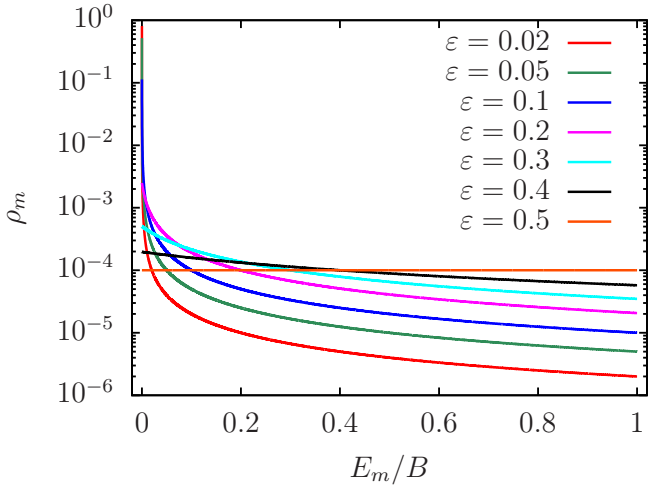

Fig. A.3 Dependence of the thermalized occupation probabilities $\rho_m = T/(E_m - \mu) = (E - \mu)/[N(E_m - \mu)]$ on E_m/B for the RJS model $E_m = m/N$, $N = 10000$ and the same values of $\varepsilon = E/B$ used in Figure I.1 of the main part.

$\rho_{N-1} \gg 1/N$ (in this work we do not insist on the regime of $T < 0$). These features are visible in both figures Figs. A.2 and A.3 showing ρ_m versus E_m/B for different values of ε (as color plot or curves in log-scale). The effect of condensation for small ε with a finite probability $\rho_0 \gg 1/N$ is clearly visible in both figures and qualitatively one could even say that it extends even up to $\varepsilon = 0.2$ with $\rho_0 = 0.002495$ still being larger than $1/N$. However, here also some other values of ρ_m with small m are significantly larger than $1/N$ (as can be seen in A.3 for the first 5% of modes with $\rho_m \geq 3/N$). Also the coarse-grained average value at the first 5% of modes at $\varepsilon = 0.2$ is roughly 0.35 times the maximal coarse-grained value at $\varepsilon \approx 0$ (according to Fig. A.2). This effect corresponds to (modest) condensation on several modes or a given small mode interval.

When constructing the Lorenz curve we have $w = 0$ for $h < \rho_0$ and in the presence of (strong) condensation there is a finite interval of households with no wealth at all. Even for modest condensation over several modes the wealth value is initially very low. This can also be seen in Fig. I.1 where $w(h \leq 0.1) \approx 0$ for $\varepsilon = 0.2$ showing the effect of modest condensation.

Below, we will present a continuous version of the RJS model with the exact limit $N \to \infty$ and some analytic formulas for the key quantities.

A.2 Additional data

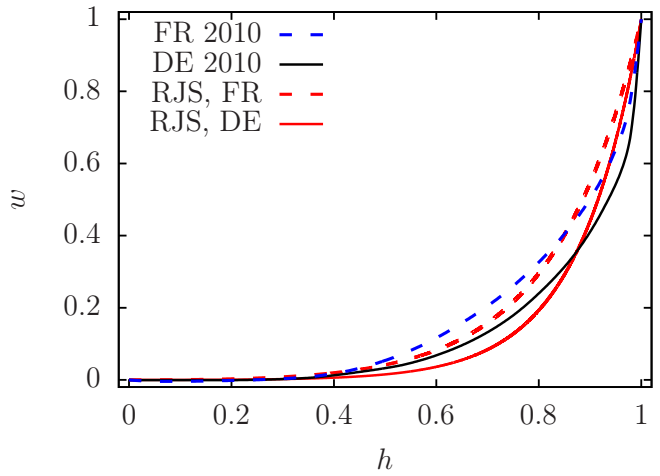

Fig. A.4 Comparison of the Lorenz curves for DE 2010 (black) and FR 2010 (blue dashed) with those of the RJS model (red curves; $N = 10000$). The data of DE and FR were extracted from Ref. [56]. As in Fig. I.3 the Gini coefficients $G = 0.758$ (DE) and $G = 0.679$ (FR) were used to determine the ε values of the RJS model as $\varepsilon = 0.1220$ (DE) and $\varepsilon = 0.1659$ (FR) to match the Gini coefficients of the reference data.

In this section, we present additional data. First Fig. A.4 shows the Lorenz curves from Germany and France and the corresponding curves of RJS model (with matching

Gini coefficients). These data were extracted from Ref. [56] with best possible precision and correspond to the period of 2010. The agreement with the RJS is comparable (not perfect but still rather close) as with the cases of US and World in Fig. I.3. The Gini coefficients of Germany ($G = 0.758$) and France ($G = 0.679$) are both intermediate between UK ($G \approx 0.62$) and US/World ($G \approx 0.85/0.84$).

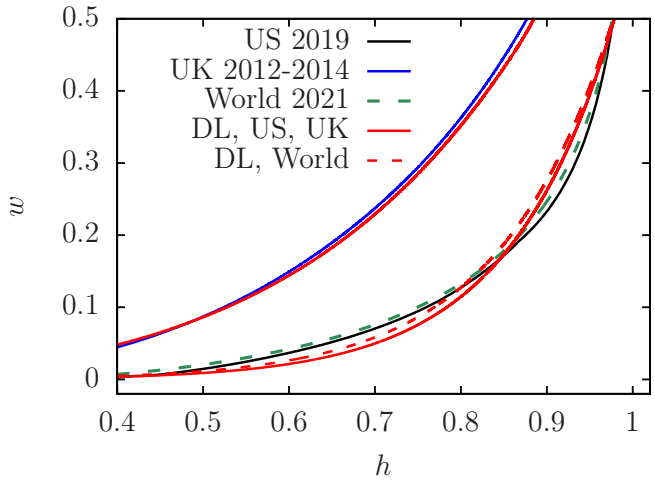

Fig. A.5 As panel (b) of Fig. I.4 but with a zoomed representation for $h \in [0.4, 1]$ and $w \in [0, 0.5]$ to increase the visibility between the close curves for US 2019 and World 2021.

The next Figure A.5 shows a zoomed representation of panel (b) of Figure I.4 for $h \in [0.4, 1]$ and $w \in [0, 0.5]$ to increase the visibility between the close curves for US 2019 and World 2021 and to also to enhance the small differences with respect to the DL model (red lines).

Furthermore, Fig. A.6 presents results for the EQI model with $E_0 > 0$, $E_m = E_0 + m/N$ and $\varepsilon = (E - E_0)/(E_{N-1} - E_0) \approx E - E_0$. In this case, the finite value $E_0 > 0$ induces an initial finite slope $E_0/E = E_0/(E_0 + \varepsilon)$ in the Lorenz curve. We have verified that for the four cases shown in Fig. A.6 this formula indeed represents the initial slope (see figure caption for the values). In this model, even the poorest households own a significant fraction of the wealth which is given by this slope. Here the range of possible Gini coefficients is quite limited with maximum values of $G_{\max} \approx 0.1$ or 0.4 for $E_0 = 1$ or $E_0 = 0.1$ respectively. Due this reason it is not possible to match the data of US, UK, World etc. (with much larger Gini coefficients) to this model (for the cases shown in Figs. I.6, A.6).

Finally, Fig. A.7 shows several color plots in the same style as Fig. I.2, i.e. the color value (visible in the color bar) shows w of the Lorenz curve as a function of h (x-axis) and ε (y-axis). The 2nd panel for the RMT model is rather similar to Fig. I.2 for the RJS model, with a slight tendency for smaller G values for $\varepsilon > 0.2$ (at given ε, see also Fig. I.5). The first panel for the DL model with $a = 16$ has a stronger condensation effect (i.e. more poor or poorer households) at $\varepsilon \approx 0.08$ as compared

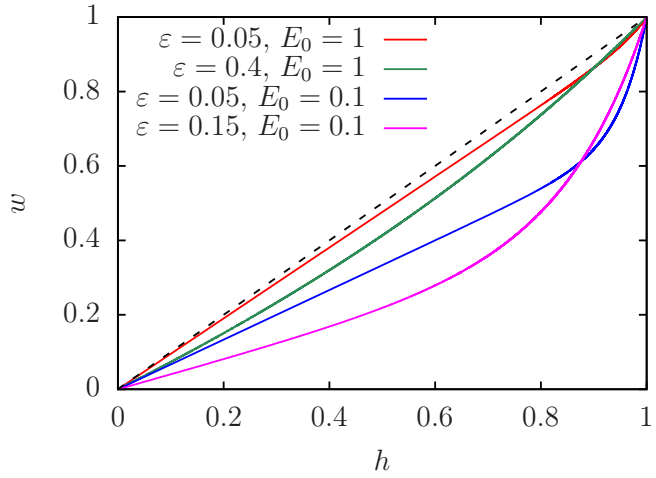

Fig. A.6 Lorenz curves of the thermalized EQI model ($N = 10000$) with the two offset values $E_0 = 0.1$ and $E_0 = 1$ and for each case for two values of the rescaled energy $\varepsilon = (E - E_0)/(E_{N-1} - E_0)$. Note that for $E_0 = 1 \Rightarrow E_{N-1} \approx 2E_0$ and for $E_0 = 0.1 \Rightarrow E_{N-1} \approx 11E_0$. The dashed line corresponds to the line of perfect equipartition $w = h$. The Gini coefficients G for all curves are $G = 0.4239, 0.3000, 0.1162, 0.04286$ (bottom to top). These curves show a finite initial slope with value $E_0/(\varepsilon + E_0) = 0.4, 0.6667, 0.7143, 0.9524$ (bottom to top).

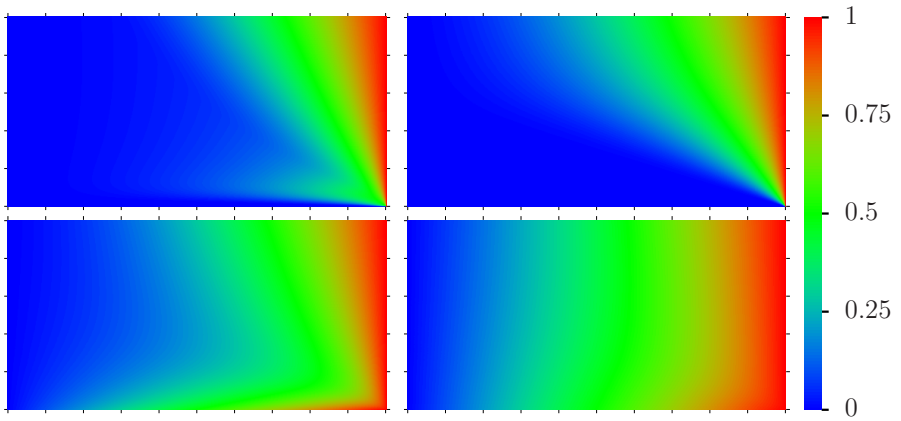

Fig. A.7 Color plot of Lorenz curves for different models in the same style of Figure I.2. The panels correspond to the DL model with parameter $a = 16$ (top left), to the shifted RMT semi-circle spectrum (top right), to the EQI model with given offset $E_0 = 0.1$ (bottom left) and $E_0 = 1$ (bottom right). For the EQI model the rescaled energy $\varepsilon \in [0, 0.5]$ for the vertical axis is given by $\varepsilon = (E - E_0)/(E_{N-1} - E_0)$ (same expression for the other models but with $E_0 = 0$). All cases correspond to $N = 10000$ levels except for RMT with $N = 1000$.

to $\varepsilon \approx 0.03$. Both bottom panels correspond to the EQI model with $E_0 > 0$ (here $\varepsilon = (E - E_0)/(E_{N-1} - E_0)$) with reduced Gini coefficients and where poor people own a significant fraction of the wealth, even at small values of ε.

A.3 Analytical results for RJS model

For the RJS model with finite ε it is possible to obtain explicit formulas in the limit $N \to \infty$ by replacing the sums over m with integrals over an energy variable $\tilde{E} = m/N \in [0, 1]$. In the following, we also use $\varepsilon = E$ (since $E_0 = 0$ and $B = (N-1)/N \to 1$ for $N \to \infty$). In the limit $N \to \infty$ the implicit equation (A.3) becomes:

$$1 = (\varepsilon - \mu) \int_0^1 \frac{1}{\tilde{E} - \mu} \, d\tilde{E} = (\varepsilon - \mu) \ln \left(\frac{1 - \mu}{-\mu} \right) \tag{A.4}$$

which can be rewritten in the following form:

$$\mu = -(1 - \mu) e^{-1/(\varepsilon - \mu)} \ . \tag{A.5}$$

Both equations determine μ as a function of $\varepsilon \in]0, 1[$. In the limit of small ε one can simply iterate Eq. (A.5) by inserting $\mu_0 = 0$ in the RHS which gives $\mu_1 = -e^{-1/\varepsilon}$ on the LHS which can be inserted in the RHS to obtain a better value μ_2 etc. This procedure converges nicely for small ε and for other values of ε one can use standard techniques to solve these equations numerically and efficiently. For $\varepsilon \ll 1$, the first approximation $(-\mu) \approx e^{-1/\varepsilon} \ll \varepsilon$ is already very good.

To understand the limit of $|\mu| \gg 1$ it is more useful to consider ε as a function of μ which is determined by (A.4). Expanding the logarithm in (A.4) up to 3rd order in $1/\mu$ one finds that

$$\varepsilon \approx \frac{1}{2} \left(1 + \frac{1}{6\mu} \right) \to \frac{1}{2} \tag{A.6}$$

for $|\mu| \to \infty$ which is expected from the curve of μ in Fig. A.1. The $1/\mu$ correction in (A.6) will be useful below.

As explained in the main part of this work, to compute the Lorenz curve we have to compute a partial sum over ρ_m to obtain the household fraction h and over $(E_m/\varepsilon)\rho_m$ to obtain the wealth variable. Now, we replace these partial sums also by integrals up to some arbitrary value $s \in [0, 1]$ which provides functions $h(s)$ and $w(s)$ allowing to determine the Lorenz curve $w(h)$. These partial integrals are:

$$h(s) = (\varepsilon - \mu) \int_0^s \frac{1}{\tilde{E} - \mu} \, d\tilde{E} = (\varepsilon - \mu) \ln \left(\frac{s - \mu}{-\mu} \right) \tag{A.7}$$

$$\Rightarrow \quad s(h) = (-\mu) \left(e^{h/(\varepsilon - \mu)} - 1 \right) \tag{A.8}$$

and

$$w(s) = \frac{\varepsilon-\mu}{\varepsilon}\int_0^s \frac{\tilde{E}}{\tilde{E}-\mu}\,d\tilde{E}$$
$$= \frac{1}{\varepsilon}\left[(\varepsilon-\mu)s + \mu(\varepsilon-\mu)\ln\left(\frac{s-\mu}{-\mu}\right)\right] . \tag{A.9}$$

Inserting (A.7) and (A.8) in (A.9) we obtain the following analytical expressions for the Lorenz curve:

$$w(h) = \frac{-\mu}{\varepsilon}\left((\varepsilon-\mu)\left(e^{h/(\varepsilon-\mu)}-1\right)-h\right) \tag{A.10}$$
$$= \frac{1-\mu}{\varepsilon}\,e^{-1/(\varepsilon-\mu)}\left((\varepsilon-\mu)\left(e^{h/(\varepsilon-\mu)}-1\right)-h\right) . \tag{A.11}$$

Here (A.11) has been obtained by replacing the global factor μ with (A.5) which gives a more convenient expression. Using (A.5), one can verify that (A.10) (and therefore also (A.11)) satisfy the conditions $w(0) = 0$ and $w(1) = 1$.

The expression (A.11) allows to take the limit $\varepsilon \ll 1$ with $\mu \approx -e^{-1/\varepsilon} \ll \varepsilon$ such that for $\varepsilon \ll 1$ we have the simplified Lorenz curve (replacing $\mu = 0$ in (A.11)):

$$w(h) \approx e^{-1/\varepsilon}\left(e^{h/\varepsilon} - 1 - \frac{h}{\varepsilon}\right) \approx e^{(h-1)/\varepsilon} . \tag{A.12}$$

Here both expression are equivalent approximations for small ε with $e^{-1/\varepsilon} \ll 1$. The first (second) expression does not exactly verify the condition for $w(1)$ (or $w(0)$). The second expression is very simple and numerically quite sufficient for $\varepsilon \leq 0.2$.

We have verified that both expressions (A.10) and (A.11) coincide with the numerical data shown in Fig. I.1 up to graphical precision with an error below 10^{-4} and for all values of ε used in Fig. I.1. The approximate formulas (A.12) are valid for $\varepsilon \leq 2$ with an error $\sim 10^{-2}$ for $\varepsilon = 0.2$ (and smaller errors for smaller values of ε). This can be seen in Fig. A.8 comparing the data for $\varepsilon = 0.1, 0.2, 0.3$ between the analytic expressions and the data for $N = 10000$. Even for $\varepsilon = 0.3$ only a modest deviation of the approximate curve is visible while here and in all other cases the more precise expression (A.11) matches the numerical data very closely.

Using the analytical expressions for $w(h)$ one can compute several other quantities. For example it is interesting to consider the 2nd order expansion in h for $|h/(\varepsilon-\mu)| \ll 1$ which gives:

$$w(h) = \frac{(-\mu)}{2\varepsilon(\varepsilon-\mu)}\,h^2 . \tag{A.13}$$

We know that the limit $|\mu| \to \infty$ corresponds to $\varepsilon \to 1/2$ and in this case (A.13) is valid for all $h \in [0, 1]$. This gives the very simple formula $w = h^2$ (which is also obvious from the fact that $\rho_m = 1/N = \text{const.}$ for $|\mu| \to \infty$ and the way the Lorenz curve is constructed from ρ_m).

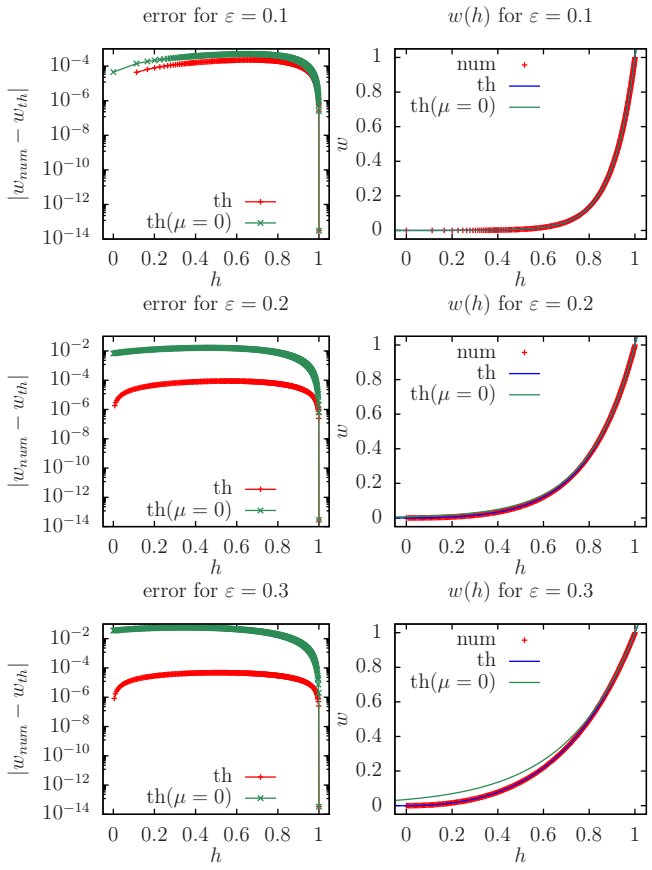

Fig. A.8 Comparison of Lorenz curves of wealth fraction w versus household fraction h for the analytical model with the numerical data of the RJS model for finite $N = 10000$ and for three key values of the rescaled energy $\varepsilon = 0.1, 0.2, 0.3$ (top to bottom). Left panels shows the difference between the analytical model and numerical data and right panels show directly the curves w versus h for the numerical data (red lines and plus symbols) and the analytical model. Blue lines/data points correspond to the formula (A.11) valid for all values of ε and using the appropriate value of the chemical potential μ determined by the implicit equation (A.4). Green lines/data points correspond to the (second) approximate formula (A.12) valid for small $\varepsilon \leq 0.2$. The discrete points of data in the top right panel for $\varepsilon = 0.1$ at values close to $w = 0$ indicate finite values for $\rho_0 = 0.1129$, $\rho_0 + \rho_1 = 0.1660$, etc. which are due to RJ condensation.

It is also possible to compute the Gini coefficient:

$$G = 1 - 2\int_0^1 w(h)\,dh$$
$$= 1 + \frac{2\mu}{\varepsilon}\left[(\varepsilon-\mu)^2(e^{1/(\varepsilon-\mu)}-1) - (\varepsilon-\mu) - \frac{1}{2}\right] \tag{A.14}$$
$$= 1 - \frac{\mu}{\varepsilon} - 2(\varepsilon-\mu)\ . \tag{A.15}$$

Here the second simpler expression (A.15) has been obtained by replacing the exponential term in (A.14) using the implicit equation of μ. The limit $\varepsilon \ll 1$ with $\mu \approx -e^{-1/\varepsilon}$ gives $G \approx 1-2\varepsilon$ which matches well the values of G given in the caption of Fig. I.1 for $\varepsilon \leq 0.1$ (rather close value for $\varepsilon = 0.2$). The other values are matched exactly by the more precise expression (A.15). Furthermore, inserting the expression (A.6) for large $|\mu|$ in (A.15) one finds (confirms) that $G = 1/3$ for $\varepsilon = 1/2$ (here it is necessary to keep the $1/\mu$ correction in (A.6) to obtain the correct result for G).

Using the analytical expression (A.11) for $w(h)$, it is also straightforward to compute (with simple numerics) the inverse function $h(w)$. Using this and the analytical expression (A.15) for the Gini coefficient, we have also recomputed the curves for $G(\varepsilon)$, $h(2\%)$, $1-h(25\%)$ (both as a function of ε) and verified that the analytical curves coincide with the numerical curves shown in Fig. I.5 and Fig. I.6 (for the RJS model at $N = 10000$) up to graphical precision (typical error $\sim 10^{-4}$).

One might be concerned that the integral approximation is not very good for small μ (close to the singularity of the first term in (A.3)) and some finite but large value of N such as $N = 10000$. This is true but the integral provides a modified logarithmic singularity which allows also to mimic correctly the condensation effect with correct probabilities. Therefore even though the values of μ are modified for $\varepsilon \ll 1$ (but still $0 < -\mu \ll \varepsilon \ll 1$ for both models !) the resulting probabilities (e.g. integrals or sums of ρ_m over some interval in $\tilde{E} = m/N$) are the same. The values of μ obtained by the continuous analytical model match very well the curve shown in Fig. A.1 but of course this figure does not allow to verify if $\mu \approx -e^{-1/\varepsilon}$ (continuous model) or $\mu \approx -\varepsilon/(N-1)$ (for the finite N model with discrete sums) which are both close to zero in the figure. In any case, we find that the analytical expressions given here (if μ is properly evaluated by its implicit equation (A.4) and if properly evaluated by avoiding numerical instabilities of some formulas in some special cases) match the numerical data with an error that scales with $1/N$.

Without going into details, we mention that we have also considered a more refined version of the continuous model using a finite value of N and keeping the first singular term separate from the integral (which starts at $s = 1/N$ and not $S = 0$). In this case, we obtain a modified implicit equation of μ which results in values of μ closer to the model of finite N but the resulting physical quantities ($w(h)$ curves, Gini coefficients etc.) are (numerically with an error $< 10^{-4}$) the same as both the numerical data and the simple model. The resulting analytical expressions of the refined model are slightly modified (essentially replacing h by $h - \rho_0$ for $h \geq \rho_0$ in the formula of the Lorenz curve and using $w(h) = 0$ for $h < \rho_0$ where ρ_0 may now have a finite value).

Note that the initial interval $h \in [0, \rho_0[$ with exactly $w(h) = 0$ for the refined and also the discrete model translates to exponentially small values $w(h) \approx h^2\, e^{-1/\varepsilon}/(2\varepsilon)$ for the simple analytical model (replacing $\mu \approx -e^{-1/\varepsilon}$ in (A.13)).

A.4 Data for companies of stock exchange at New York, London, Hong Kong

We present here the Lorenz curves for the capitalization of companies at stock exchanges of New York, London, Hong Kong. They are obtained respectively from Refs. [57–59].

First, we present in Fig. A.9 the Lorenz curve for the data of 504 S&P500 companies of the New York Stock Exchange (NYSE) of June 16, 2025 (see Ref. [57]). This Fig. A.9 shows the direct comparison of the Lorenz curve of NYSE and the corresponding RJ thermal distribution of the RJS model (at same Gini value). Here, we use the standard value $N = 10000$ for the RJS curve but using a reduced value $N = 504$ (as the number of companies) gives the same RJS curve within graphical precision. The quality of agreement with the RJS model is comparable to the cases of US or World in Fig. I.3. We also note the characteristic values: $h = 0.191$ at wealth $w = 0.02$; $w = 0.092$ at $h = 0.5$; the wealth of top 10 percent of h companies is $1 - w(0.9) = 0.602$ and the wealth of top 1 percent of companies is $1 - w(0.99) = 0.267$. Thus we see that there is a small fraction of oligarchic companies that monopolize a big fraction of total wealth. The fraction of poor companies, corresponding to the RJ condensate, is smaller than the fraction of poor households in the US or World cases. We attribute this to the fact that these 504 companies of S&P500 represent only about 80 percent of the total capitalization of US companies.

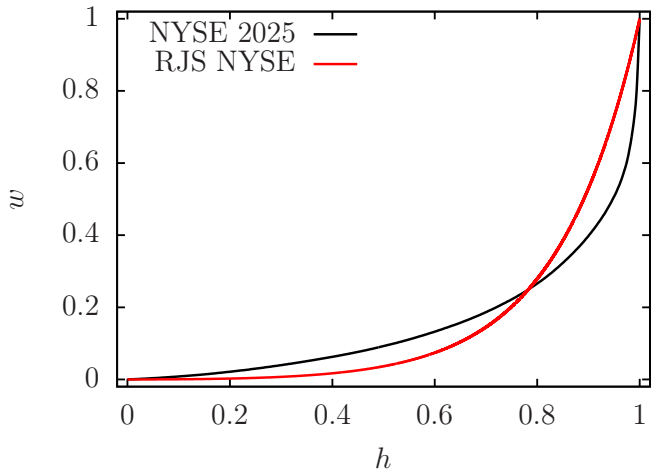

Fig. A.9 Comparison of the Lorenz curve for the S&P500 companies of NYSE 2025 (black; data from Ref. [57]) with the corresponding curve for the RJS model (red curve; $N = 10000$) at same Gini coefficient $G = 0.692$ obtained for $\varepsilon = 0.1582$.

Fig. A.10, compares the Lorenz curve for the London stock exchange (2024; data from Ref. [58]) with the RJS model. Here, the Gini coefficient $G = 0.9126$ is higher than for the US and World cases and the corresponding value $\varepsilon \approx 0.044$ for the RJS model is quite small. Due to the high value of G the first probability $\rho_0 = 0.6545$ is very high indicating a strong RJ condensation with exactly $w = 0$ for $h \in [0, \rho_0[$ in the RJS model. The chosen value $N = 1637$ is identical to the number of considered companies but the RJS curve for $N = 10000$ is identical on graphical precision (with a slightly modified value for ε).

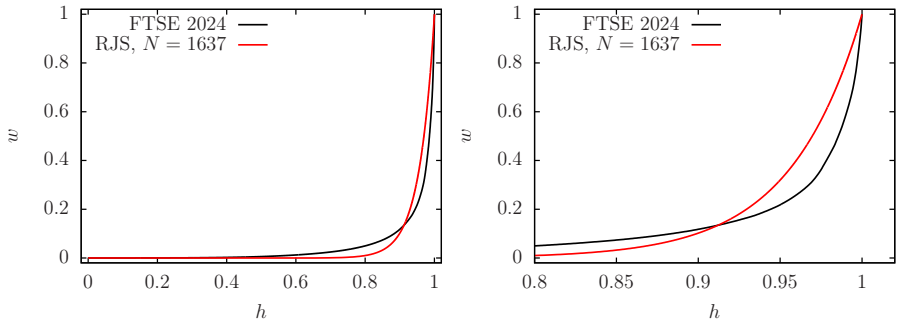

Fig. A.10 Comparison of the Lorenz curve for the 1637 companies of the London stock exchange FTSE at 31 December 2024 (black; data from Ref. [58]) with the corresponding curve for the RJS model (red curve; $N = 1637$) at same Gini coefficient $G = 0.9126$ obtained for $\varepsilon = 0.04387$. The left (right) panel shows the full range $h \in [0, 1]$ (zoomed range $h \in [0.8, 1]$).

Fig. A.11, compares the Lorenz curve for the Hong Kong stock exchange (2025; data from Ref. [59]) with the RJS model. Here, the Gini coefficient $G = 0.9471$ is even higher than for the London stock exchange and the corresponding value $\varepsilon \approx 0.027$ for the RJS model is even smaller. Due to the very high value of G the first probability $\rho_0 = 0.7768$ is even higher (than ρ_0 for the London stock exchange) indicating a strong RJ condensation with exactly $w = 0$ for the larger interval $h \in [0, \rho_0[$ in the RJS model. The chosen value $N = 2683$ is identical to the number of considered companies but the RJS curve for $N = 10000$ is identical on graphical precision (with a slightly modified value for ε).

Fig. A.12, compares the Lorenz curve for the 30 Dow Jones companies (2025; data from Ref. [57]) with the RJS model. Here, the Gini coefficient $G = 0.3096$ is very low and the corresponding value $\varepsilon \approx 0.55$ for the RJS model is very high being in the region for $T < 0$ with large $|T|$. The value of G is even smaller then $G = 1/3$ for the curve $w = h^2$ corresponding to the RJS model with $\varepsilon = 0.5$ and $|T| \to \infty$. The chosen value $N = 30$ is identical to the number of considered companies but despite the modest value of N the RJS curve for $N = 10000$ is identical on graphical precision (with a slightly modified value for ε). We mention, that a comparison with the EQI model for a modest value of E_0 to fit approximately the finite initial slope in the data provides the energy value $\varepsilon \approx 0.48 < 0.5$ corresponding to the regime of $T > 0$ but still with large $|T|$. We note that this case is very special since these 30 companies are

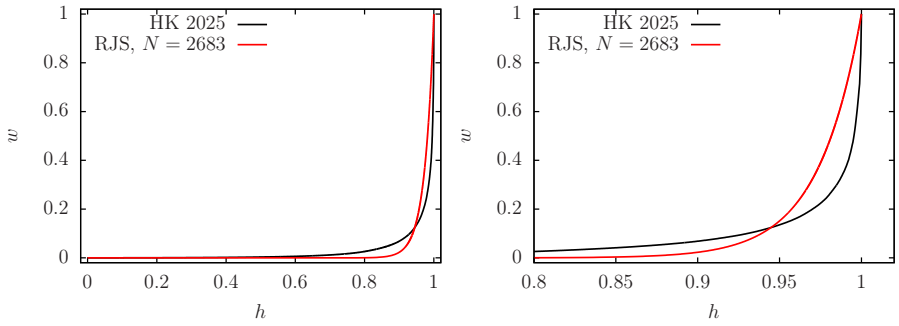

Fig. A.11 Comparison of the Lorenz curve for the 2683 companies of the Hong Kong stock exchange at 19 June 2025 (black; data from Ref. [59]) with the corresponding curve for the RJS model (red curve; $N = 2683$) at same Gini coefficient $G = 0.9471$ obtained for $\varepsilon = 0.02651$. The left (right) panel shows the full range $h \in [0, 1]$ (zoomed range $h \in [0.8, 1]$).

certainly not isolated and they constitute a subset of the 504 companies of S&P500 (which are not perfectly isolated as well).

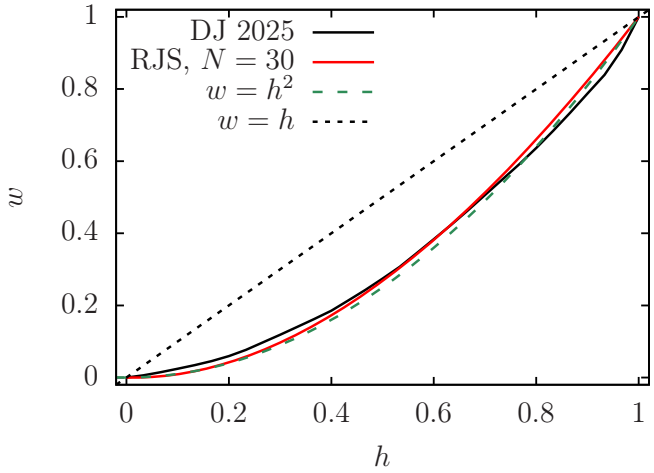

Fig. A.12 Comparison of the Lorenz curve for the 30 Dow Jones companies of NYSE 2025 (black; data from the site of Ref. [33] taken at June 18, 2025) with the corresponding curve for the RJS model (red curve; $N = 30$) at same Gini coefficient $G = 0.3096$ obtained for $\varepsilon = 0.5528$. The dashed green (black) line represents the curve for $w = h^2$ ($w = h$) for the RJS model at $\varepsilon = 0.5, T \to \infty$ (perfect equipartition).

A.5 Spectral reconstruction procedure

Let us briefly remind the construction of a Lorenz curve, already given in the main part, from a given model spectrum E_m with appropriate values of μ, E and T such that the two conditions (A.1) are verified. For this a set of points (h_m, w_m) is determined with

$h_0 = w_0 = 0$, $h_{m+1} = h_m + \rho_m$ and $w_{m+1} = w_m + (E_m/E)\,\rho_m$ for $m = 0, \ldots, N-1$ and where

$$\rho_m = \frac{E - \mu}{N(E_m - \mu_m)} \tag{A.16}$$

(see also (A.2)). Then the conditions (A.1) assure that $h_N = w_N = 1$ and the points (h_m, w_m) provide for $0 \leq m \leq N$ the associated Lorenz curve with both $h_m, w_m \in [0, 1]$.

The question arises if it is possible to invert this construction, i.e. to determine ("reconstruct") for a given Lorenz curve $w(h)$ a certain effective spectrum E_m with appropriate values of μ and E such that its related Lorenz curve is very close to the Lorenz curve of real data with best possible precision (depending on the choice of N).

This is indeed possible and to define an explicit reconstruction procedure let us assume we have some smooth Lorenz curve $w(h)$ with derivatives $w'(h) \geq 0$ and $w''(h) > 0$ for all $h \in [0, 1]$. In particular, we assume that we can compute numerically with high precision and in a reliable way the derivative $w'(h)$ which satisfies $w'(h_1) > w'(h_2)$ for all points with $h_1 > h_2$ (this assumption may be problematic in practice; see below). For simplicity, we also assume that $w'(0) = 0$ and we want to construct spectra with $E_0 = 0$ which is the most relevant case for the typical examples (it is not difficult to modify the method for the more general case $w'(0) \neq 0$ with $E_0 \neq 0$). Furthermore, we choose $E = 1$ to fix the global energy scale. Then the value of $E_m/E = E_m$ is (very close to) the derivative $w'(h_m)$ at the corresponding value of h_m. However, initially we do not know the value of h_m for a given index m (or the index m value as a function of h_m).

We choose some initial value for μ (close to zero), start with $m = N - 1$ and want first to determine $E_m = E_{N-1}$. Here we know the last value $h_{m+1} = 1$ at $m = N - 1$. Therefore, we can at least approximately compute $E_m = w'(h_{m+1})$ and then the associated value of ρ_m using (A.16). This pair (E_m, ρ_m) is yet not very precise since the derivative is taken at the right boundary of the interval $[h_m, h_{m+1}]$ and we can refine its value by recomputing $E_m = w'(h_{m+1} - \rho_m/2)$ using a small shift with the first approximate value of ρ_m (which will then be updated with the more precise value of E_m using (A.16)). In principle, one could iterate this refinement step until there is convergence of (E_m, ρ_m). However, in our experience the method works best with precisely one refinement step (to ensure later convergence for a good value of μ). Once ρ_m is known, we obtain $h_m = h_{m+1} - \rho_m$. Then we decrease m by 1 and repeat this procedure to compute the next values of E_m, ρ_m and h_m at $m = N - 2$. This provides a recursion for $m = N - 1, N - 2, \ldots, 1, 0$ and three sequences for E_m, ρ_m and h_m with decreasing m.

For the last value E_0 at $m = 0$ we do not use the derivative but we simply fix it by $E_0 = 0$. Typically, in this regime the derivative is already very small. Ideally, the last value $h_0(\mu)$ should be $h_0(\mu) = 0$ but this is only true for a specific value of μ which has to be found iteratively, e.g. to be determined numerically as the zero of the function $h_0(\mu)$ by some standard method (which is actually quite tricky for bad quality data with problematic convergence) and where this function is computed by a full reconstruction loop $m = N - 1, \ldots, 0$ for each value of μ as described above.

Instead of searching numerically the zero of the function $h_0(\mu)$, one can also use another more practical method to determine the correct value of μ. For this, one can at the last step $m = 0$ manually fix the last density value and compute from (A.16) a new modified value $\tilde{\mu}$ such that the condition $\rho_0(\tilde{\mu}) = h_1$ holds exactly and therefore $h_0 = 0$ is perfectly verified. The modified value $\tilde{\mu}$ can be reinjected in the procedure from the start resulting in a fixed-point iteration for μ which typically converges quite well and allows also to use the exact initial value $\mu = 0$ at the first iteration (which is not a problem since this value is not used in the last step at $m = 0$ with $E_0 = 0$). For this method the convergence is typically a bit slower, but more reliable, as compared to the secant method applied to $h_0(\mu)$ but the latter fails to converge in cases of bad quality data which influence the computation of $w'(h)$. In such a situation the fixed point iteration does not always provide a convergence with high precision as well but still the μ values stabilize in some small interval (with relative fluctuations $\sim 10^{-3}$ etc.) and any value in this interval can be used to have a nice reconstructed spectrum.

Once the procedure is finished, we can use the obtained spectrum E_m to recompute a new appropriate value of μ and the densities ρ_m in the usual way by numerically solving (A.3) with the value $E = 1$. In case of good convergence of the procedure this simply confirms the already obtained values of μ and ρ_m but in case of a problematic convergence, this provide a final refinement of μ and ρ_m which will match precisely the spectrum E_m with $E = 1$ according to (A.1) and (A.2). Using these refined densities, we can finally recompute the Lorenz curve associated to this spectrum in the usual way. This curve matches typically, also in the case of not perfect convergence, very well the original data with numerical errors below 10^{-3} (or less).

The choice of the parameter N for the size of the reconstructed spectrum is not very important, except it needs to be sufficiently large, e.g. $N = 1000$. The reconstructed spectrum E_m provides, as a function of the rescaled level number $x = m/N$, essentially the same curves for different (sufficiently large) values of N provided that the same (reliable) numerical implementation for the derivative function $w'(h)$ is used.

The method depends in a very sensitive way on the quality of the numerical implementation of $w'(h)$, quality of input data and chosen interpolation procedure and this part is actually rather tricky. Usual linear interpolation for the initial data for the Lorenz curve $w(h)$ provides a piecewise constant derivative $w'(h)$ which works reasonably well in the above procedure concerning μ-convergence and good matching of the initial Lorenz curve.

If the raw data is of good quality, i.e. with support points that lie very accurately on a smooth function, one can also use a combination of rational interpolation (for the region where $w'(h) > 1$) and polynomial interpolation (for the region with $w'(h) < 1$) and in both cases with a small number of support points between 3 and 6 which are closest to the value of h for which we want to compute $w'(h)$. In both interpolation approaches, one can work out efficient formulas to exactly evaluate the derivative of the interpolation function. However, if the data is of bad quality this procedure may be problematic for μ-convergence and also violate the property that $w'(h_1) < w'(h_2)$ for $h_1 < h_2$ which is crucial to obtain a correctly ordered spectrum (with $E_{m_1} \leq E_{m_2}$ for $m_1 < m_2$). In such a case, it may be necessary to clean the data by coarse-graining them (keeping only 15-20 significant data points) and then recompute a new data

set with 500 or 1000 points using high quality interpolation (also rational/polynomial interpolation with 4-5 support points from the reduced set). In particular for the data of UK 2012-2014 from Ref. [31] with a lot of data points but with limited precision this was necessary.

In order, to keep things simple and reliable, we opted for a compromise between rational/polynomial interpolation and a piecewise constant derivative. Without going into too much details, we mention that we computed first discrete derivatives (from good quality data) and applied linear interpolation to obtain a piecewise linear numerical implementation of $w'(h)$ which respects that $w'(h_1) < w'(h_2)$ for $h_1 < h_2$ and is still a continuous function. In this approach the support points for h are now in the center of two former supports points (for which the discrete derivative was taken) and also a slight renormalization was applied to assure that the interpolated piecewise linear function satisfies numerically $\int_0^1 w'(h)dh = 1$, a property which is very important for the reconstruction procedure.

Using this particular implementation of $w'(h)$, we have applied the above reconstruction procedure to all available data sets. Typically, the obtained reconstructed spectra initially increase slowly (linearly, with a possible quadratic correction) but at some critical value of $x_c = m_c/N \approx$ 0.7-0.9 the increase becomes significantly stronger. Beyond this critical value the precise form of the obtained spectrum depends rather strongly on the chosen interpolation method and the obtained values of E_m are not very reliable. This corresponds to the regime of the Lorenz curve with h close to 1 where both $w'(h)$ and $w''(h)$ may be very large and difficult to obtain with high precision by interpolation.

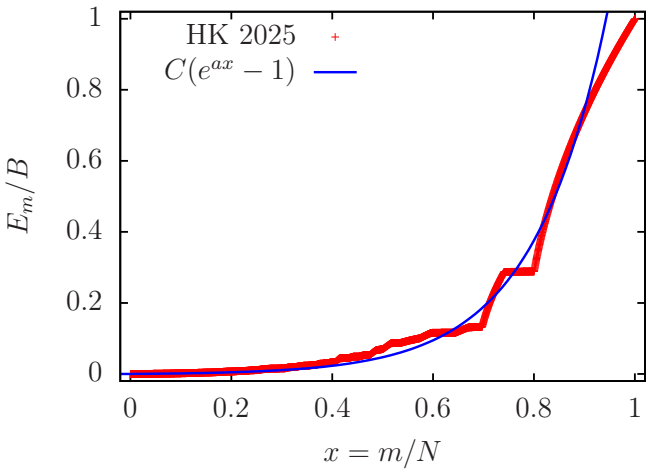

Fig. A.13 Rescaled reconstructed spectrum E_m/B for the data of Hong Kong 2025 (red data points) versus rescaled level number $x = m/N$. The blue curve shows the curve $E_m/B = C\,(e^{ax} - 1)$ with $C = 0.00160 \pm 0.00004$ and $a = 6.83 \pm 0.03$ obtained from a fit in the interval $x \in [0, 0.9]$. The value of $a = 6.83$ is used in Fig. I.11 for the blue curve of the RJE model.

Globally, the fit $E_m = C(e^{a(m/N)} - 1)$ works rather well at least for some reasonable subinterval. For each data set, we perform two fits of this function for the intervals $x \in [0, 0.7]$ and $x \in [0, 0.9]$ that provides two interesting values of a. We inject these two values of the parameter a in the RJE model and determined which a value gives a better agreement for the Lorenz curve (the value of ε is determined as usual by matching the Gini coefficient to be identical between initial Lorenz curve and the model curve). Figs. I.7—I.11 show the resulting RJE curves for 5 of our data sets, already discussed in the previous section, with a very good agreement of the RJE model at the optimal fitted values of a.

In Fig. A.13, we show as illustration one example of an reconstructed spectrum for the data set of the stock market Hong Kong 2025 using the value $N = 2683$ and the piecewise linear derivative for $w'(h)$. The number $N = 2683$ represents the number of companies used in the Hong Kong SE data but the precise choice of this value is not very important and the reconstruction procedure works also nicely for $N = 1000$ or $N = 10000$ for this example. In this case, the shown fit $E_m/B = C\,(e^{ax} - 1)$ works quite well for the larger interval $x \in [0, 0.9]$ and the resulting value of $a = 6.83$ provides a nearly perfect Lorenz curve of the RJE model.

We mention that the bandwidth B of the reconstructed spectrum shown in Fig. A.13 is $B = 566.6$ and it corresponds to the initial choice $E = 1$ to fix the global energy scale such that the rescaled energy of the reconstructed spectrum is $\varepsilon_{rc} = 1/B \approx 0.001765$. The value of $\varepsilon_{\rm RJE}$ for the fitted blue curve is slightly modified due to a modified bandwidth of the latter: $\varepsilon_{\rm RJE} \approx \varepsilon_{rc}/[C\,(e^a - 1)] = 0.001193$ which compares to the value $\varepsilon = 0.0008381$ given in the caption of Fig. I.11 obtained by matching the Gini coefficient. The slightly different value for ε is due to the matching of the Gini coefficient and the fact that the fit is far from perfect. Furthermore, also the data points for $x > 0.9$ are not very reliable.

However, here we do not want to enter deeply in such details and we use this reconstruction procedure more as a tool to determine and justify optimal values of a for the RJE model. Globally this procedure is very sensitive to technical details and parameter choices which give potentially rather different spectra (for x close to 1 beyond a certain critical value x_c) but which all reproduce afterwards matching Lorenz curves to the initial data with good accuracy.

Finally, we note that instead of the above reconstruction procedure it is also possible simply to fit the value of parameter a in the spectrum E_m of Eq.(I.2) in such a way that the Lorenz curve of the RJE model is closet to the real Lorenz curve which is done by minimizing a suitable metric to measure the distance between two curves (parameter ε is fixed as usually to match Gini coefficient). We checked that the obtained a values by minimizing different variants of such metrics are rather close to those obtained from the reconstruction procedure. Thus both approaches allows to obtain very good agreement between the model and real Lorenz curves. The advantage of the reconstruction procedure is related to a more physical understanding of the origins of spectrum E_m.

Appendix B Additional material for Part II

B.1 Netscience network

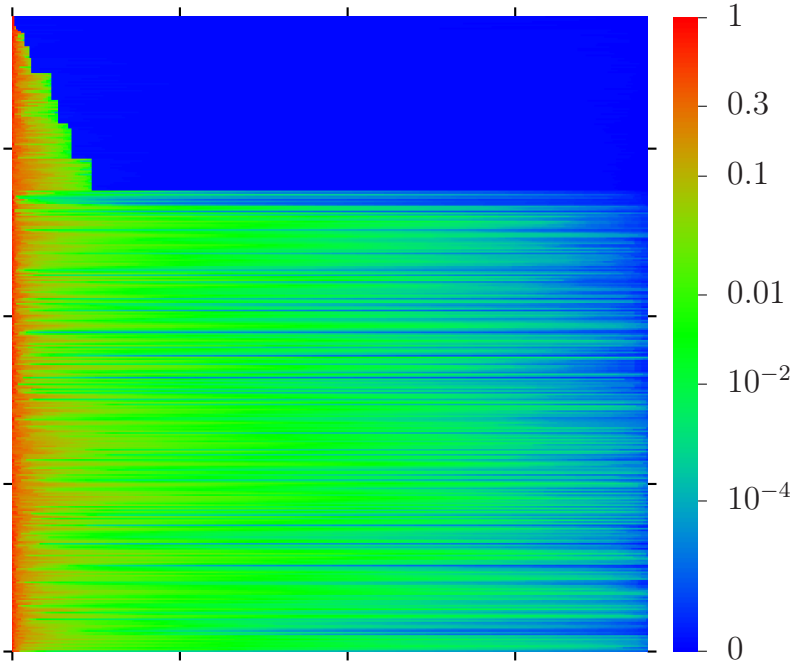

Fig. B.1 Color plot of the eigenvectors $\phi_n^{(m)}$ of the matrix H (size 379×379) for the netscience network at $\kappa = 0$. The values of the color bar correspond to $|\phi_n^{(m)}|^2$ at a certain position ($x = K_m(n), y = L(m)$) in the grid of the color plot. Each row shows a given eigenvector ordered with decreasing values of $|\phi_n^{(m)}|$ in the node index n (from left to right) and therefore the x-axis corresponds to the ordering index $K_m(n) = 1, \ldots, 379$ such that $|\phi_n^{(m)}| > |\phi_{\tilde{n}}^{(m)}|$ for $K_m(n) < K_m(\tilde{n})$ (This index vector is different for each eigenmode m). For each such vector the support length $l(m) =$ number of nodes n with $|\phi_n^{(m)}| > 10^{-12}$ has been computed and the vectors have been ordred with decreasing values of $l(m)$ (bottom to top; ordering for identical $l(m)$ values is arbitrary) and the y-axis corresponds therefore to the ordering index $L(m)$ such $L(m) < L(\tilde{m})$ for $l(m) > l(\tilde{m})$ (lowest $L(m)$ values correspond to the bottom rows). The tics indicate integer multiples of 100 for both index values K_m and L. There are 104 out of 379 eigenvectors with a support length $l(m)$ significantly smaller than $N = 379$ visible at the top 104 rows (other eigenvectors have either $l(m) = N$ or $l(m) \approx N$ due to the limited numerical precison). The eigenvalues E_m of the 104 modes with small $l(m)$ values correspond to nice fractional values (with denominator ≤ 420) and the majority of them correspond to the degenerate plateau values visible in the red curves in the bottom panels of Figure II.1. The scale of the color bar is strongly non-linear to enhance small values of $|\phi_n^{(m)}|^2$.

In Fig. B.1, we show a color plot of the eigenvectors at $\kappa = 0$. Each row represents an eigenvector with components in node space ordered horizontally according to the rank index K_m of this vector (i.e. with decreasing values of $|\phi_n^{(m)}|$ with n for fixed m)

and the eigenvectors themselves are ordered vertically with decreasing values of their support length $l(m)$ (from bottom to top).

The modes with limited support length $l(m) \leq 48$ have energies $E_m = p/q$ with nice rational values (maximal $q = 420$ and other $q \leq 12$). We mention a few examples, such as the mode $E_{25} = -25/12$ with $l(25) = \xi_{\rm IPR} = 2$ localized on the two nodes *Kim, D.* and *Goh* and with values $\phi_n^{(25)} = \pm 1/\sqrt{2}$ for these two nodes. Another example is the pair of two modes $E_{66} = E_{67} = -389/420$ with $l(66) = l(67) = 3$ and $\xi_{\rm IPR} = 2$ for both. These two modes are localized on the three nodes *Rajagopalan*, *Raghavan*, *Tomkins*.

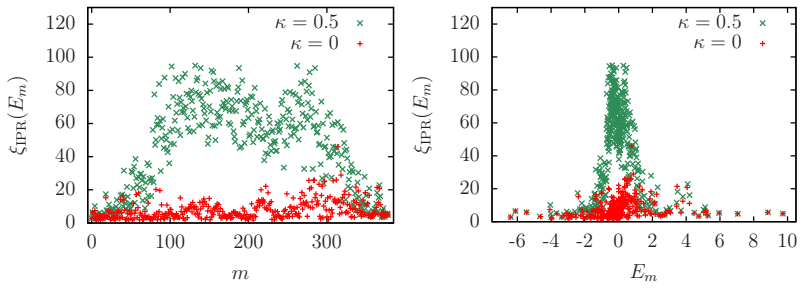

Fig. B.2 $\xi_{\rm IPR}(E_m)$ of eigenvector $\phi^{(m)}$ of H for the case of the netscience network with $\kappa = 0$ and $\kappa = 0.5$ versus index m (energy E_m) in left (right) panel.

Fig. B.2 shows the IPR of eigenvectors for the netscience network at $\kappa = 0$ and $\kappa = 0.5$ versus mode index m and also mode energy E_m. The IPR values at $\kappa = 0.5$ are roughly a factor 10 larger than the values at $\kappa = 0$ and the maximal value of the IPR is 45.98 (94.94) for $\kappa = 0$ ($\kappa = 0.5$). However, the boundary modes have essentially the same (small) IPR values since due to the large energy gaps these modes are in the quantum perturbative regime even at $\kappa = 0.5$ with coupling matrix elements $\sim \kappa/\sqrt{N} = 0.5/\sqrt{379} \approx 1/40$ which is much smaller than the boundary energy gaps.

Fig. B.3 shows the Lyapunov exponent λ_m for selected initial modes m of the netscience network at $\kappa = 0.5$ and $\beta = 0.05, 0.2, 10$. The quantity $\|\Delta\psi(t)\|$ mentionned in the figure caption is the vector norm of the difference $\Delta\psi = \psi_2(t) - \psi_1(t)$ where $\psi_1(t)$ and $\psi_2(t)$ are both solutions of (II.2) with different but close initial conditions at the initial mode $\psi_1(t = 0) \approx \psi_2(t = 0) \approx \phi^{(m)}$. In this case the Lyapunov exponent is defined by $\lambda_m = \lim_{t\to\infty}(\ln \|\Delta\psi(t)\|)/t$ and the data in Fig. B.3 has been extracted by the fit $\ln \|\Delta\psi(t)\| = a + b \ln(t) + \lambda_m\, t$.

The modes at $\beta = 10$ are clearly in the chaotic regime while boundary modes at $\beta = 0.2$ and (most) modes at $\beta = 0.05$ are in the KAM regime with much smaller (numerical) Lyapunov exponent (we expect that for these states Lyapunov exponents become zero in the limit $t \to \infty$).

Fig. B.4 presents coarse-grained color plots in the m-E plane of the theoretical RJ-values $\rho_m = T/(E_m - \mu)$ where T and μ are determined from the implicit equations (II.16). The horizontal x-axis corresponds to $m/N \in]0, 1]$ and the vertical y-axis to the rescaled energy $\varepsilon = (E - E_1)/(E_N - E_1) \in [0, 1]$. The left (right) panel corresponds

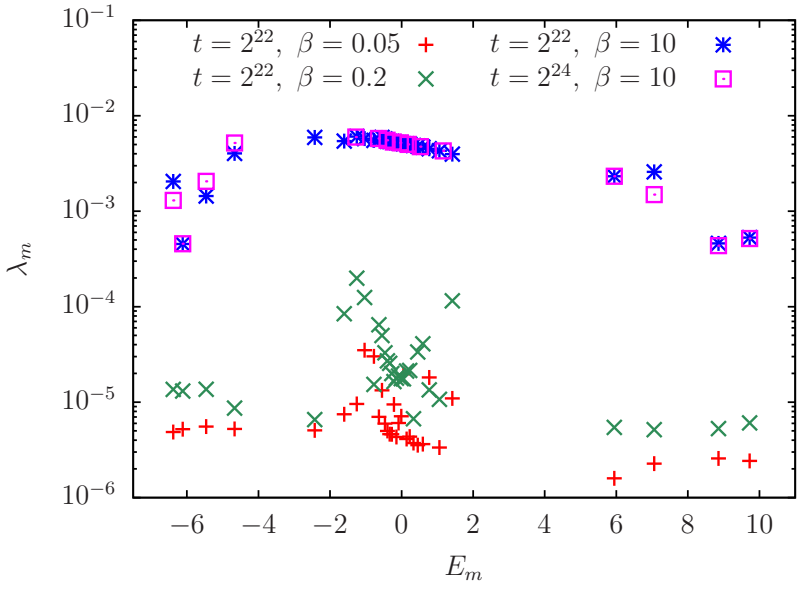

Fig. B.3 Lyapunov exponent λ_m dependence on E_m with m being the index of the initial state for the netscience network with $\kappa = 0.5$ and $N = 379$. λ_m has been determined from the fit $\ln \|\Delta\psi(t)\| = a + b\ln(t) + \lambda_m t$. Shown are data from 4 data sets: with 32 selected modes at $t = 2^{22}$ for $\beta = 0.05$ (red + symbol), $\beta = 0.2$ (green × symbol), $\beta = 10$ (blue ∗ symbol) and also with 16 selected modes at $t = 2^{24}$ for $\beta = 10$ (pink □ symbol) obtained from a different computation.

to the energy spectrum of H at $\kappa = 0.5$ for the netscience network with $N = 379$ (politician network with $N = 5908$). One clearly sees a condensation on the modes with minimal $m \sim 1$ (maximal $m \approx N$) at $E \approx E_1$ ($E \approx E_N$) while for intermediate energies the distribution of ρ_m is more uniform in m.

Fig. B.5 shows the dependence of T and μ on E obtained by solving the implicit equations (II.16) with $\rho_m = T/(E_m - \mu)$. Both curves show the usual behavior with $T > 0$ ($T < 0$) and $\mu < E_1$ ($\mu > E_N$) for $E < 0$ ($E > 0$) with $T \to 0$ for $E \to E_1$ or $E \to E_N$. Furthermore, for $E \to 0$ we have $|T| \to \infty$ and $|\mu| \sim NT \to \infty$ corresponding to uniform $\rho_m \to 1/N$.

It is not very difficult to show that in the limit of large $|\mu|$ the chemical potential is given by the equation

$$\mu \approx E + \frac{\sum_m (E - E_m)^2}{\sum_m (E - E_m)} \ . \tag{B.1}$$

Here the denominator has the same sign as $E - E_c$ where $E_c = (\sum_m E_m)/N = \mathrm{Tr}(H)/N \sim \kappa/N \approx 0$ is the critical energy ("energy center of mass") at which the chemical potential and the temperature switch their sign. Here the trace of H is entirely given by the trace of the GOE perturbation κH_{GOE} since $\mathrm{Tr}(A) = 0$ (the absence of self links implies $A_{nn} = 0$).

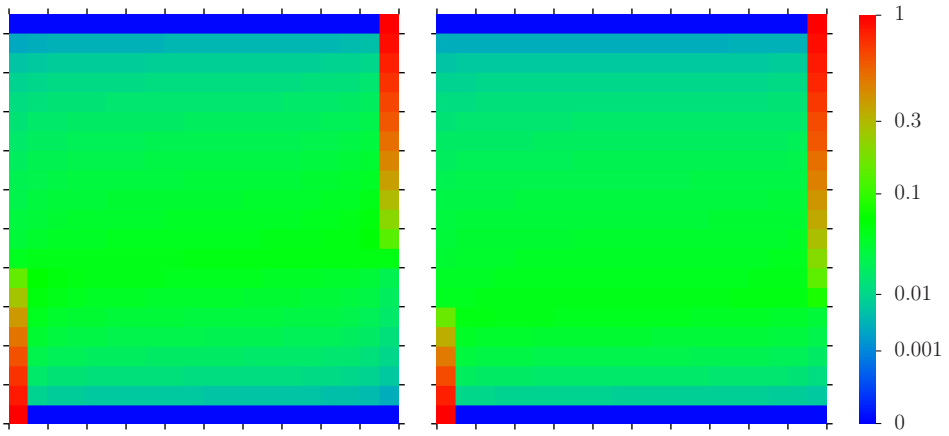

Fig. B.4 Color plot of the coarse-grained thermalized occupation probabilities $\rho_m = T/(E_m - \mu) = (E - \mu)/[N(E_m - \mu)]$ for the netscience network (politician network) at $\kappa = 0.5$ in left (right) panel. The x-axis corresponds to the fraction $m/N \in [0, 1]$ with $m = 1, \ldots, N$ being the index of energies E_m (left to right) and the y-axis corresponds to the rescaled energy $\varepsilon = (E - E_1)/(E_N - E_1)$ (top to bottom for increasing values). The tics indicate integer multiples of 0.1 for both quantities. The color values shown in the color bar correspond to the value of ρ_m averaged over intervals of size 1/20 (for m/N on the x-axis) and computed for 21 values $\varepsilon = i/20$, $i = 0, 1, \ldots, 20$ (for the y-axis; the minimal value $\varepsilon = 0$ has been slightly enhanced and the maximal value $\varepsilon = 1$ has been slightly reduced to have a stable computation of the thermalized μ-value). To increase visibility of small values a non-linear color bar scale has been chosen (e.g. green color corresponds to 1/16).

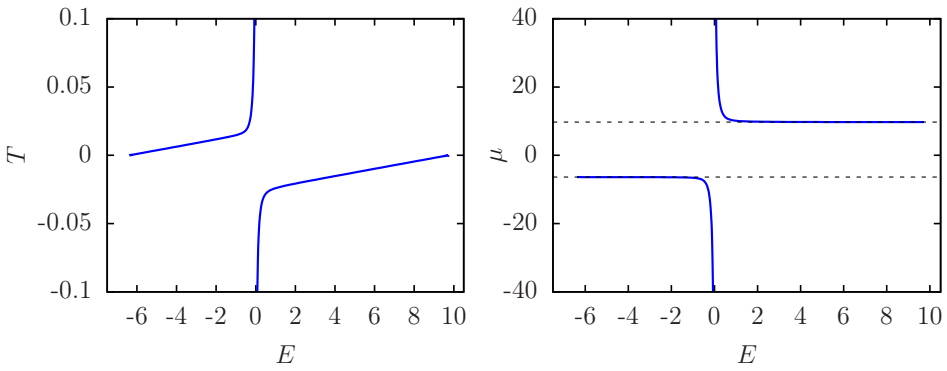

Fig. B.5 The left (right) panel shows the temperature T (the chemical potential μ) versus the energy E for the netscience network at $\kappa = 0.5$. The dashed black lines in the right panel correspond to the values of $E_1 = -6.3829$ and $E_N = 9.7256$ showing that either $\mu < E_1$ (for $T > 0$) or $\mu > E_N$ (for $T < 0$).

Note that Figs. B.4 and B.5, which simply provide a generic illustration of the basic properties of RJ-thermalization, are rather similar to Figs. A.2 and A.1 of Appendix A obtained from a different simple uniform spectrum $E_m = m/N$.

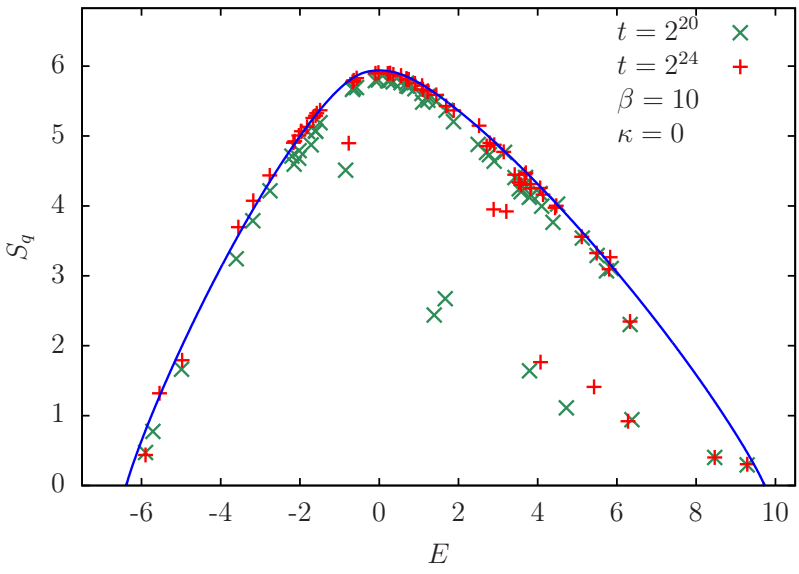

Fig. B.6 Entropy S_q versus energy E for the netscience network with $\kappa = 0$, $\beta = 10$, $N = 379$. Shown are 64 selected modes at $t = 2^{24}$ (red + symbols) and $t = 2^{20}$ (green $\times$ symbols). The blue line shows the energy dependence of the theoretial thermalized entropy. S_q has been computed by Equation (II.17) using ρ_m values obtained as the time average $\rho_m = \langle |C_m(\bar{t})|^2 \rangle$ for $t/2 < \bar{t} \leq t$ (for $t = 2^{24}$ or $t = 2^{20}$ according to the selected data in this figure).

For the case of the netscience network with $\kappa = 0$ and $\beta = 10$, we show in Fig. B.6 the energy dependence of S_q. Here the agreement with the theoretical curve is similar as for the case with $\kappa = 0.5$ but for this longer iteration time scales $t = 2^{24}$ are required.

In Fig. B.7, we present two examples of nicely thermalized states for the netscience network with $\kappa = 0.5$ and $\beta = 4$, Due to the smaller coupling value of β the fluctuations at the shorther time $t = 2^{22}$ are stronger than for similar states at $\beta = 10$.

Fig. B.8 shows some results for the intial condition localized on the nodes of *Barabasi* or *Newman* (top two PageRank nodes for the netscience network). In its first two top panels we see the time dependence of $S_q(t)$ and $S_B(t)/N$ for both cases and the two values $\beta = 4$ and $\beta = 10$. All eight curves saturate to the corresponding theoretical thermalized entropy values which are obtained from the usual value for $E = \langle E \rangle = \sum_m E_m \rho_m(t = 2^{24})$ to determine T and μ and with the numerical final values of $\rho_m(t = 2^{24})$. For the case $\beta = 4$ the onset of thermalization is somewhat delayed in the initial phase with smaller entropy values for $t < 2^{14}$ (in comparison to the case $\beta = 10$). For such states the conserved energy in (II.3) is given by the simple

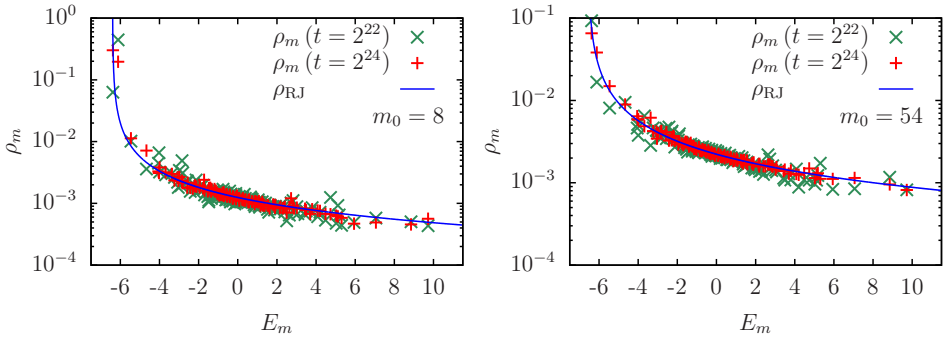

Fig. B.7 As Figure II.3 for the netscience network with $\kappa = 0.5$, $\beta = 4$, $N = 379$ and the two initial modes $m_0 = 8, 54$. The blue curve shows the RJ theoretical curve $\rho_{\rm RJ}(E) = T/(E-\mu)$. The values of T, μ and $\langle E\rangle$ for the 2 initial modes $m_0 = 8, 54$ are $T = 0.008006, 0.01461$, $\mu = -6.4, -6.574$ and $\langle E\rangle = -3.366, -1.038$.

formula $E = \mathcal{H} = H_{n_0,n_0} + \beta/2 \approx \beta/2$ since $H_{n_0,n_0} \sim 1/\sqrt{N}$ (absence of self links with $A_{n_0,n_0} = 0$ and small diagonal matrix element from the GOE perturbation).

The 6 panels in the bottom three rows of Fig. B.8 show, in the same style as Fig. II.3, for different states the dependence of ρ_m on E_m for the largest iterations times $t = 2^{24}$ ($\beta = 10, 4$) or $t = 2^{25}$ ($\beta = 1$) (red + symbols) and at a shorter time $t/100$ (green $\times$ symbols). Furthermore, each panel also presents the theoretical curve $\rho_{\rm RJ}(E_m) = T/(E_m - \mu)$ (blue line) where T and μ are obtained by solving the constraints (II.16) at $E = \langle E\rangle = \sum_m E_m \rho_m(t)$ for the numerical data of $\rho_m(t)$ at the largest available value of t. The obtained values of T, μ and $\langle E\rangle$ for the 3 cases $\beta = 10, 4, 1$ of *Barabasi* are $T = -0.01322, -0.02075, -0.02822$, $\mu = 9.754, 9.853, 11.2$ and $\langle E\rangle = 4.744, 1.99, 0.5012$. For *Newman* these values (at same β-order) are $T = -0.01292, -0.02074, -0.02811$, $\mu = 9.753, 9.853, 11.16$ and $\langle E\rangle = 4.855, 1.991, 0.5069$. The negative values of T are coherent with the positive energy values above the critical value $E_c \approx 0$ for the transition from positive to negative T (see also Eq. (B.1) and the discussion of Fig. B.4 above).

From the physical point of view, we see that globally for all cases the states thermalize well to the theoretical curve for (nearly) all values ρ_m. The data points for the shorter time value $t/100$ show stronger fluctuations as expected and for $\beta = 1$ the quality of convergence is also a bit reduced, probably larger iterations times are still needed here.

B.2 Politician network

Fig. B.9, shows the IPR values of eigenmodes for the politician network at $\kappa = 0$ and $\kappa = 0.5$ (in the same style as Fig. B.2). For a significant number of boundary modes the IPR is very small with sames values between $\kappa = 0$ and $\kappa = 0.5$. Due to the large boundary energy gaps the states are essentially the same for both κ values. Modes in the bulk have a quite large distribution of IPR values between localized states (IPR ~ 10) and maximal values IRP ~ 1200 (for both κ values). There is also a signifiant reduction of typical IPR values for energies $E_m \approx 0$ by a factor 3 (2) for $\kappa = 0$

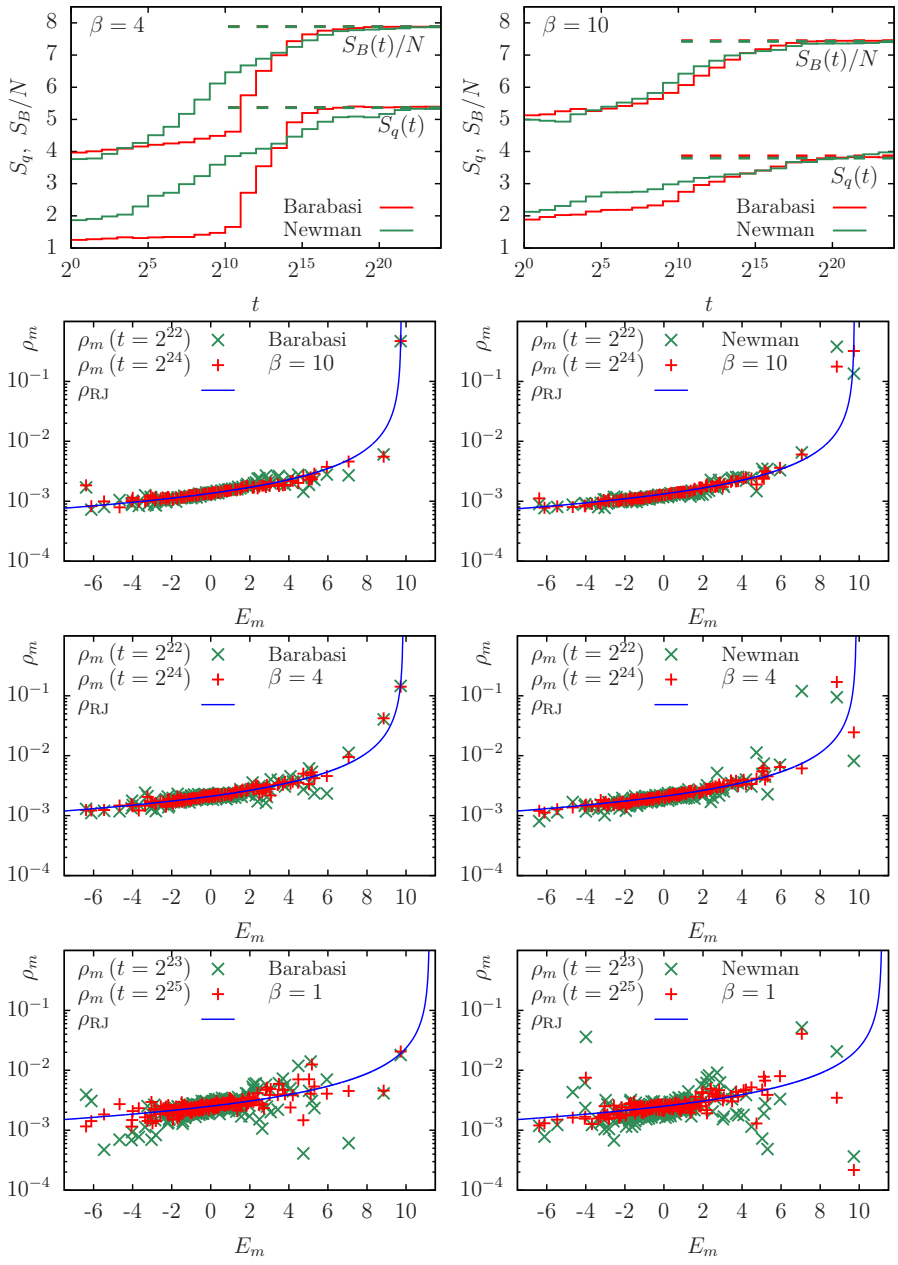

Fig. B.8 Results for the netscience network with $\kappa = 0.5$ and two initial states localized either on the node of *Barbasi* or *Newman*. Top panels show the time dependence of S_q and S_B/N for $\beta = 4$ (left) and $\beta = 10$ (right). The two top (bottom) curves correspond to $S_B(t)/N$ ($S_q(t)$) and dashed lines indicate the theoretical thermalized values for each case. The 6 bottom panels show ρ_m versus mode energy E_m for both initial conditions and $\beta = 10, 4$ ($t = 2^{22}, 2^{24}$) and $\beta = 1$ ($t = 2^{23}, 2^{25}$). See text and captions of Figs. II.3-II.5 for more technical details.

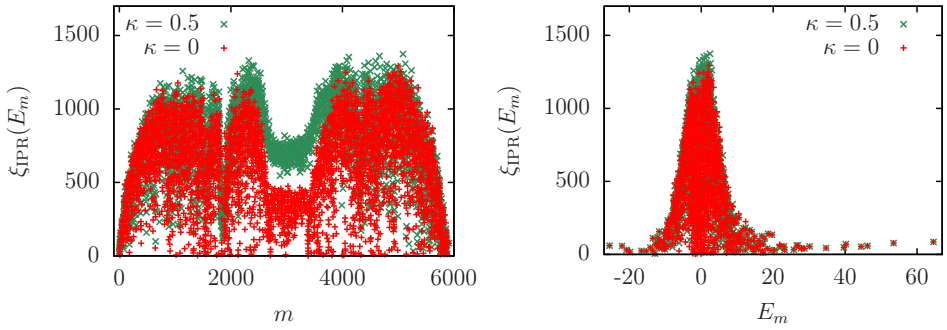

Fig. B.9 $\xi_{\rm IPR}(E_m)$ of eigenvector $\phi^{(m)}$ of H for the case of the politician network with $\kappa = 0$ and $\kappa = 0.5$ versus index m (energy E_m) in left (right) panel.

($\kappa = 0.5$). Furthermore, the probability (density of data points) to find very small IPR values (for center modes) is strongly reduced for $\kappa = 0.5$ in comparison to $\kappa = 0$.

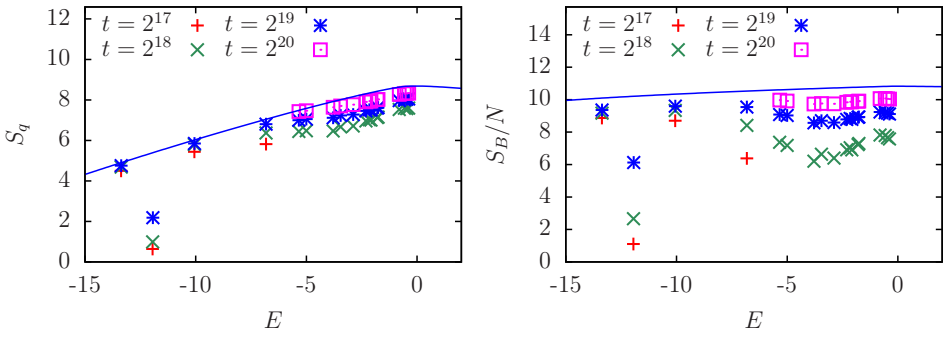

Fig. B.10 Entropy S_q (S_B/N) versus energy E in left (right) panel for some initial modes of the politician network with $\kappa = 0.5$, $N = 5908$, $\beta = 10$. For each case three data points for the three longest time values are shown to illustrate the thermalization. The first four modes ($m_0 = 8, 16, 32, 128$) were computed with the time step $dt = 1/32$ for the symplectic integrator up to $t = 2^{19}$. For other modes S_q and S_B were computed with $dt = 1/16$ (for $128 < m_0 \leq 600$) or $dt = 0.1$ (for $600 < m_0$) both up to $t = 2^{20}$. The blue line shows the energy dependence of the theoretical thermalized entropy for both entropy quantities.

In Fig. B.10, we show for a selected number of modes with initial energies in the interval $-14 < E_{m_0} < 0$ the dependence of both entropy values S_q and S_B/N on the final (linear) energy $E = \langle E \rangle = \sum_m E_m \rho_m$ (which is typically very close to E_{m_0}). For each data point the values for three successive time values $t = 2^{l-2}, 2^{l-1}, 2^l$ (with either $l = 19$ for $m_0 \leq 128$ or $l = 20$ for $m_0 > 128$) are shown indicating a clear tendency for convergence to the theoretical curve. For three of the four modes with $m_0 \leq 128$ and S_q the last data points are actually already very close to the theoretical curve and the remaining mode at $E \approx -12$ shows a strong increase of S_q between the last two time values indicating a potential convergence at later times.

B.3 Entropy in the RMT model

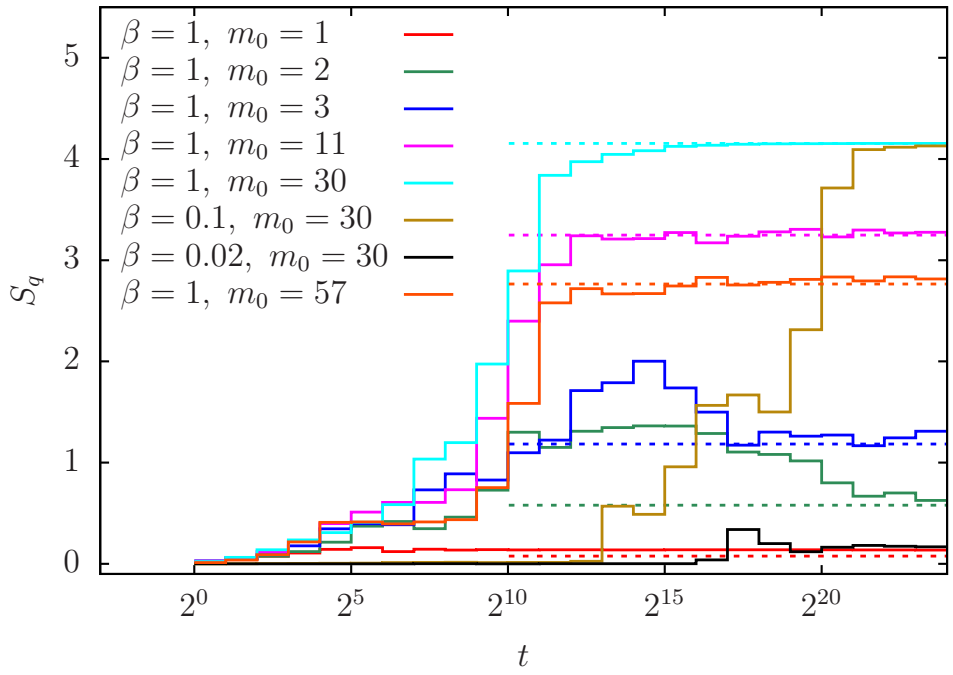

Fig. B.11 Time dependence of S_q for the case of a GOE matrix ($N = 64$, semicircle radius 1) using the data of [17]. The full lines correspond to $S_q(t)$ for the cases of Figure S1 of [17] and the dotted lines indicate the theoretical thermalized RJ values (using the color for the cases with $\beta = 1$). This figures is very similar to Figure S1 of [17]. It is shown here for convenience.

Figs. B.11 and B.12 show the time dependence of $S_q(t)$ and $S_B(t)/N$ respectively for a pure GOE matrix (corresponding to $A = 1$ and $\kappa = 1$ for $N = 64$) for the cases already shown in Fig. S1 of [17] which is actually very similar to Fig. B.11 (the latter shows more theoretical values as well). For S_q we have a nonmonotonic time dependence for the initial states at $m_0 = 2, 3$ at intermediate times. However, at large times these modes are well thermalized and close to the RJ condensate phase. For S_B the time dependence is always monotonic in the chaotic regime.

B.4 Wealth inequality and Lorenz curves

Fig. B.13 shows the density of state for the netscience network and a set of Lorenz curves for the case of a very strong value of κ. Now, the density of states is rather close to the semicercle law with radius $\kappa = 6$ and the behavior for $h > h_0$ ($h_0 =$ maximal value at which $w(h) = 0$) corresponds more to a smooth curve instead of a straight line as for the case $\kappa = 0.5$ shown Fig. II.8.

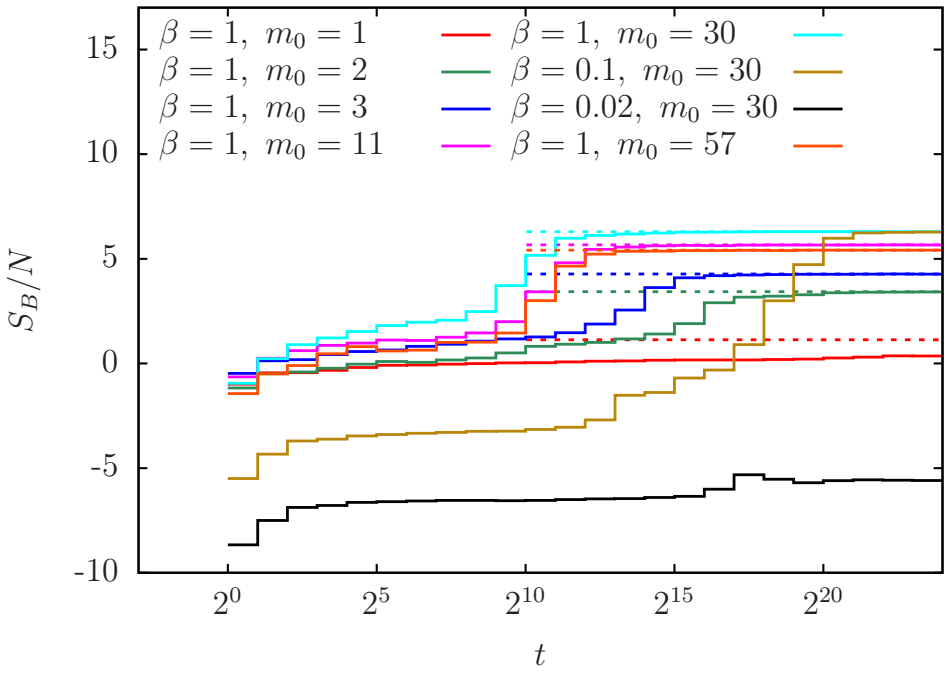

Fig. B.12 Time dependence of S_B/N for the case of a GOE matrix ($N = 64$, semicircle radius 1) using the data of [17]. The full lines correspond to $S_B(t)/N$ for the cases of Figure S1 of [17] and the dotted lines indicate the theoretical thermalized RJ values (using the color for the cases with $\beta = 1$). S_B has been computed by (II.20) using $h_B = 1/N^2$.

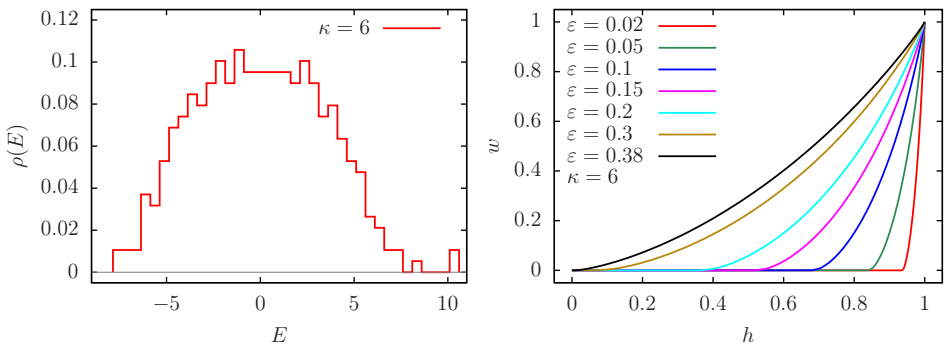

Fig. B.13 Density of states (Lorenz curves) for the netscience network at $\kappa = 6$ in left (right) panel.

References

[1] L. Boltzmann, *Weitere Studien über das Wärmegleichgewicht unter Gasmolekülen*, Wiener Berichte **66**, 275 (1872).

[2] E.Fermi, J.Pasta and S.Ulam, *Studies of non linear problems*, Los Alamos Report LA-1940 (1955); published later in E.Fermi *Collected papers*, E.Serge (Ed.) **2**, 491, Univ. Chicago Press, Chicago IL (1965); see also historical overview in T.Dauxois *Fermi, Pasta, Ulam and a mysterious lady*, Phys. Today **61(1)**, 55 (2008).

[3] N.J. Zabusky and M.D. Kruskal, *Interaction of "solitons" in a collisionless plasma and the recurrence of initial states*, Phys. Rev. Lett. **15**, 240 (1965).

[4] C. S. Gardner, J. M. Greene, M. D. Kruskal and R. M. Miura, *Method for solving the Korteweg - de Vries equation*, Phys. Rev. Lett. **19**, 1095 (1967).

[5] V.E. Zakharov and A.B. Shabat, *Interaction between solitons in a stable medium*, Sov. Phys. JETP **37(5)**, 823 (1973).

[6] M. Toda, *Studies of a non-linear lattice*, Phys. Reports **18(1)**, 1 (1975).

[7] G. Benettin, H. Christodoulidi and A. Ponno, *The Fermi-Pasta-Ulam problem and its underlying integrable dynamics*, J. Stat. Phys. **152**, 195 (2013).

[8] B.V. Chirikov and F.M. Izrailev, *Statistical properties of a non-linear string*, Sov. Phys. Doklady **11(1)**, 30 (1966).

[9] B.V.Chirikov, F.M.Izrailev and V.A.Tayursky, *Numerical experiments on statistical behavior of dynamical systems with a few degrees of freedoms*, Comp. Comm. Phys. **5**, 11 (1973).

[10] R. Livi, M. Pettini, S. Ruffo and A. Vulpiani, *Chaotic behavior in nonlinear Hamiltonian systems and equilibrium statistical mechanics*, J. Stat. Phys. **48**, 539 (1987).

[11] D.L. Shepelyansky, *Low energy chaos in the Fermi-Pasta-Ulam problem*, Nonlinearity **10**, 1331 (1997).

[12] V. Arnold, A. Avez, *Ergodic problems of classical mechanics*, Benjamin, N.Y. (1968).

[13] I. P. Cornfeld, S. V. Fomin and Ya. G. Sinai, *Ergodic theory*, Springer-Verlag, N.Y. (1982).

[14] B. V. Chirikov, *A universal instability of many-dimensional oscillator systems*, Phys. Rep. **52**, 263 (1979).

[15] A. Lichtenberg and M. Lieberman, *Regular and Chaotic Dynamics*, Springer, N.Y. (1992).

[16] G.Gallavotti (Ed.), *The Fermi-Pasta-Ulam problem: a status report*, Lect. Notes Phys. **728**, Springer, Berlin (2008).

[17] K.M. Frahm and D.L. Shepelyansky, *Nonlinear perturbation of Random Matrix Theory*, Phys. Rev. Lett. **131**, 077201 (2023).

[18] E.P. Wigner, *Random matrices in physics*, SIAM Review **9(1)**, 1 (1967).

[19] M.L. Mehta, *Random matrices*, Elsvier, Amsterdam (2004).

[20] T. Guhr, A. Müller-Groeling and H.A. Weidenmüller, *Random Matrix Theories in quantum physics: common concepts*, Phys.Rep. **299**, 189 (1998).

[21] O. Bohigas, M.-J. Giannoni and C. Schmit, *Characterization of chaotic quantum spectra and universality of level fluctuation laws*, Phys. Rev. Lett. **52**, 1 (1984).

[22] F. Haake, *Quantum signatures of chaos*, Springer, Berlin (2010).

[23] L.D. Landau, and E.M. Lifshitz, *Statistical physics*, Wiley, New York (1976).

[24] J.E. Mayer, M. Goeppert-Mayer, *Statistical mechanics*, John Wiley & Sons, N.Y. (1977).

[25] V.E. Zakharov, V.S. L'vov, and G. Falkovich, *Kolmogorov spectra of turbulence I*, Springer, Berlin, (1992).

[26] A. Picozzi, J. Garnier, T. Hansson, P. Suret, S. Randoux, G. Millot and D.N. Christodoulides, *Optical wave turbulence: Towards a unified nonequilibrium thermodynamic formulation of statistical nonlinear optics*, Phys. Reports **542**, 1 (2014).

[27] L. Ermann, A.D. Chepelianskii, and D.L.Shepelyansky, *Dynamical thermalization, Rayleigh-Jeans condensate, vortexes and wave collapse in quantum chaos fibers and fluid of light*, arXiv:2506.06534[cond-mat.stat-mech] (2025).

[28] H, Fröhlich, *Bose condensation of strongly excited longitudinal electric modes*, Phys. Lett. A **26A(9)**, 402 (1968).

[29] H. Fröhlich, *Long-range coherence and energy storage in biological systems*, Int. J. Quantum Chemistry **II**, 641 (1968).

[30] S. Dorogovtsev, *Lectures in Complex Networks*, Oxford University Press, UK (2010).

[31] M. Newman, *Networks*, Oxford University Press, UK (2018).

[32] T. Piketty, *Capital in the Twenty-First Century*, Belknap Press of Harvard University Press, Cambridge, MA (2014).

[33] L. Chancel, T. Piketty, E. Saez, G. Zucman *et al. World Inequality Report 2022*, World Inequality Lab https://wir2022.wid.world (Accessed on 8 June 2025).

[34] B. Roach, P. J. Rajkanikar, N. Goodwin, and J.Harris, *Social and Economic Inequality*, An ECI Teaching Module on Social and Environmental Issues, Economics in Context Initiative, Global Development Policy Center, Boston University (2023), https://www.bu.edu/eci/files/2023/05/Inequality-Module-2023.pdf (Accessed 8 June 2025).

[35] M.O. Lorenz, *Methods of measuring the concentration of wealth*, Quarterly Publications of the American Statistical Association, **9**, (New Series, No. 70), 209–219 (1905); https://doi.org/10.1080/15225437.1905.10503443 (Accessed 8 June 2025).

[36] C. Gini, *Sulla misura della concentrazione e della variabilit'a dei caratteri*, Atti del Reale Istituto Veneto di Scienze, Lettere ed Arti, **73**, 1203–1248 (1914); English translation in Metron - Int. J. Statisrics, **63**, 3–38 (2005); https://www.dss.uniroma1.it/RePec/mtn/articoli/2005-1-1.pdf (Accessed 8 June 2025).

[37] Wikipedia, *List of sovereign states by wealth inequality*, (Accessed 8 June 2025).

[38] E.M. Lifshitz and L.P. Pitaevskii, *Physical kinetics*, Pergamon Press N.Y. (1995).

[39] J. Angle, *The surplus theory of social stratification and the size distribution of personal Wealth*, Soc. Forces **65**, 293 (1986).

[40] S. Ispolatov, P. L. Krapivsky, and S. Redner, *Wealth distributions in asset exchange models*, Eur. Phys. J. B. **2**, 267 (1998).

[41] A. Dragulescu, and V. Yakovenko, *Statistical mechanics of money*, Eur. Phys. J. B. **17**, 723 (2000).

[42] J.-P. Bouchaud, and M. Mezard, *Wealth condensation in a simple model of economy*, Physica A **282**, 536 (2000).

[43] V. M. Yakovenko, and J. B. Rosser, *Colloquium: Statistical mechanics of money, wealth, and income*, Rev. Mod. Phys. **81**, 1703 (2009).

[44] B. K. Chakrabarti, A. Chakraborti, S.R. Chakravarty, and A. Chatterjee, *Econophysics of income and wealth distributions*, Cambridge University Press, N.Y. (2013).

[45] B. M. Boghosian, A. Devitt-Lee, M. Johnson, J. Li, J. A. Marcq, and H. Wang, *Oligarchy as a phase transition: the effect of wealth-attained advantage in a Fokker–Planck description of asset exchange*, Physica A **476**, 15 (2017).

[46] B. M. Boghosian, *The inescapable casino*, Sci. American, November, 71 (2019).

[47] N. V. Von Bibow, and J.L. Perotti, *Study of the Extended Yard Sale model of wealth distribution on Erdos-Renyi random networks*, arXiv:2505.04032[cond-mat.stat-mech] (2025).

[48] K. Krupa, A. Tonello, A. Barthelemy, B.M. Shalaby, A. Bendahmane, G. Millot and S. Wabnitz, *Observation of geometric parametric instability induced by the periodic spatial self-imaging of multimode waves*, Phys. Rev. Lett. **116**, 183901 (2016).

[49] C. Connaughton, C. Josserand, A. Picozzi, Y. Pomeau, and S. Rica, *Condensation of classical nonlinear waves*, Phys. Rev. Lett. **95**, 263901 (2005).

[50] K. Baudin, A. Fusaro, K. Krupa, J. Garnier, S. Rica, G. Millot, and A. Picozzi, *Classical Rayleigh-Jeans condensation of light waves: observation and thermodynamic characterization*, Phys. Rev. Lett. **125**, 244101 (2020).

[51] E.V. Podivilov, F. Mangini, O.S. Sidelnikov, M. Ferraro, M. Gervaziev, D.S. Kharenko, M. Zitelli, M.P. Fedoruk, S.A Babin, and S. Wabnitz, *Thermalization of orbital angular momentum beams in multimode optical fibers*, Phys. Rev. Lett. **128**, 243901 (2022).

[52] H. Pourbeyram, P. Sidorenko, F.O. Wu, N. Bender, L. Wright, D.N. Christodoulides, and F. Wise, *Direct observations of thermalization to a Rayleigh–Jeans distribution in multimode optical fibres*, Nature Phys. **18**, 685 (2022).

[53] K. Baudi, J. Garnier, A. Fusaro, N. Berti, C. Michel, K. Krupa, G. Millot. and A. Picozzi, *Observation of light thermalization to negative-temperature Rayleigh-Jeans equilibrium states in multimode optical fibers*, Phys. Rev. Lett. **130**, 063801 (2023).

[54] A. Aladangady, and A. Forde, *Wealth Inequality and the Racial Wealth Gap*, FEDS Notes Oct 22 (2021); https://www.federalreserve.gov/econres/notes/feds-notes/2021-index.htm, (Accessed 8 June 2025).

[55] E. Chamberlain, *Wealth in Great Britain Wave 4. Chapter 2: Total wealth, Wealth in Great Britain, 2012 to 2014*, 18 Dec 2015; https://www.ons.gov.uk/peoplepopulationandcommunity/personalandhouseholdfinances/incomeandwealth/compendium/wealthingreatbritainwave4/2012to2014/chapter2totalwealthwealthingreatbritain2012to2014 (Accessed 8 June 2025).

[56] F. Cowell, B. Nolan, J.Olivera, and Ph. Van Kerm, *Wealth, Top Incomes and Inequality*, p.175, in *National Wealth*, Eds. K. Hamilton, and C. Herburn, Oxford Univ. Press, Oxford UK (2017),

[57] Holdings SPDR S&P500 ETF Trust of June 16 (2025); https://www.ssga.com/us/en/intermediary/etfs/spdr-sp-500-etf-trust-spy

[58] London stock exchange data of capitalization of companies, December 31 (2024), https://www.londonstockexchange.com/reports?trkcode=lsehomstats&tab=issuers (Accessed 19 June 2025).

[59] Hong Kong stock exchange data of capitalization of companies, June 19 (2025), https://www.hkex.com.hk/Market-Data/Securities-Prices/Equities?sc_lang=en (Accessed 19 June 2025).

[60] M. E. J. Newman, *Network data*, http://www.umich.edu/~mejn/netdata, (Accessed 12 September 2025).

[61] M. E. J. Newman, *Scientific collaboration networks. II. Shortest paths, weighted networks, and centrality*, Phys. Rev. E **64**, 016132 (2001).

[62] M. E. J. Newman, *Finding community structure in networks using the eigenvectors of matrices*, Phys. Rev. E **74**, 036104 (2006).

[63] M. E. J. Newman, *Community Centrality*, http://www.umich.edu/~mejn/centrality (Accessed 12 September 2025).

[64] B. Rozemberczki, R. Davies, R. Sarkar and C. Sutton, *Graph Embedding with Self Clustering*, arXiv:1802.03997 (2018); *GEMSEC: graph embedding with self clustering*, ASONAM '19: Proceedings of the 2019 IEEE/ACM International Conference on Advances in Social Networks Analysis and Mining, page 65, (2020), https://doi.org/10.1145/3341161.3342890

[65] L. Backstrom, P. Boldi, M. Rosa, J. Ugander and S. Vigna, *Four degrees of separation*, WebSci 2012: Proceedings of the 4th Annual ACM Web Science Conf., pafe 33, https://doi.org/10.1145/2380718.2380723

[66] E. Forest and R.D. Ruth, *Fourth-order symplectic integration*. Physica D. 43: 105 (1990); https://cloudfront.escholarship.org/dist/prd/content/qt35h9v2k9/qt35h9v2k9.pdf (Accessed Dec 2022).

[67] R.I. McLachlan and G.R.W. Quispel, *Splitting methods*, Acta Numerica **11**, 341 - 434 (2002).

[68] S. MacNamara and G. Strang, *Operator splitting*/ In: R. Glowinski, S. Osher, W. Yin (Eds) *Splitting methods in Communication, Imaging, Science, and Engineering*, Scientific Computation. Springer, Cham. pp.95-114 (2016); https://doi.org/10.1007/978-3-319-41589-5_3

[69] Ermann L., Frahm K. M. and Shepelyansky D. L., *Google matrix analysis of directed networks*, Rev. Mod. Phys. **87** (2015) 1261.

[70] F. Evers and A.D. Mirlin, *Anderson transitions*, Rev. Mod. Phys. **80**, 1355 (2008).

[71] B.V. Chirikov and D.L. Shepelyanskii, *Dynamics of some homogeneous models of classical Yang-Mills fields*, Sov. J. Nucl. Phys. **36(6)**, 908 (1982).

[72] M. Mulansky, K. Ahnert, A. Pikovsky and D.L. Shepelyansky, *Strong and weak chaos in weakly nonintegrable many-body Hamiltonian systems*, J. Stat. Phys. **145**, 1256 (2011).